5-2012

Flushing of a Dense Fluid from an Isolated Urban Canyon

Zahra Baratian-ghorghi
Clemson University, Gbarati@clemson.edu

Flushing of a Dense Fluid from an Isolated Urban Canyon

A Dissertation
Presented to
the Graduate School of
Clemson University

In Partial Fulfillment
of the Requirements for the Degree
Doctor of Philosophy
Civil Engineering

by
Zahra Baratian-Ghorghi
August 2012

Accepted by:
Dr. Nigel B. Kaye , Committee Chair
Dr. Abdul A. Khan
Dr. Thomas J. Overcamp
Dr. Ben Sill

ABSTRACT

The mechanics of shear-driven flushing of a dense fluid from a canyon is investigated through a series of laboratory experiments. Such a flow has many environmental applications including the removal of dense pollutants trapped in urban canyons and the purging of salt water from bed depressions at river mouths. While there is an extensive literature on flow in canyons and cavities for the neutrally buoyant case, the problem of flushing a dense fluid from canyon has received considerably less attention. To understand the dynamics of the mixing and to quantify the buoyant contaminant flushing rate, a broad range of experimental results using multiple techniques to quantify the flushing rate are presented

First the effect of the fluid density in the canyon, which is parameterized in terms of the flow Richardson number, is examined. For a square canyon a total of 26 experiments were conducted for Richardson numbers ranging from 0.08 to 4.5. The effect of the buoyancy on the in-canyon flow structure is examined and the regime diagram showing the flow observed in different ranges of Richardson number is presented. Also the flushing time and decay rate of the dense fluid is quantified. Three different mean stratifications are observed, namely well-mixed, continuously stratified, and two-layer. Increasing the Richardson number decreases the rate of flushing from the cavity. Curve fits through the measured buoyancy over time were used to calculate the flushing rate.

The effect of canyon aspect ratio on the flushing of a dense fluid is considered through four series of finite release experiments for different aspect ratios (η=0.45, 0.75, 1, 2). A total of 64 experiments are conducted over a range of Richardson numbers. The effect of the canyon width on the observed flow regime, in-canyon vortex structure and buoyancy stratification is demonstrated. Empirical equations for the initial decay rate are also determined for all aspect

ratios and their results are compared with the existing data in the literature. For high Richardson numbers which is a two-layer stratification, the lower dense layer in the stratification acts as a soft bottom to the canyon, alters the effective aspect ratio of the canyon and changes the flow dynamics. Narrower canyons were found to flush more slowly as the large scale vortex that drives most of the mixing is restricted laterally and, therefore, does not penetrate deep into the canyon.

An experimental investigation of the effect of the upstream surface roughness is also provided in order to highlight the impact of the upstream boundary properties on the flushing. This is the first such systematic investigation of the role of turbulence intensity on flushing of fluid form a canyon. Three series of tests for different upstream surface roughness (d_{84}= 1.14, 0.83 and 0 cm) have been conducted. It is shown that the initial purging of dense fluid is driven by the mean flow. However, at later stages, the turbulence within the flow is the dominant cause of mixing.

Finally an analytical model is developed to describe both continuous and finite release flows. A series of continuous release experiments were run in order to measure the exact rate of mixing for a broad range of source buoyancies and layer depths. The results of this two-layer model coupled with a revised equation for non-two layer flow regimes shows a good agreement with the all the experimental data presented in this study. It is shown that all the mixing rate data from the finite release and continuous release experiments collapse onto a single line when parameterized in terms of a layer Richardson number.

DEDICATION

I gratefully dedicate this thesis to the most precious gift in my life

my selfless and devoted parents, Aqdas and Ismael.

ACKNOWLEDGEMENTS

First and foremost, I give my utmost gratitude to Dr. Nigel B. Kaye not only for his patience, guidance and untiring supports as my dissertation adviser and teacher in life, but also for all I learnt from his sincerity, respect and modesty, despite his wealth of knowledge. I do not feel I could have had a better adviser. I also would like to thank my committee members of my dissertation, Dr. Ben Sill, Dr. Abdul A. Khan and Dr. Thomas J. Overcamp for their timely review of my thesis, delivering their valuable guidance, and sharing their feedback.

I would like to graciously thank Mr. John D. Elsea for all his help and support in physical model development. Also I would like to extend my thanks to Mr. Danny Metz and Warren H. Scovil for their technical support. This dissertation would not have been possible without people and also friends who helped me in one way or another. I would like to thank them all for being there for me during my research and whenever I was in need. I wish them all best future.

Last but not least I send my sincere gratitude to my family: my lovely sisters, helpful brothers, and my sacrificing parents. I am deeply indebted to them and will never forget their constantly unconditional love, support, and encouragement in my studies and endeavors.

ZAHRA BARATIAN-GHORGHI

August 2012

TABLE OF CONTENTS

LIST OF TABLES

LIST OF FIGURES

LIST OF SYMBOLS

a	constant coefficient
A	canyon cross section area
A_1	non-dimensional parameter dependent on shear layer turbulence intensity
A_2	constant value
b	constant coefficient
c	constant coefficient
C	concentration at any time
C_s	source concentration
C'	relative concentration
$\bar{C}$	average pollution concentration in canyon
d	Initial interface deflection
d_t	time decay constant
d_{84}	the gravel sizes which 84% of particles are smaller than
D	depth of upstream overflow
e	mathematical constant, Euler's number
Fr	Froude number
g	gravity acceleration
g'	reduced gravity
g'_a	ambient flow buoyancy
g'_{ave}	average buoyancy of canyon
g'_l	dense layer buoyancy

g'_s	source buoyancy
g'_0	initial buoyancy
G	total buoyancy
h	parapet height
h_{ss}	interface height at steady state
H	buildings height
I	turbulence intensity defined by root-mean-square value of the time series of individual velocity magnitude values
I_l	light intensity
I_{lz}	light intensity zero offset
I_{l0}	initial light intensity
Je	Jensen number
k	non-dimensional exponential decay rate
k_{ET}	mixing efficiency constant
K	decay constant with unit of 1/s
K_a	constant of proportionality relating γ_a to C
KE	kinetic energy
l	turbulence length
L	length of the path through the dyed fluid
m	constant
n	constant
Pe	Peclet number

q_s	two-dimensional source flow rate
Q	rate of pollutant release
Re	Reynolds number
Ri	Richardson number
Ri_l	Richardson number based on buoyancy of the dense layer
Ri_s	Richardson number based on source buoyancy
Ri_0	Richardson number based on the buoyancy at t =0
t	time
t_r	time scale for flushing
T_{ref}	reference time
u	mean velocity at the height of z
u_e	exchange velocity
u_h	ambient velocity just above the interface height
u_s	skimming velocity
U	reference velocity
U_*	shear velocity
v	two-dimensional outflow volume flux
V	canyon volume
W	canyon width
x	horizontal distance
y	streetwise direction
z_0	upstream surface roughness

z	Height
α	exchange coefficient
α_t	thermal expansion coefficient
β	skimming coefficient
γ	scaled buoyancy
γ_a	coefficient of light attenuation
γ_l	scaled buoyancy of the dense layer
γ_{ss}	non-dimensional buoyancy of the layer at steady state
γ'	vertical buoyancy gradient
γ'_{max}	maximum vertical buoyancy gradient
Γ	non-dimensional total buoyancy
Γ_e	maximum extent of initial exponential decay
Γ_{ss}	non-dimensional total buoyancy at steady state
δ	maximum interface thickness
$\delta_{g'}$	density interface thickness
δ_v	shear layer thickness
$\Delta\theta$	temperature difference
ζ_{ss}	non-dimensional interface height at steady state
ζ	scaled height
ζ_i	Interface height
η	aspect ratio
$\eta_{effectiv}$	effective aspect ratio

κ	von Karman constant
κ_D	molecular diffusivity of the contaminant
υ	kinematic viscosity of water
ρ	pollutant density
ρ_0	ambient flow density
τ	scaled time
$\tau_{90\%}$	time taken to flush 90% of initial buoyancy
$\tau_{50\%}$	time taken to flush 50% of initial buoyancy
φ	scaled source flow rate

CHAPTER ONE

INTRODUCTION

The main problem addressed by this dissertation is the flushing of a dense air pollutant from an urban canyon. This chapter introduces the specific questions this study seeks to answer. Section 1.1 describes the motivation for choosing the project and a review of the literature follows in section 1.2. The specific problem considered is defined in section 1.3. An outline of the dissertation is presented in section 1.4.

1.1 Motivation

This study considers the flushing of dense fluid trapped in a cavity by a steady turbulent flow passing over the top of the cavity. Such a flow has many environmental and industrial applications. For example, dense gas pollutants can become trapped in urban canopies formed by building arrays, and flushed by vertical mixing driven by the wind flowing above the buildings. While dense gas releases in urban areas are rare, they can have catastrophic consequences. Three such events have occurred over the past few years in Festus, MO (2002), Macdona, TX (2004), and Graniteville, SC (2005), resulting in several deaths (Hanna et al., 2008; Buckley et al., 2007). Further, salt water trapped in bed depressions at river mouths can be flushed by the fresh water overflow of the river (Coates et al., 2001; Debler and Armfield 1997). On a smaller scale, heat can become trapped on the underside of electronic circuit boards between densely packed arrays of electrical components.

While an extensive literature addresses flow in canyon and cavity geometries for neutrally buoyant fluids (see, for example, Caton et al., 2003; Simoens et al., 2007; Chang and Meroney, 2003) the problem of flushing a dense fluid from a canyon has received considerably

less attention. To the best of the author's knowledge, thus far there has been no attempt to fully understand the effect of fluid buoyancy on the contaminant flushing process and flow structure within the street canyon. In addition to the density (negative buoyancy) of the fluid trapped in the cavity, the cavity geometry, and upstream boundary layer properties will also influence the flushing rate. This study experimentally investigates the influence of pollutant buoyancy, canyon geometry, and upstream boundary layer properties on the flushing of a dense fluid from a street canyon.

1.2 Review of relevant literature

The goal of this research is to improve understanding of the physics of dense gas dispersion in urban environments. A full understanding of dense gas dispersion in urban environments requires an understanding of the urban wind climate and the mechanics of pollution mixing. Therefore, numerous studies have been conducted on urban canopy flows and urban pollution dispersion. Some of these studies will be reviewed in the next sections.

1.2.1 Urban wind climate and urban canopy flows

Study of the dispersion of pollution in urban areas requires knowledge of the flow characteristics over the canyon and inside the canopy, which determine how pollutants are mixed and transferred from street level up into the atmosphere.

The atmospheric boundary layer (ABL) over a surface covered with a large number of discrete buildings behaves like a rough turbulent boundary-layer flow. Large scale ABL flow models usually treat urban surface topography, such as clusters of buildings, as surface roughness. This modeling approach largely ignores the flow within the canopy. Since the flow

inside the canopy is non-homogenous and plays an important role in pollutant dispersion, it is important to understand wind flow within the urban canopy.

To predict the spatially averaged velocity profile within and above arrays of buildings, different studies have been done which describe the urban canopies in term of the morphological parameters of the buildings and avoid resolving the flow around individual obstacles (e.g., Macdonald, 2000; Di Sabatino et al., 2007). In the vicinity of the obstacles, the flow is complicated by the large spatial variation in the average wind velocity. The simplest urban canopy unit is the two-dimensional street canyon. Several studies focus on street canyon flow structure (Coceal et al., 2007; Christen et al., 2007; Oke, 1988; Soulhac et al., 2008; Xie et al., 2007; Sini et al., 1996; Depaul and Sheih 1986; Chang and Meroney, 2003; Simoens et al., 2007; Olvera et al., 2008; Klein et al., 2007). Some of these studies looked at the flow structure influenced by building height, H (e.g. Klein et al., 2007) or canyon aspect ratio (e.g. Simoens et al., 2007) defined as

$$\eta = \frac{W}{H} \tag{1.1}$$

where W is the canyon width and H is the canyon height (equal to the building height).

Urban canyon flow was categorized by Oke (1988) to be either isolated roughness flow, in which the boundary layer flow re-attaches to the ground between buildings, wake interference flow, in which each downwind building feels the effect of the upwind buildings wake, and skimming flow, in which the ABL is raised up to the height of the building roofs and the flow in the canyons is driven by shear at the top of the canyon. These different flows are shown schematically in Figure 1.1.

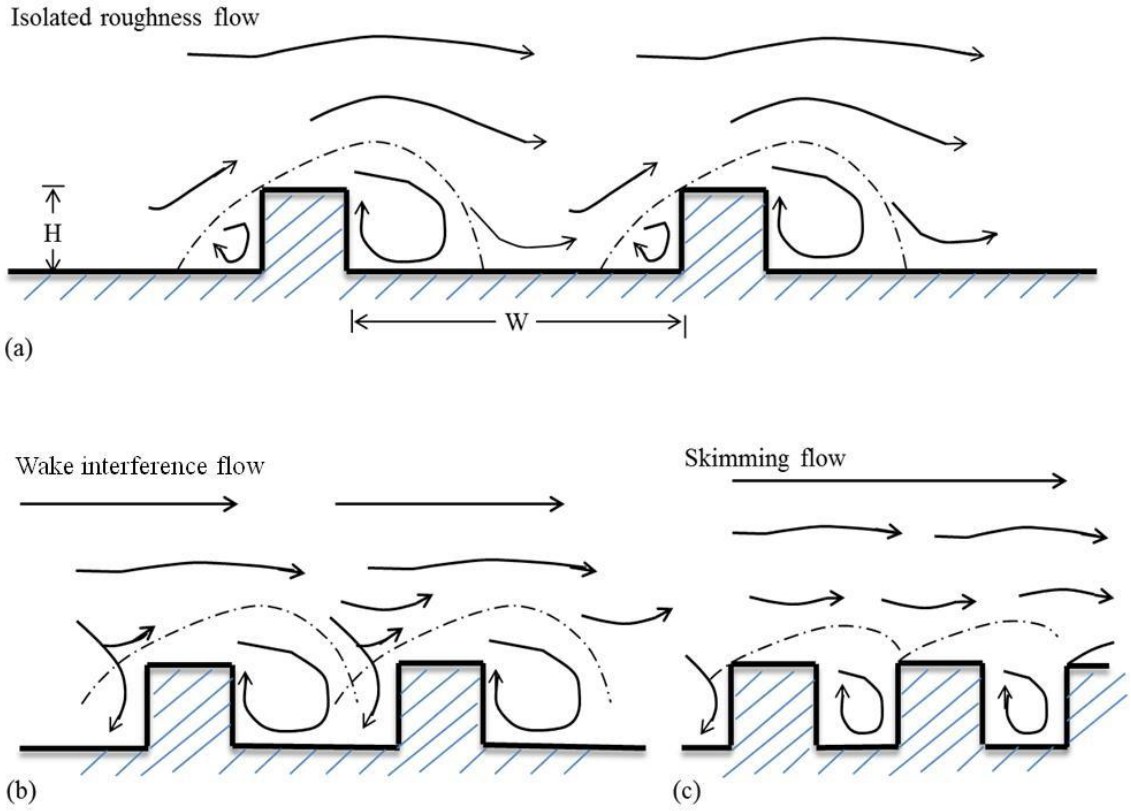

Figure 1.1: Schematic diagrams of a. isolated roughness, b; wake interference, and c. skimming flows (Oke, 1988).

For a given canyon geometry, the dispersion will be influenced by the pollutant properties (for example, phase and density), and the nature of the pollutant source, namely, instantaneous or continuous.

1.2.2 Urban pollution dispersion

Urban pollution dispersion models are mostly concerned with predicting the spatial distribution of pollutant concentration resulting from a constant flux or instantaneous point or area source. Models are typically a variation of the Gaussian plume model of Pasquill (Pasquill,

1971; Klein et al., 2007; Deaves, 1992) in which the vertical and lateral spreading rates of a plume are parameterized in terms of the local topography (surface roughness, etc.) and atmospheric stability (wind speed, stratification, etc.). The merits of the Gaussian models are their relative simplicity and limited input parameters. However, they usually model obstacles, such as buildings, as a uniform roughness. They are, therefore, appropriate to predict dispersion when the building dimensions are small compared to the pollutant cloud depth (see, for example, Macdonald and Griffith, 1997; Zhou and Hanna 2007).

As with ABL models, this approach largely ignores the canopy flow, assuming, rather, that the mean building's effect on dispersion can be parameterized in terms of a surface roughness drag on the flow and increased turbulent mixing. It is then assumed that the mean pollutant concentration predicted is appropriate for flow within the canopy. However, this ignores the heterogeneity of the building geometry and therefore fails to account for any potential trapping of pollutants within the canopy. The pollution trapped in the surroundings of an urban street and high-rise buildings can cause serious health risks, because the dispersion process is significantly limited and can produce poor air quality.

Attempts to understand dispersion within the urban canopy fall into two broad categories: those that model the mean flow and dispersion within building arrays (Hamlyn et al., 2007; Macdonald et al., 1997; Macdonald et al., 1998), and those that look at flow near individual urban structures such as buildings (Olvera et al., 2008; Mavroidis, 2001), intersections (Klein et al., 2007), urban canyons (Caton et al., 2003; Simoens and Wallace, 2008; Taseiko et al., 2009), and suburban backyards (Mensink and Cosemans, 2008).

In the vast majority of urban dispersion studies, only neutrally buoyant pollutants were considered (e.g., Chang and Monerey, 2003; Li et al., 2007; Liu et al., 2011; Cheng et al., 2008;

Sini et al., 1996). A significant risk of dense gas pollution in highly populated urban areas exists, however, due to either accidental or malicious releases. Such releases pose a real danger to the local inhabitants' health (Buckley et al., 2007). The density of such pollutants drives negative buoyancy that will act to suppress vertical mixing, as work must be done by the incoming flow to raise the dense fluid up into the atmosphere. The relative influence of the fluid density is typically expressed in terms of a bulk Richardson number, which is the ratio of the buoyancy force to the inertia force given by

$$Ri = \frac{g'H}{U^2} \tag{1.2}$$

in which U is the flow velocity over the top of the cavity, and g' is the negative buoyancy of the pollutant (Strang and Fernando 2004; Armfield and Debler 1993; Briggs et al., 1990) defined as

$$g' = g\frac{\rho - \rho_0}{\rho_0} \tag{1.3}$$

where ρ_0 is the density of the ambient fluid and ρ is the pollutant density. Thus for negative buoyancy, $Ri > 0$. The higher the Richardson number the more stable the flow and the lower the rate of vertical mixing. When $Ri > 1$ the inertia force is smaller than buoyancy force so the effect of the buoyancy must be considered in modeling the street canyon flow (Liu et al., 2003). However multiple studies showed that, even for Ri numbers lower than one, buoyancy significantly influences the pollutant mixing mechanism (Chang et al., 2007a; Chang et al., 2007b).

The removal of a buoyant pollutant from a cavity or a canyon has been examined numerically and experimentally (e.g. Chang et al., 2007a; Chang et al., 2007b; Kim and Baik, 2001; Liu et al., 2003; Chan et al., 2002). In these studies, the buoyancy was due to either thermal difference

(e.g. Xie et al., 2007; Cheng and Liu 2011; Cheng et al., 2009) or a density difference between the ambient fluid and the pollutant material (e.g. Armfield and Debler, 1993; Kirkpatrick et al., 2012; Strang and Fernando, 2004; Liu et al., 2003; Briggs et al., 1990; Castro et al., 1993).

In all these studies, different geometries have been considered. Meroney et al. (1996) stated that, for modeling a street canyon in open country, an isolated canyon geometry is appropriate (Figure 1.2a). Other researchers have used an isolated cavity geometry (Figure 1.2b) in which the effect of flow separation at the leading edge of the upstream building is no longer present. However, in the case of urban canopies, the buildings and surface roughness upstream of the specific street canyon shifts the zero plane displacement of the boundary layer up, meaning that periodic street canyons (Figure 1.2c) are more appropriate for modeling urban areas (see Liu et al, 2011; Cheng and Liu 2011; Cheng et al., 2009; and Cheng et al., 2008). In this study, the open country condition is considered, so an isolated canyon (Figure 1.2a) is used to model a street canyon.

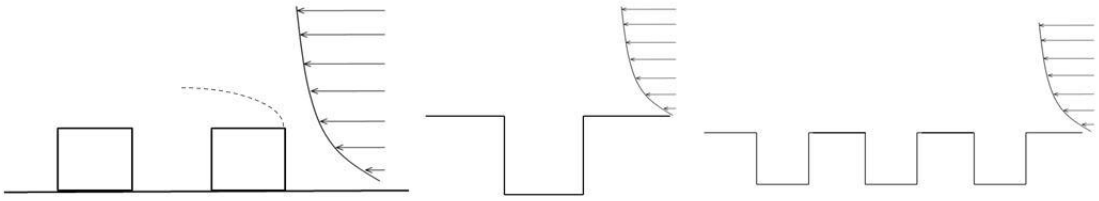

Figure 1.2: Schematic diagram of (a) an isolated street canyon; (b) an isolated cavity; and (c) multiple cavity geometry.

Table 1.1 summarizes studies on pollution dispersion in urban canyons in terms of buoyancy, canyon geometry, and upstream velocity.

Table 1.1: Summary of several studies on the cavity/canyon geometry

	η	Ri	Upstream profile	Geometry	Number of upstream cavities	
Armfield and Debler 1993	1	$0.02 < Ri < 0.6$	free stream flow	cavity	0	CFD&W.F*
Sini et al., 1996	0-∞	$Ri < 0$	log-law	cavity	0	CFD
Debler and Armfield, 1997	1-16.7	$0.45 < Ri < 31$	free stream flow	cavity	0	W.F*
Baik and Park. 2000	1, 0.66, 0.5, 0.42, 0.33	0	rough B.L.	canyon	0	CFD&W.F*
Uehara et al., 2000	1	$-0.2 < Ri < 0.8$	rough B.L.	canyon	4	W.T*
Kim and Baik, 2001	0.6-3.6	$Ri < 0$	power-law	cavity	0	CFD
Chang and Monerey, 2003	0.5, 1, 2, 4, 6	0	rough B.L	canyon	0, 1, 2, 7	CFD & W.T*
Caton et al., 2003	1	0	free stream flow	cavity	0	W.F*
Kim and Baik, 2003	1	0	power-law	cavity	0	CFD
Liu et al., 2003	0.67, 0.83, 1.7	$-\infty - 0$	free stream flow	canyon	0	W.F*

Park et al., 2004	0.64, 1.39, 2.38	0	rough B.L.	canyon	0	W.T*
Strang and Fernando, 2004	1,2	$Ri > 0$	free stream flow	cavity	0	W.F*
Kirkpatrick and Armfield, 2005	1	$0.02 < Ri < 0.6$	free stream flow	cavity	0	CFD&W.F*
Kim and Baik, 2005	1	$Ri < 0$	free stream flow	canyon	0	W.F*
Li et al., 2005	0.5,1,2	0	free stream flow	cavity	6	CFD
Liu et al., 2005	0.5,1,2	0	free stream flow	cavity	∞	CFD
Xie et al., 2006	1	-0.21	free stream flow	cavity	4	CFD
Chang et al., 2007a	2	0,0.2	laminar B.L.	cavity	0	CFD
Chang et al., 2007b	2	0, 0.2	turbulent B.L	cavity	0	CFD
Xie et al., 2007	0.5, 1, 2, 10	$Ri < 0$	free stream flow	cavity	4	CFD
Siemon et al., 2007	1, 10, 12	0	rough B.L.	canyon	0	W.T
Li et al., 2007	2, 1, 0.5	-	free stream flow	cavity	∞	CFD
Soulhac et al., 2008	0-∞	0	log-law	cavity	0	Theo.
Cheng et al., 2008	0.5, 1, 2	0	free stream flow	cavity	6	CFD

Cheng et al., 2009	1	$-10.6 \leq Ri \leq 0$	power-law	cavity	6	CFD
Li et al., 2010	1	-2.4, -1.2,-0.6,0	free stream flow	cavity	∞	CFD
Liu et al., 2011	$0.067 \leq \eta \leq 2.5$	0	power-law	cavity	6	CFD
Cheng and Liu 2011	1	-0.11,-0.06, 0, 0.18, 0.35	free stream flow	cavity	1	CFD
Kirkpatrick and Armfield, 2012	$7 < \eta < 17$	$1 < Ri < 20$	free stream flow	cavity	0	W.F*

*** W.F:** water flume; **W.T:** wind tunnel.

The reference velocity in each study in this table is different. Despite the large number of studies, little available studies offer a consistent definition for the reference velocity to use in Eq. 1.2. This research provides a considerable amount of data with consistent variable definitions.

Despite all of the studies cited in table 1.1, no comprehensive study exists on the role of buoyancy on pollution dispersion from a street canyon with different aspect ratios and boundary layer properties. There is, therefore, still a need to understand and parameterize the interaction of wind and gas density for pollutants trapped in urban canyons with different dimensions. The goal of this dissertation is to provide both a qualitative and quantitative investigation of the effects of negative buoyancy on the flushing of a dense fluid from a canyon for different aspect ratios and upstream ABL properties. Wherever in this study it's referred to the term of "buoyancy" which is driven by density, it implies the negative buoyancy.

1.3 Problem definition

In terms of air quality management, there is clearly a need to understand the dispersion of a dense gas trapped in complex urban topography more fully. However, there are an infinite range of three-dimensional building arrays. The dispersion process in an urban area with highly crowded buildings is significantly different from that in flat terrain. The pollution trapped in the surroundings of an urban street with high-rise buildings can cause serious health risks because the dispersion process is significantly limited, and can result in poor air quality.

To avoid the endless complexity of general urban canopy geometry, this research focuses on the most basic trapping topography, the two-dimensional urban canyon. While this is a somewhat idealized geometry, it is a sensible starting point for the parameterization of shear-

driven vertical mixing of dense gas pollutants. Figure 1.3 schematically illustrates the simplest two-dimensional geometric components of an urban canopy and the major parameters considered. These are the building height H, the street width W, the atmospheric boundary layer properties and the pollutant density parameterized in terms of its reduced gravity, g'. The widths of the buildings, W, in this study are constant and are the same as the building height.

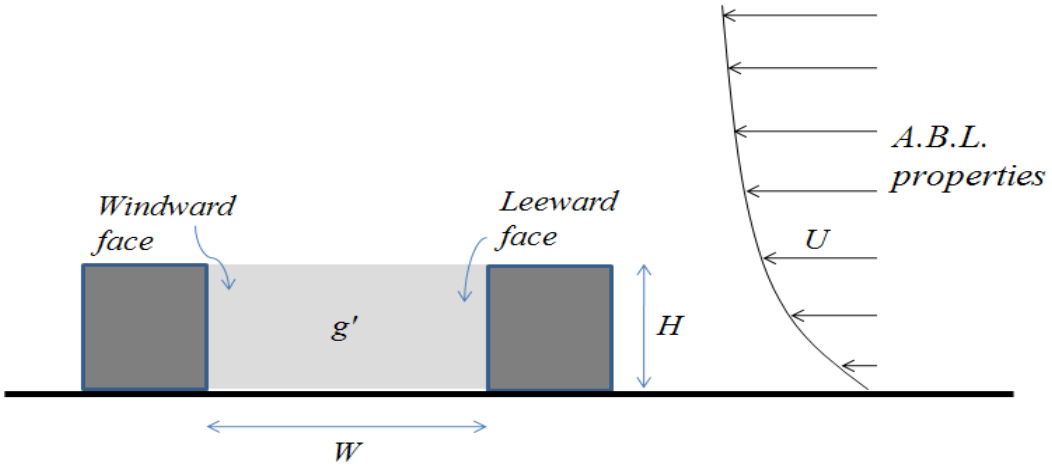

Figure 1.3: Schematic diagram of the street canyon showing geometric parameters. The windward side is that end of the canyon near the windward facing canyon wall, and the leeward side is the end of the canyon near the leeward facing canyon wall.

The variation in the total buoyancy in the canyon over time will depend on the initial pollutant buoyancy, g'_0, the canyon dimensions, and the properties of the upstream atmospheric boundary layer (ABL):

$$\int g' dA = f(g'_0, t, H, W, ABL) \qquad (1.4)$$

where t is the time from the start of flushing and A is the cross section area of the canyon shown in the Figure 1.3. There are a number of ways of parameterizing the atmospheric

boundary layer. For example, Jensen (1958) suggested that to attain dynamic similarity one must accurately account for the surface roughness of the upstream terrain. Estimation of this parameter is typically done either by examining the geometry of the upstream fetch, or by fitting a curve through measured velocity profile data. One can therefore parameterize the ABL in terms of the upstream velocity at the height of the roof top (U) and the upstream surface roughness height (z_0). This approach is commonly used for wind tunnel testing of wind loads on structures (ASCE 1999 and ASCE / SEI 7-10, 2010). Alternatively, one could follow the lead of Huang et al. (2000) and use the rooftop velocity and the rooftop turbulence intensity (I).

Defining

$$G = \int g' dA, \tag{1.5}$$

we can define the non-dimensional mean canyon buoyancy as

$$\Gamma = \frac{G}{g_0' HW}. \tag{1.6}$$

Time can be scaled using the canyon height and upstream roof top velocity,

$$\tau = \frac{tU}{H}. \tag{1.7}$$

Equation (1.4) can then be written in non-dimensional form as either

$$\Gamma = f\left(\tau, Ri, \eta, Je\right) \tag{1.8}$$

where $Je = H / z_o$ is the Jensen number (Cook 1986) or

$$\Gamma = f\left(\tau, Ri, \eta, I\right) \tag{1.9}$$

where I is the turbulence intensity of the upstream flow at the roof height. Having a source of buoyancy emission in the canyon adds another term to (1.9), accounting for the source buoyancy flux.

In this study, we will consider two basic cases, a finite release of pollutant (chapters 2, 3, & 4) and a continuous release (chapter 5). A release can be considered instantaneous if it is released over a period of time that is much shorter than the time it takes to disperse (such as an instantaneous release from a sudden rupture of a gas cylinder). It can be considered continuous if the dispersion time scale is significantly shorter than the release time such as a slow leak from a pipe.

1.4 Dissertation outline

This study presents an experimental and analytical investigation into the effects of buoyancy, canyon aspect ratio, and the properties of the upstream boundary layer on the flushing of a pollutant from an urban canyon. A range of canyon dimensions, pollutant densities, flow velocities, and turbulence intensities were considered in this research.

Chapter 2 describes the experimental methodology and quantifies the effect of the pollutant buoyancy on the flushing process and flow stratification in a canyon with aspect ratio one, under a rough turbulent boundary layer. Chapter 3 and 4 discuss the effects of the canyon aspect ratio and upstream boundary layer properties (rough and smooth turbulent boundary layers) on the in-canyon flow structure and purging process in the presence of buoyancy.

Chapter 5 presents results of experiments for which there was a continuous release of pollutant into the canyon, and includes an entrainment model for predicting the time evolution of both finite and continuous release flows. Chapter 6 provides a summary of results and the major conclusions of this research. Recommendations for future work are also presented in chapter 6.

CHAPTER TWO

BUOYANCY EFFECT

This chapter describes the effect of buoyancy on the mechanism and the rate of concentration removal from a canyon with aspect ratio one. An empirical equation based on the experimental investigation is presented to estimate the flushing time as a function of the Richardson number.

2.1 Introductions

Caton et al. (2003) examined the flushing of a neutrally buoyant pollutant from a square cavity due to a flow over the canyon top. They showed that a shear layer forms at the top of the canyon, and produces an exchange flow between the polluted cavity fluid and the fresh ambient fluid. For a finite initial release of pollutant, the cavity remains well mixed and the rate of exchange is constant, resulting in an exponential decay in pollutant concentration over time. The decay rate was found to be proportional to the flow velocity and inversely proportional to the height of the cavity.

For buoyant pollutants, the dispersion mechanism differs from that of passive pollutants. Atmospheric stability, thermal buoyancy, and dense gas pollution are all considered in street canyon flow studies.

Kim and Baik (2001) defined five different regimes for recirculating flow in a cavity based on different thermal conditions. Cheng et al. (2011), in a numerical study, considered the effect of a thermal stratification on urban street canyon flows and pollution transport for $Ri = -0.11, -0.06, 0, 0.18$, and 0.35. The bulk Richardson number was defined as

$$Ri = \frac{\alpha g H \Delta\theta}{U^2} \quad (2.1)$$

where α is the thermal expansion coefficient, g is gravitational acceleration, H is building height, U is free-stream flow velocity, and Δθ is the difference between street-level temperature and roof-level temperature. A negative Richardson number indicates relatively warm air in the canyon, a positive Richardson number indicates relatively cold air in the canyon, and Ri=0 indicates that the air in the canyon is the same temperature as the ambient air in the boundary layer flow. Based on their results, although pollutant removal is improved for unstable stratifications (Ri<0) because of turbulence enhancement, only the stable case showed a different flow pattern from the neutral situation, because the temperature inversion near the ground level suppressed turbulence and trapped most of the cool air at street level. Uehara et al. (2000) showed that for very stable conditions (Ri = 0.4 − 0.8), the wind velocity in the street canyon is suppressed and drops to zero. A similar study by Cheng et al. (2009) showed the effect of thermal buoyancy and the atmospheric stability condition on the pollutant removal time.

In terms of thermal buoyancy, most studies focus either on negative Ri number or on low Ri values, because the highest Richardson number reported for a stable atmosphere is about 0.2 for a stable atmospheric condition and a strong stable stratification is rarely caused by temperature differences (Liu et al., 2003). Study of higher Ri numbers is necessary for dense pollutants.

The removal of a negatively buoyant pollutant from a cavity has been examined numerically and experimentally. Chang et al. (2007b) conducted LES simulations of a cavity with aspect ratio of two for the neutrally buoyant case (Ri=0) and for a slightly negatively buoyant pollutant (Ri=0.2). They found that the dense pollutant took about twice as long to flush fully from the cavity. For the Ri=0.2 case the cavity did not stay well mixed and the decay rate was

not constant over time, but rather a density stratification was maintained throughout the flushing process.

The problem of the dispersion of a dense fluid from a cavity has also been applied to the study of salt water trapped in depressions of river beds. In this case, flushing is driven by the fresh water overflow from the river (Kurup and Hamilton, 2002; Coates et al., 2001; Debler and Imberger, 1996). For a cavity with aspect ratio one, Armfield and Debler (1993) conducted a laboratory study for six different Richardson numbers over the range $0.02 < Ri < 0.6$, to identify the mixing characteristics and verify their numerical simulation results. Four stages were identified during the purging process: 1) the initial large splash of dense fluid; 2) forming a vortex at the interface height and resultant splash; 3) seiching interface surface which ejects the dense fluid continuously from the cavity; and 4) forming a vortex inside the cavity which moves the dense fluid out of the basin. The first three stages occurred due to the large scale flow while the last stage is due to the small scale turbulent flow (Kirkpatrick et al., 2012).

Debler and Armfield (1997) considered both rectangular and trapezoidal cavities and Richardson numbers in the range $0.45 < Ri < 31$. They parameterize the rate of flushing and the entrainment velocity at the interface as a function of the cavity geometry, Ri number, layer thickness, the upstream flow depth, and velocity. However, their model only accounts for flushing by skimming of dense fluid from the top of the dense layer and does not consider mixing across the density interface, nor the role of upstream turbulence intensity on the flushing rate.

This study was extended by Kirkpatrick and Armfield (2005). It was assumed that the flushing process was largely due to skimming of dense fluid off the top of the layer rather than via an exchange flow across the density interface. Kirkpatrick et al. (2012) in a similar study

considered wide trapezoidal canyons with 7<η<17. It was shown that the entrainment rate at the interface surface can be defined by only a power-law function of the Richardson number. This study also focuses on the strongly stratified fluid in the cavity (high Ri) when it is assumed that the density of the layer does not decrease.

All these studies were run with a shallow overflow, and are consequently not appropriate for atmospheric boundary layer modeling in which the flow depth is effectively infinite. A cavity-flushing study with a deep upstream turbulent flow was conducted by Strang and Fernando (2004). They ran experiments on flushing of saline water from rectangular cavities with η=1 and 2, but they mainly focused on the flow and concentration downstream of the cavity. This chapter seeks to quantify the effect of buoyancy (Ri number) on the flushing process for a square canyon. The specific problem considered is that of the removal of a finite volume of dense fluid from a canyon due to vertical mixing driven by a turbulent flow over the top of the buildings.

The remainder of this chapter is structured as follows. The experimental technique and procedure is described in section 2 followed by the results and a qualitative description of the observed flow in section 3. Quantitative parameterizations of the flushing rate are given in section 4. Conclusions are drawn in section 5.

2.2 Experimental technique

A series of small-scale laboratory experiments were conducted in the water flume of Lowry Hall Fluid Mechanics Laboratory to measure the time taken to remove a dense layer of fluid from a square canyon as a function of the flow Richardson number. A series of experiments were conducted in a water flume using a canyon formed by two parallel square prisms whose

axis is horizontal and normal to the flow. The building height is denoted by H, the canyon width by W, the wind speed at the top of the blocks by U, and the total flow depth is D. The length of the canyon in the transverse direction and the depth of the ambient fluid were assumed to be high enough to have no effect on the flushing process. The fluid density is parameterized in terms of its buoyancy. A schematic of the flow considered is given in Figure 2.1.

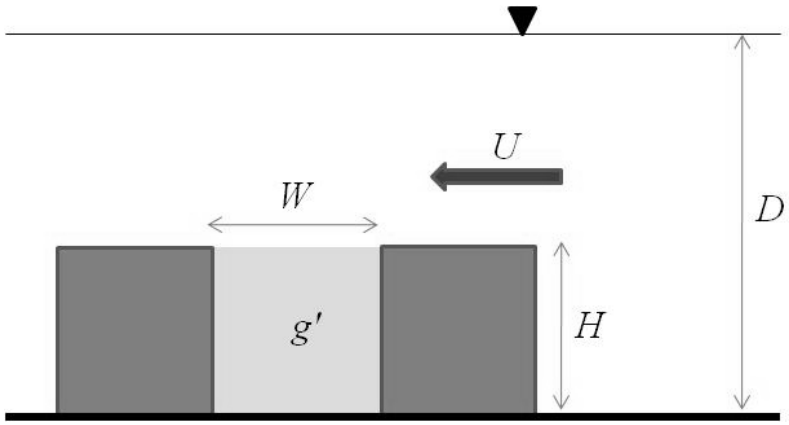

Figure 2.1: Schematic diagram of the problem considered showing the building height H, the cavity width W, the flow depth D, and the pollutant density parameterized in terms of its buoyancy g'.

Water channels can be used to physically model the street-canyon flow (see, for example, Li et al., 2007; Baik et al., 2000; Liu et al., 2003; Kim and Baik, 2005; and Caton et al., 2003). Although salt bath laboratory experiments are run on a smaller scale than are large wind tunnel or field studies, they can provide great insight into large-scale flows such as volcanic eruptions (Woods et al., 1992), mixing in the ocean (Hughes and Griffiths, 2006; Wahlin and Cenedese, 2006), and air movement in buildings (Kaye and Hunt, 2004; Linden et al., 1990) They succeed for three main reasons. First, the kinematic viscosity of water is a factor of 10 less than that of air, meaning that equivalent Reynolds numbers can be achieved on a smaller scale using

water as the working fluid. Secondly, it is easier to control the boundary conditions as temperature fluctuations make only a slight difference to the density as compared to the salinity. Finally, flow visualization and measurement are considerably easier as the liquid can be dyed, high salt concentrations can be used compared to those of tracer gases, and its concentration can be measured using a light attenuation technique (described in this section) without placing instrumentation within the flow.

The following sections describe the experimental setup instrumentation, buoyancy measurement and experimental results for measuring the effect of buoyancy on the flushing rate. Since all the experiments were run for a single Schmidt number and high Re number ($7500 < Re = \frac{UH}{\upsilon} < 13000$), the flow is insensitive to Re and Sc (Kirkpatrick et al., 2012; Meroney et al., 1996).

2.2.1 Experimental setup

The canyon pollution dispersion was modeled in a Plexiglas water flume using fresh water as the ambient environment and dyed salt water as the buoyant pollutant released in between the model building blocks representing the urban canopy. The experiments were run in a free surface water flume which is 10 m long and 0.6 m wide, and was run at a depth of between 0.4 and 0.5 m. The flow is driven by a 0.08 m^3/s capacity pump controlled by a variable frequency drive. The flow was controlled downstream by a rectangular sharp crested weir of height 0.38 m above the channel bed. The weir was located 2 m downstream of the test section. Upstream the flow passed over a weir wall, into a header tank, and then through a contraction and flow straightener into the main channel. Figure 2.2 depicts the flume along with the water recirculation set up.

To model the urban boundary layer, a rough turbulent boundary layer was generated using a gravel bed (d_{84}= 1.14 cm), laid over a 7.5 m length of the channel, upstream of the test section.

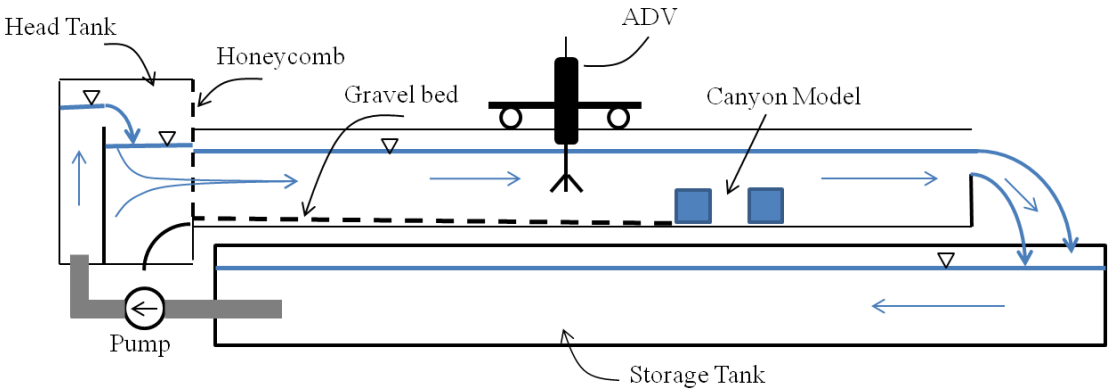

Figure 2.2: Schematic diagram of the flume section

The velocity measurements were made using a SonTek 10-MHz ADV (Acoustic Doppler Velocimeter) that is capable of measuring all three components of velocity with an accuracy of 0.25 cm/s at a sampling rate of 25 Hz. To verify that the velocity profile is fully developed at the test section, velocity profile measurements were made at three different sections upstream of the test section. The mean velocity and turbulent intensity profiles taken at the highest flow rate for a gravel bed of size d_{84}=1.14 are shown in Figure 2.3 along with the best fit logarithmic profile.

$$u(z) = \frac{U_*}{k} \ln\left(\frac{z}{z_0}\right) \tag{2.2}$$

in which $u(z)$ is the time averaged velocity at the height of z, z_0 is the surface roughness, U_* is shear velocity, and k is the von Karman constant.

A surface roughness length of z_0 =0.24 cm was found from analyzing the profiles using the techniques of Smart (1999) and Karimpour et al. (2012). Since all the acoustic receivers of the ADV must be underwater to measure the velocity at 10 cm distance, the top 10 cm of the profile could not be measured. The ADV was also used during each experiment to measure the mean rooftop velocity (U) and turbulence intensity (I) defined by the root-mean-square value of the time series of individual velocity (u_{rms}) about the mean velocity$U$. To ensure that the flow is independent of the Reynolds number, the rooftop velocity was chosen such that $Re > 7500$ (Meroney et al., 1996). When the inflow velocity is higher than 6 cm/s, the turbulent intensity is independent of (U).For all experiments in this chapter, I (defined as root mean square of time series at the top of the blocks was 13%<I<16%.

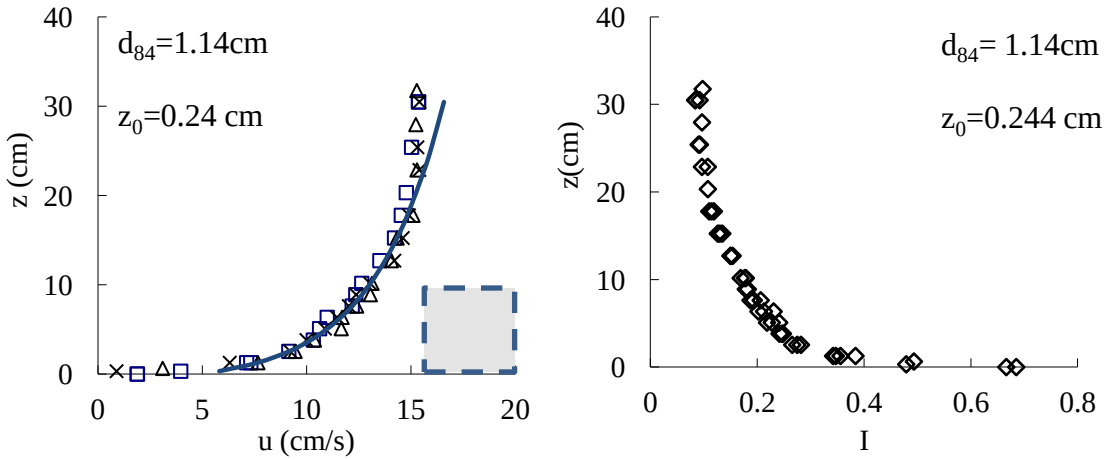

Figure 2.3: a) Vertical velocity profile data (points) and fitted curve (line) based on Eq. 2.2, for d_{84}=1.14 cm, z_0 =0.24 cm and U_* =1.36 cm/s. b) The total turbulence intensity profile. The block represents the heights of the model buildings.

Buoyancy measurements were made using the light attenuation technique. Figure 2.4 illustrates the flume test section and the cavity model along with the measurement instruments. The flume's Plexiglas sidewalls allow videotaping the process during the test runs. A fluorescent lighting system at one side of the flume is used as back light for the flow. A light diffusing screen makes the back light almost uniform. The canyon was formed by two hollow square prismatic buildings of height 0.1 m and width 0.6 m, equal to the width of the flume. The depth of the flow was always approximately four times the height of the buildings. The Jensen number (Cook 1986), which parameterizes the height of the building relative to the boundary layer surface roughness, was $Je = H / z_0 = 42$ (Jensen, 1958).

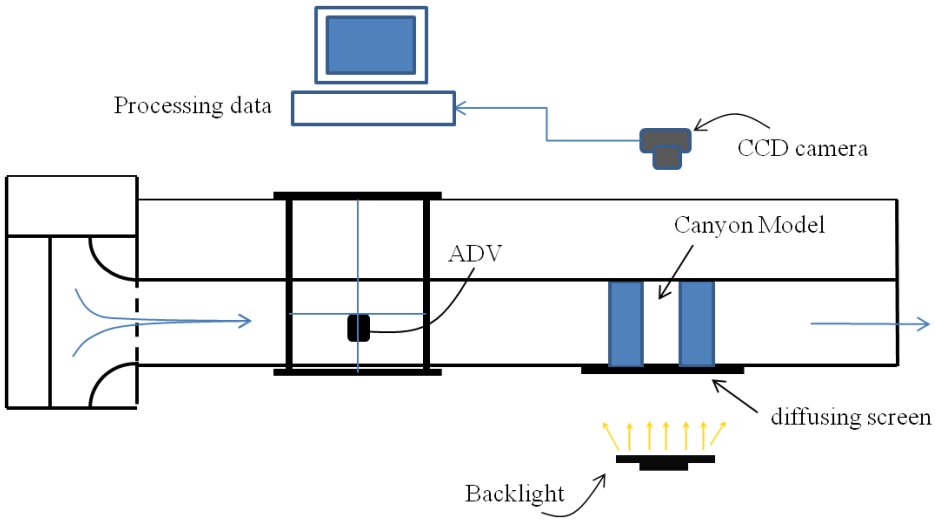

Figure 2.4: Plan view of the canyon model, test section, and measurement instrument.

A schematic diagram of the experimental model is shown in Figure 2.5. Salt water was introduced into the already flooded canyon through a perforated pipe that ran along the canyon floor across the whole width of the canyon transverse to the flow direction.

The salt water was supplied from a constant head tank. The rate at which the salt water was introduced was controlled by a needle valve attached to an inline rotameter flow rate meter. The flow rate was kept very low so that there was minimal mixing of the salt water with the fresh water as the salt water left the perforated pipe.

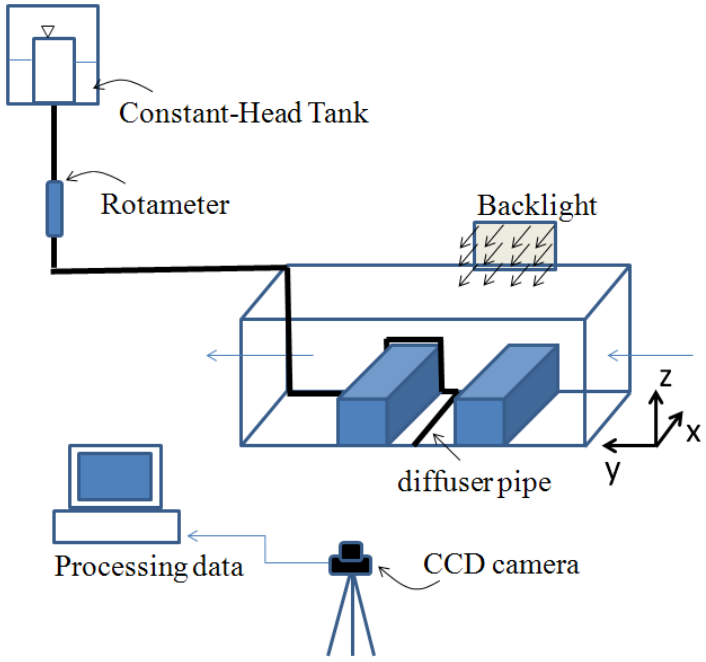

Figure 2.5: Schematic diagram of the experimental test section showing the buildings forming the canyon, the backlighting, CCD camera for measuring light attenuation, and the salt water supply system.

2.2.2 Buoyancy measurement

The buoyancy of the fluid in the canyon was measured using a light attenuation technique (Hacker et al, 1996; Cenedese and Dalziel, 1998; Allgayer and Hunt, 2012) in which the buoyant fluid is dyed and the light attenuation across the canyon is related to the fluid buoyancy. The technique is based on the Beer-Lambert law of absorption, which states that the

light intensity's local spatial attenuation rate is linearly proportional to the local light intensity and dye concentration. Thus,

$$\frac{dI_l}{dx} = -\gamma_a I_l \tag{2.3}$$

where I_l is the light intensity, x is the direction of the light beam, and γ_a is a property of the medium attenuating the light. The measurement technique relies on γ being a linear function of the dye concentration and the experiment being two-dimensional. If both these conditions are satisfied, then (2.3) becomes

$$\frac{dI_l}{dx} = -K_a C I_l \rightarrow \frac{I_l}{I_{l0}} = e^{-K_a CL} \tag{2.4}$$

where C (ppm) is the local dye concentration, K_a (ppm m) is the constant of proportionality relating γ_a to C, I_{l0} is the light intensity prior to passing through the dyed fluid, and L (m) is the length of the path through the dyed fluid. The resulting measurement gives the dye concentration at any location in the streamwise (y) and vertical (z) directions averaged over the transverse width (L) of the canyon. In present experiments, the light intensity was measured using a JAI CV-M4+CL black and white CCD camera with 1392 (h) x 1040 (v) 6.45 µm square pixels per image. The camera has a linear relationship between light intensity and digitized signal, though it does have a zero offset I_{lz} that was calculated by averaging the measured intensity with the lens cap on (Coffey, 2006).

A series of experiments were run with different dyes and a range of lens filters to establish which combination provided the most linear relationship between concentration and attenuation rate. The resulting experimental setup used a commercial red food coloring and a combination of blue and green lens filters to achieve the highest light sensitivity for the camera

while remaining in the linear attenuation range of the dye. Figure 2.6 shows the light intensity that was considered in all experiments in order to be in the range of linear relationship ($0.2 < \frac{I_l}{I_{l0}} < 1$).

The concentration was calculated by taking an experimental image and dividing the measured light intensity at every point by the light intensity measured at the same point in the absence of any dyed solution. Thus,

$$C(x,y) = \frac{1}{K_a L} \ln\left(\frac{I_l - I_{lz}}{I_{l0} - I_{lz}}\right) \tag{2.5}$$

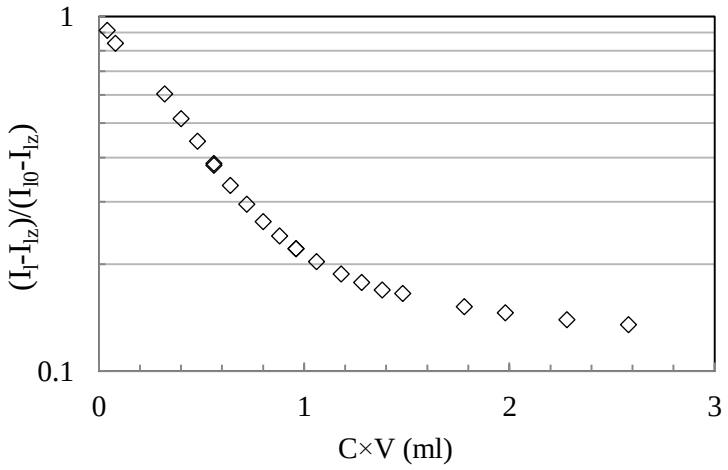

Figure 2.6: Light sensitivity for green and blue lens filters (V is the cavity volume).

where I_{lz} is the digitized black offset for the camera. All image processing and attenuation calculations were made using a DigiFlow software package (Cenedese and Dalziel, 1998). The constant of proportionality K was calculated by taking a series of measurements within the

canyon with different measured dye concentrations, plotting the log of the measured attenuation against the concentration, and fitting a straight line through the data.

To calculate the buoyancy based on the concentration, the technique requires that the dye and the salt mix at the same rate that is, the dye concentration is directly related to the buoyancy at all times. This is valid provided the Peclet number ($Pe = \frac{UH}{\kappa_D}$) is large for both the dye and salt, as was the case for present experiments. Also this has been verified during preliminary experiments (Figure 2.7).

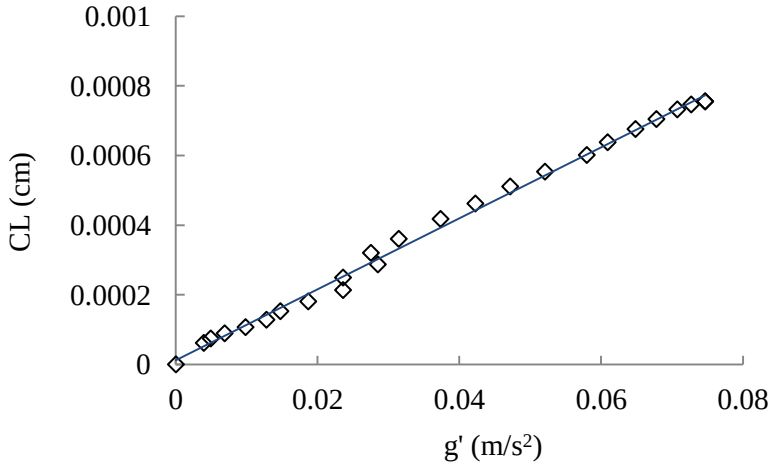

Figure 2.7: Dye concentration and buoyancy relation based on the experimental tests.

2.2.3 Experimental procedure

Each experiment was conducted using the same procedure. First, a batch of dyed salt solution was mixed, ensuring that the dye concentration was still within the linear attenuation range based on the earlier calibration. The density of the dyed solution in the constant head tank was measured using a hand-held Densito 30 PX densitometer (accuracy ±0.0001 gcm^{-3}). The flume was then filled with fresh water up to the height of the weir wall (38 cm) and its

density was measured. The temperature difference between fresh and salt water was also measured and found to be negligible (around one degree Celsius) for all experiments. When the flume was full of fresh water and before adding salt water to the canyon, an image was taken to give the background light intensity. The dyed salt water was then slowly drained from the constant head tank into the canyon in the flume which was already flooded by fresh water with depth of 40- 50 cm. Once the canyon was full (Figure 2.8), a sample of the salt water inside the cavity was taken, using a syringe with a long needle, to check the initial density. Then the camera started recording and the flume was turned on to the desired flow rate. During the experiment, the velocity upstream of the model buildings, U, was recorded using the ADV at the height of the top of the buildings. The time average of the steady velocity was taken as the reference velocity for the flow. Images were recorded every 0.15 to 1 seconds, depending on the expected rate of flushing (fewer frames per second were recorded for lower flow velocities and higher fluid densities). Filming was ended when the canyon was fully flushed based on visual inspection of the canyon.

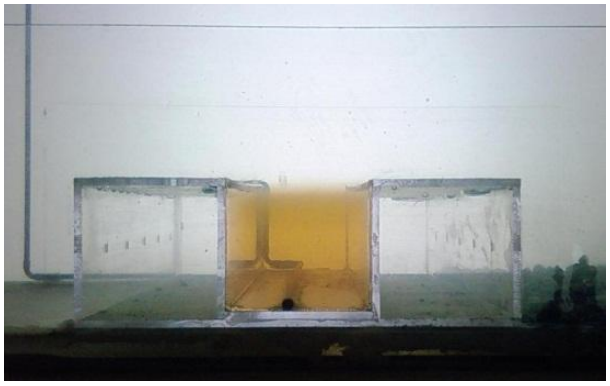

Figure 2.8: The flooded flume with the canyon space full of dyed saltwater.

After an experiment each frame of the movie was used to calculate the concentration and hence buoyancy at each point in the canyon cross-section using (2.5). Figure 2.9 shows the background subtraction and the final light intensity at each pixel of the image.

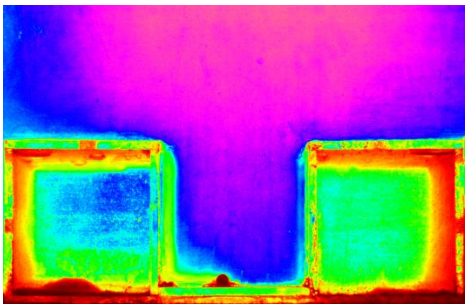

(a)

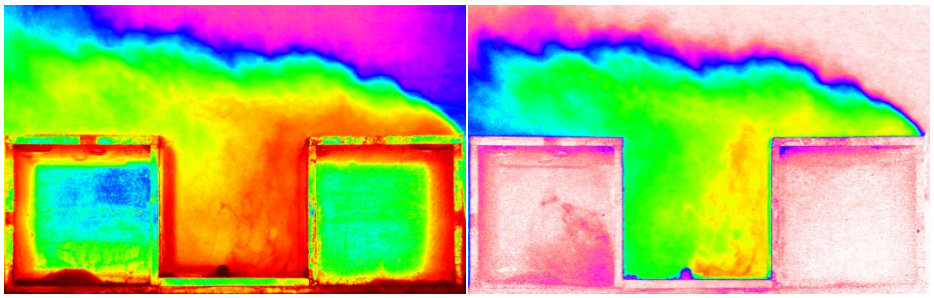

(b) (c)

Figure 2.9: a) Background image before experiment, I_0, b) a captured image during the test, I_l, c) corrected image with the light intensity $(I_l - I_{lz})/(I_{l0} - I_{lz})$. The false colors map the intensity of the light.

Using the Digiflow software, a horizontal average of the buoyancy was then calculated at each height for each frame to give vertical buoyancy profiles over time. An example of the calculated horizontal averaged profiles is shown in Figure 2.10.

The filling tube at the bottom of the canyon blocked all light at 1 cm height of the canyon, preventing the attenuation technique being used all the way to the canyon base.

Therefore, the buoyancy measurement at the top of the tube was taken to represent the buoyancy below the tube top. The area averaged buoyancy, g_0', was also calculated for the canyon. In the results presented in this chapter, the buoyancy is scaled on the initial mean buoyancy in the canyon

$$\gamma = \frac{g'}{g_0'} = \frac{g'H}{\int_0^H g'(t=0)dz} \tag{2.6}$$

and vertical distance from the canyon floor (z) is scaled on the canyon height

$$\zeta = \frac{z}{H}. \tag{2.7}$$

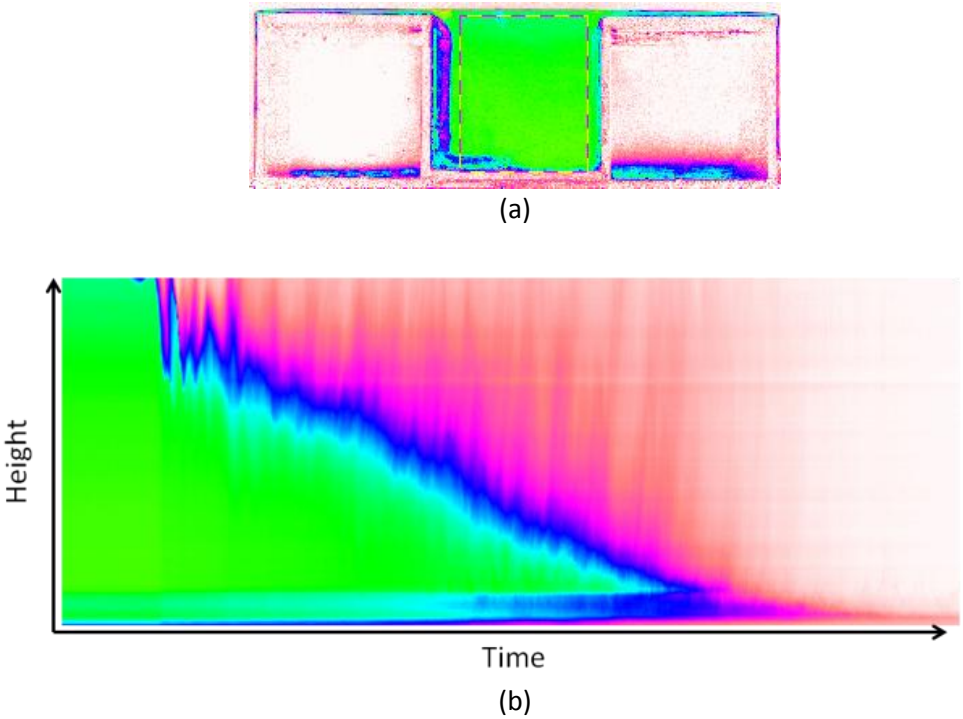

(a)

(b)

Figure 2.10: a) The captured area for buoyancy calculation; b) Horizontal average profiles of the canyon over time.

2.3 Flushing mechanics and flow descriptions

A total of 26 experiments were run for a range of Richardson numbers ($0.08 < Ri < 4.5$) and for an aspect ratio η=1. The flow regimes observed followed by a discussion of the stratifications measured for different Richardson number flows are described below.

2.3.1 Observations and flow regimes

A number of flow regimes were observed depending on the Richardson number of the flow. For higher Richardson numbers, the canyon remained strongly stratified during the flushing process, whereas for lower Richardson numbers it was relatively well mixed throughout the flushing. Despite the different stratifications observed, the initial mechanics of the flushing process was similar in all cases. After the flume was turned on to the desired flow rate, the fresh water over the flooded canyon was set into motion and started purging the saline water out of the basin. The general purging process was similar to what Armfield and Debler (1993) reported. Each experiment roughly followed the same four steps. Experimental images of these four stages are shown in Figure 2.11 for an aspect ratio $\eta = 1$ and a Richardson number of $Ri = 0.1$.

a) When the flume is initially turned on, the shear from the flow over the top of the canyon tilts the interface at the top of the dense fluid layer. The interface is depressed at the upstream end of the canyon and raised at the downstream end. This tilting results in a slug of fluid being pushed out of the downstream end of the cavity. This slug of fluid is then rolled up into a trailing edge vortex downstream of the second building (Figure 2.1b).

The initial condition of the experiments and the abrupt splash of dense fluid from the canyon might play major role in initial purging process and affect the rate of flushing. This influence will be discussed in Section 5.4.2.2.

b) The upstream depression formed during the initial tilting moves downstream in the form of an interfacial wave. In some cases dense fluid is rolled up into a vortex at the top of the wave as seen in Figure 2.11(b). This roll up is less pronounced for higher Richardson numbers (see Figure 2.14). For more stable Richardson numbers, the wave simply travels across the cavity. As the wave progresses, the fluid slug that was initially pushed out of the back of the cavity is pinched off.

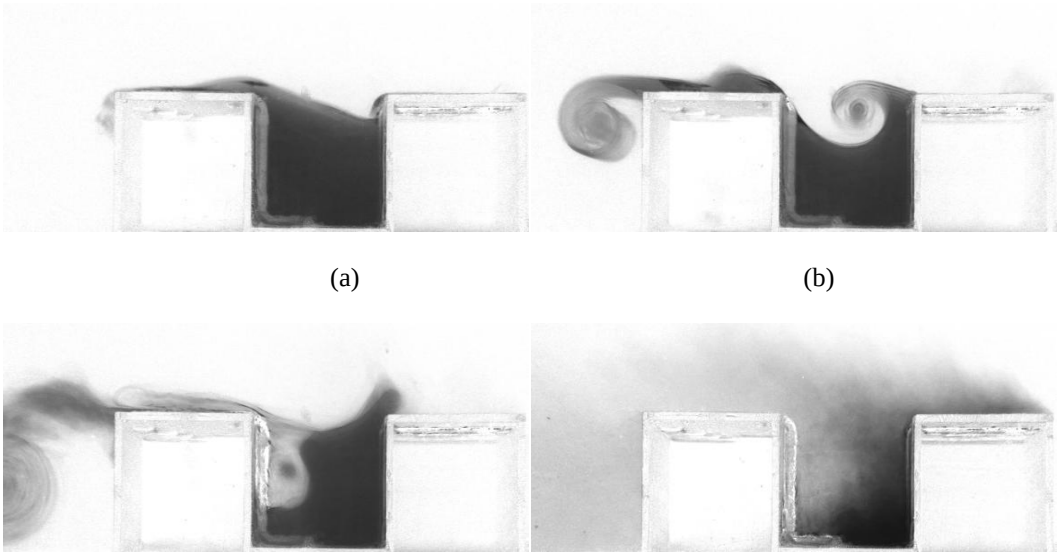

(a) (b)

(c) (d)

Figure 2.11: Series of images of the buoyancy field for a Richardson number of Ri=0.1 and a square cavity, showing, a) the initial tilting (t =5 s), b) interfacial wave (t=7 s), c) vortex penetration into the cavity at the downstream end (t =10 s), and d) the quasi-steady flushing of the dense fluid out of the cavity (t =26 s). Also shown in the last image is buoyant fluid being driven upstream to the flow separation point at the building's leading edge.

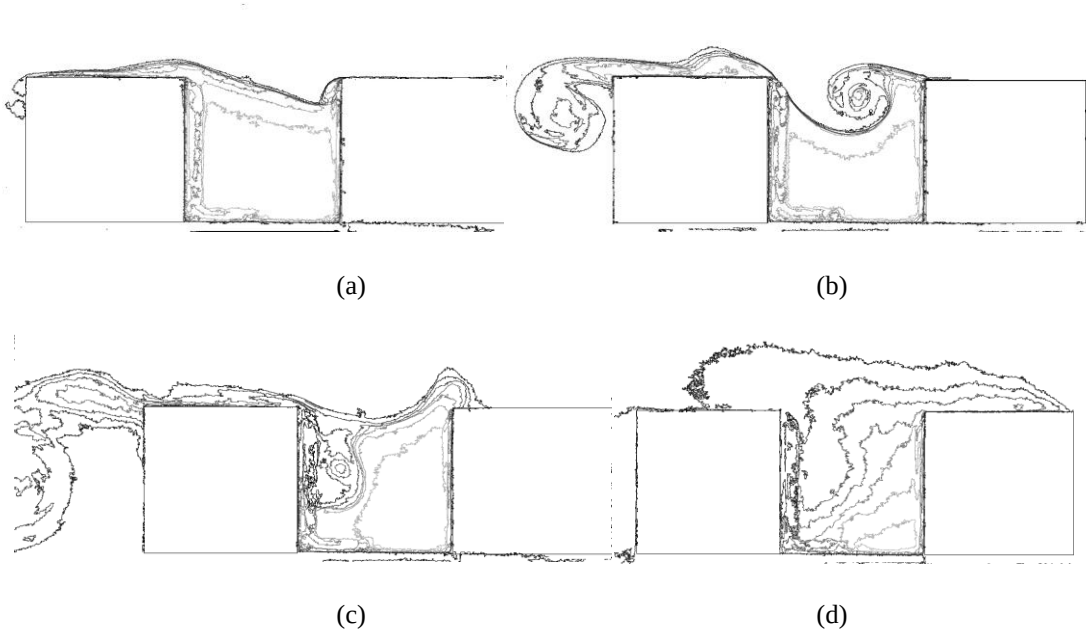

Figure 2.12: Corresponding density contours for images in Figure 2.11 showing 10% spacing between isopycnal contours.

c) When the wave reaches the downstream edge of the cavity, the trough is deflected down into the cavity and a recirculation zone is established that is maintained for the duration of the flushing. The initial depth of the recirculation zone is strongly dependent on the Richardson number of the flow. The higher the Richardson number, the more stable the stratification and the smaller the vertical penetration depth. For lower Richardson numbers this recirculation zone extends all the way to the base of the cavity.

d) After the recirculation zone is formed, a steady flushing flow is established in which fluid is mixed into the recirculation zone and flushed out the top of the cavity. Once out of the cavity, the dense fluid was drawn upstream due to the low pressure created by the flow separation at the leading edge of the upstream building (consistent with Meroney et al., 1996). The dense fluid is then mixed across the shear layer formed at the leading edge and transported

downstream. Some of this fluid is transported fully downstream while some becomes trapped in the wake behind the downstream building.

The density contours for corresponding images in Figure 2.11 are shown in Figure 2.12 in order to show the change in concentration over the depth.

Although these four basic stages occurred in all the experiments, the mechanism of the purging process and the distribution of buoyant fluid within the cavity were observed to be strongly dependent on the Richardson number. Figure 2.13 shows the depth of the scaled initial interface deflection, d/H, at the upstream cavity edge as a function of the Richardson number: the higher the Richardson number, the more stable the layer and the smaller the deflection depth.

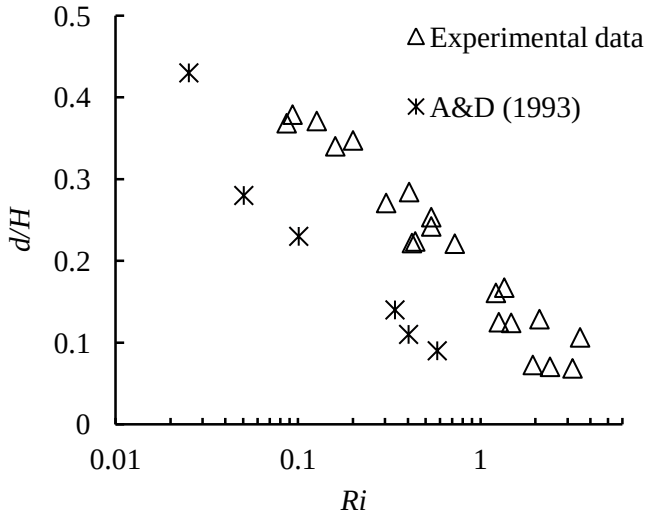

Figure 2.13: Non-dimensional initial deflection against Richardson number (triangles) and first splash fractional volume measurements from Armfield and Debler (1993) (stars).

Also shown in the Figure are the data from Armfield and Debler (1993) for the fractional volume of the initial slug of fluid pushed out of the cavity: again, the higher the Richardson

number, the lower the volume of the initial purge. Since the data from Armfield and Debler (1993) are for the average interface drop caused by the initial splash, the results are not directly equivalent, and it is expected to be lower than the initial deflection results reported for this study's results as observed.

The Richardson number also greatly influences the buoyancy profile in the canyon during the flushing process. False color images of the reduced gravity field for different Richardson numbers are shown in Figure 2.14: the lower the Richardson number the greater the initial deflection of the interface and the deeper the initial vortex penetrates at the downstream wall of the canyon. For the lowest Richardson number shown, the second wave is strong enough to roll up the light fluid and generate another vortex; it eventually penetrates to the base of the cavity, and the dense fluid is held at the upstream end of the cavity and flushed from there. As the Richardson number increases, the depth of the steady vortex decreases and the slope of the interface between the vortex and the dense layer decreases. For very high Richardson numbers, there is no significant steady vortex penetration and a two-layer stratification is observed. Further, as the Richardson number increases, the interface becomes sharper as seen by the more rapid vertical color gradients.

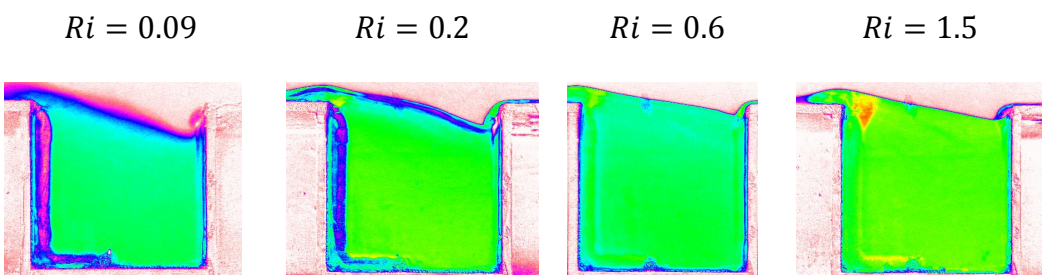

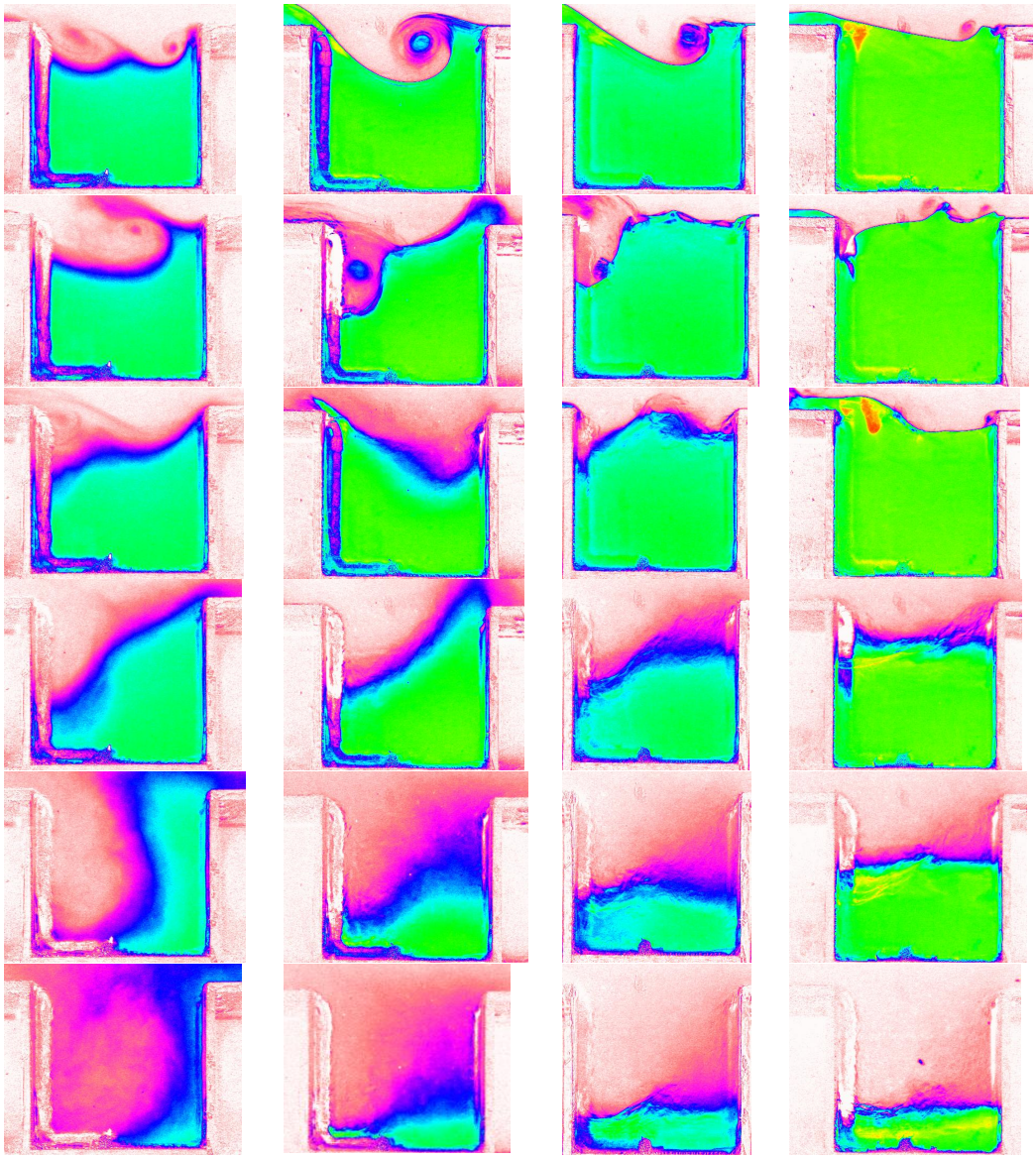

Figure 2.14: False color images of the flushing of a square cavity at different Richardson numbers (Ri increases from left to right). The times for each Ri number are: Ri=0.09, tU/H =1.7, 9.5, 11.5, 16, 19.5, 22; Ri=0.2, tU/H =4, 6.5, 11.5, 16.5, 25.5, 54, 76.5; Ri=0.6, tU/H =3.7, 6, 7.5, 13.5, 66, 124.5, 180; Ri=1.5, tU/H =5, 6, 7.5, 9.7, 126, 390, 464.

Buoyancy measurements inside the canyon showed three different buoyancy profile behaviors:

Well-mixed Flow: For low Richardson numbers, the initial vortex penetrates to the bottom of the cavity, the flushing is quite rapid, and the resulting mean vertical reduced gravity profile is approximately uniform with height decaying in magnitude over time. The cavity remained largely well mixed in a manner similar to that of the neutrally buoyant case, as demonstrated by Caton et al. (2003).

Continuously stratified flow: For intermediate Richardson numbers, the horizontally averaged buoyancy increases continuously with height above the cavity base. The vortex located at the downstream wall does not penetrate to the base of the cavity and so a stable stratification is maintained throughout the flushing.

Two-layer stratification: For high Richardson numbers, the dense layer is more stable and a distinct two-layer stratification is observed with a sharp density interface between the relatively fresh upper layer and relatively dense lower layer. Unlike the other two cases, the vortex was not able to persist in the canyon to mix the layer, so the purging process, at the beginning, was predominantly due to the shear layer at the top of the cavity. The interface oscillates, intermittently pushing dense fluid out from the upstream and downstream corners. This process continued until the level of the interface dropped to around one fourth of the cavity height below the top. After this, the dense layer was skimmed by a vortex formed at the downstream end of the upper part of the canyon. The scouring process continued to lower the interface toward the bottom of the cavity.

Table 2.1 shows the flow regimes in each range of Richardson number based on present experiments. Armfield and Debler (1993) and Debler and Armfield (1997) reported all their data for $0.02<Ri$ as being in the two layer regime. However, they use a different reference velocity

and cavity geometry. Further, they did not attempt to measure the vertical variation in pollutant density so would not have been able to distinguish between the different stratifications.

Table 2.1: Flow regimes in isolated canyon with aspect ratio 1 based on Richardson number.

Flow regimes	Well-Mixed	Continuous Stratified	Transition	Two-layer stratification
Ri	0 ---------- 0.09	---------- 0.3	---------- 0.8	----------∞

To illustrate the flow regimes described above, contour plots of the buoyancy field for Ri=0.091, 0.2, 0.6, and 1.5 are shown in Figure 2.15. The plots are all taken when 70% of the time taken to flush the cavity completely had elapsed. For the lowest Richardson number flow (far left) no significant vertical buoyancy gradients are observed and the horizontally averaged buoyancy profile is approximately uniform with height. For Ri=0.2, the downstream vortex can be seen to have penetrated most, but not all, of the way to the cavity base. There are vertical gradients but, except right at the base on the downstream end, the gradients are not high. As the Richardson number increases further, there is a transition toward a distinct two-layer stratification as seen for Ri=1.5.

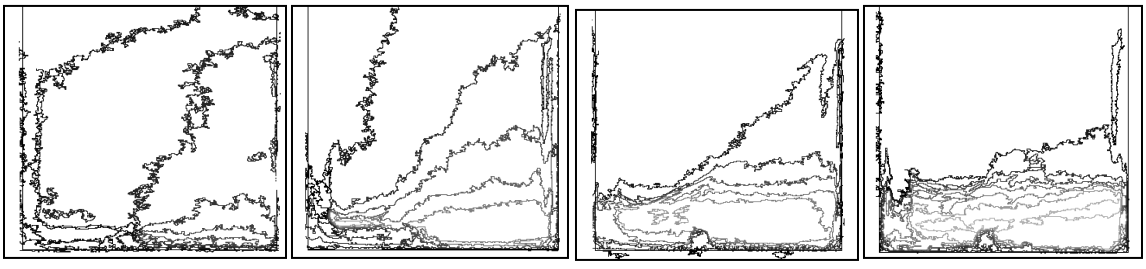

Figure 2.15: Buoyancy contour plots for, from left to right, Ri=0.091, 0.2, 0.6, and 1.5. The plots are taken when 70% of the time taken to flush the cavity completely has elapsed.

Sample sets of reduced gravity profiles are shown in Figure 2.16 for a range of Richardson numbers. For two-layer flow (Figure 2.16d) the gradient at the inflection was large compared to the mean gradient across the cavity depth and two layers are clearly identifiable. When the density gradient increased monotonically with height, but there was a non-significant inflection in the profile, the flow regime was considered as transitional (Figure 2.16c). Though all care was taken to eliminate mixing during the setup for each experiment, the canyon would still have a slight variation in buoyancy with depth. Therefore, the initial non-dimensional buoyancy toward the bottom of the canyon was greater than one.

2.3.2 Buoyancy stratification

For higher Richardson numbers, a distinct two-layer stratification is observed. The height of the interface between these two layers decreases over time as dense fluid is scoured off the top of the layer. The measured, horizontally averaged vertical buoyancy profiles were analyzed in order to track the interface height over time. The interface height was taken to be the point in the normalized buoyancy profiles, $\gamma(\zeta)$, with the highest vertical gradient: that is, the interface height is at ζ_i such that

$$\left(\frac{d\gamma}{d\zeta}\right)_{\max} = \gamma'_{max} \tag{2.8}$$

The thickness of the interface, δ, was assumed to be the vertical distance between the two points in the buoyancy profile such that

$$\frac{\gamma'}{\gamma'_{max}} = \frac{1}{e}. \tag{2.9}$$

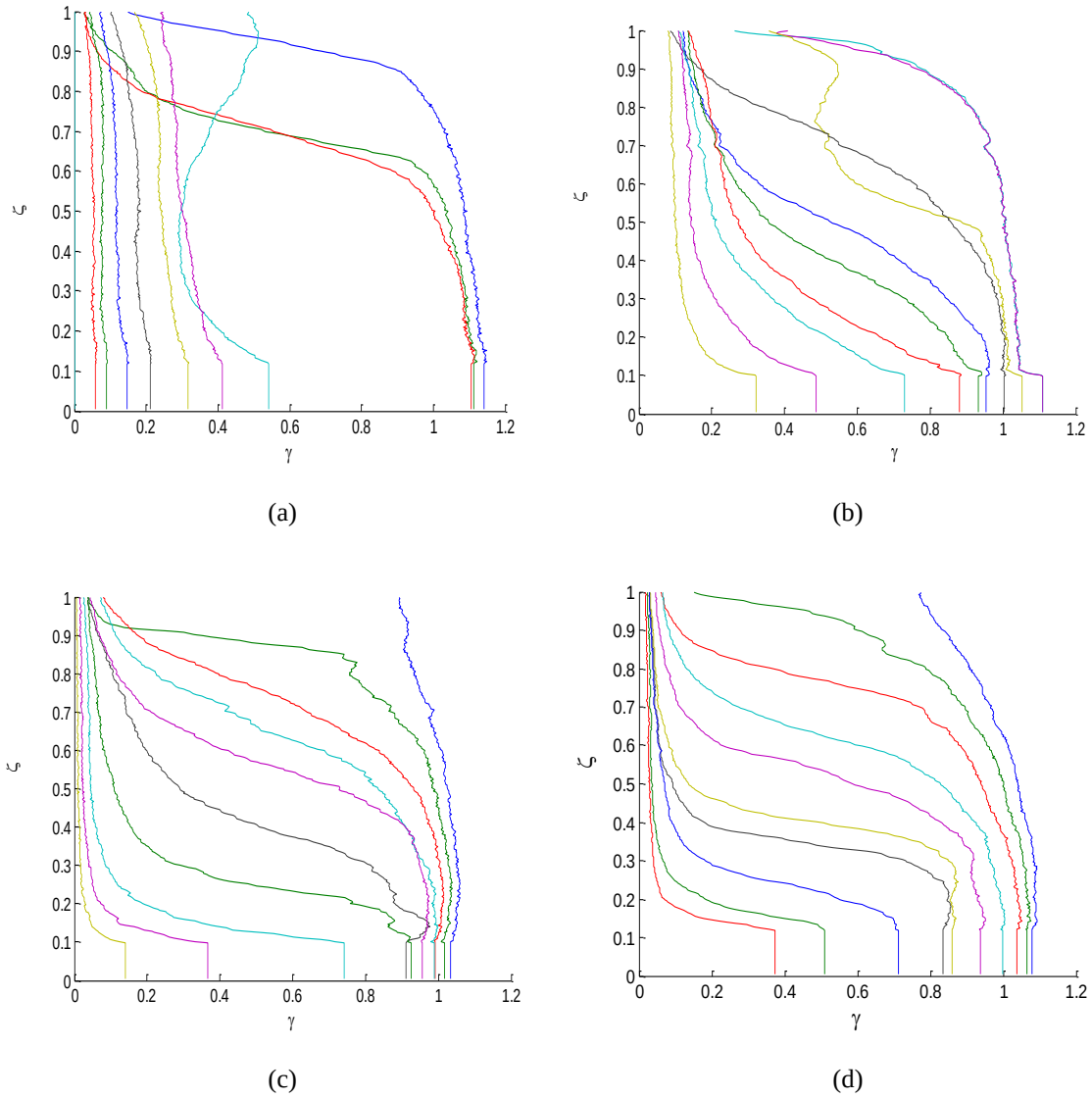

Figure 2.16: Sample scaled reduced gravity profiles for different flow regimes. (a) Well mixed (Ri=0.09), showing approximately vertical profile lines after the initial vortex penetration phase. (b) Continuously stratified ($Ri = 0.2$), showing decreasing density with height but no clear two-layer structure. (c) Transitional ($Ri = 0.6$), showing profile inflections but no high gradient layer interfaces except very late in the test. (d) Two-layer ($Ri = 1.5$), showing a relatively sharp interface between the lower dense layer and the upper ambient layer throughout the experiment. Profiles are at equal time intervals for each test.

These two definitions for the interface height and the interface thickness are illustrated in Figure 2.17. Sample buoyancy and buoyancy gradient profiles at different times for Ri=1.94 are shown in Figure 2.18.

An example of the interface height (ζ_i) calculation is shown in Figure 2.19, superimposing the graphical horizontal average buoyancy in the cavity over time, τ. Time is scaled using the upstream rooftop height velocity and the canyon height to give a reference time $T_{ref} = H/U$ and a non-dimensional time given by

$$\tau = \frac{t}{T_{ref}} = \frac{tU}{H} \tag{2.10}$$

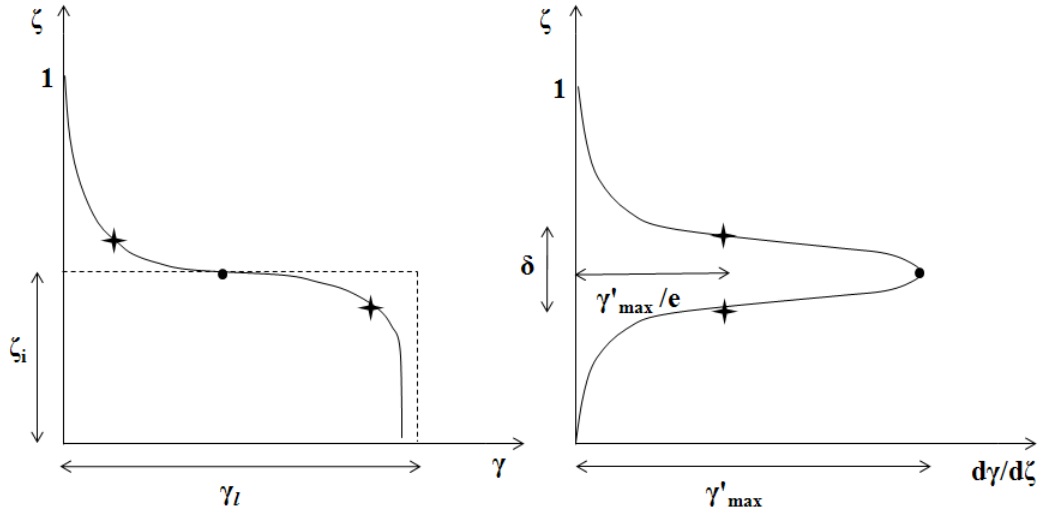

(a) (b)

Figure. 2.17: Graphical illustration of definitions for non-dimensional (a) interface height, ζ_i, buoyancy of the layer, γ_l, and (b) thickness of the density interface, δ.

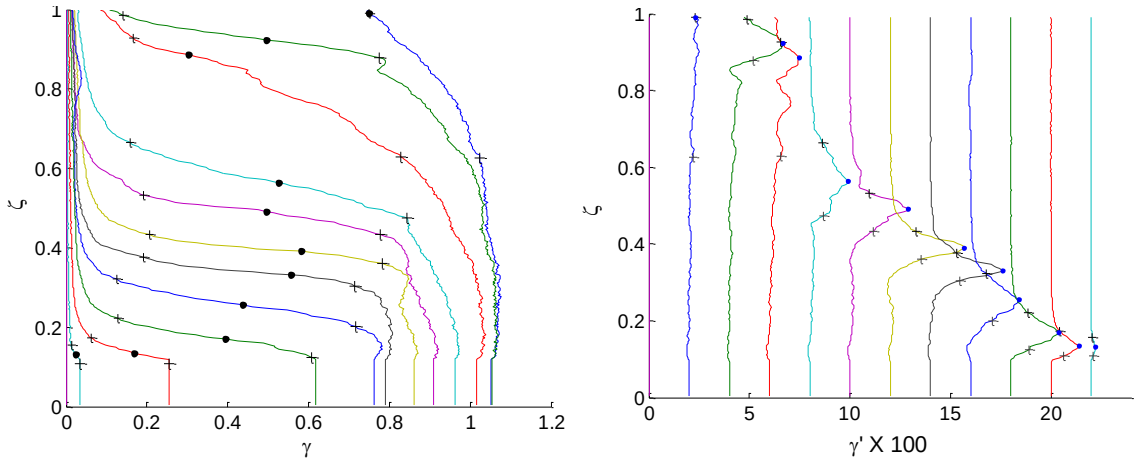

Figure 2.18 (a) buoyancy profiles and (b) corresponding buoyancy gradient, γ'. Profiles at equal time intervals for Ri=1.94. The dots represent the interface height and the + signs represent the upper and lower limits on the interface. The gradient profiles in (b) are offset from each other for clarity.

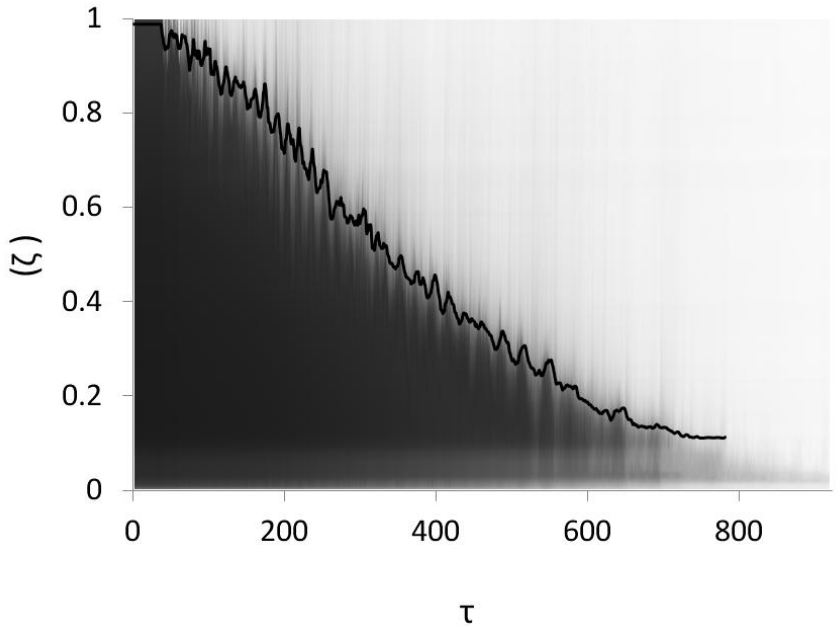

Figure 2.19: Gray scale image of the horizontal averaged buoyancy profile over time with the calculated interface height, ζ_i, superimposed as a black line ($Ri = 1.26$).

The interface height (ζ_i) and interface thickness (δ) were calculated at each time for each experiment. As described above, the lower Richardson number experiments exhibited a relatively uniform buoyancy profile. Although it was possible to calculate an interface height and thickness for low Richardson number experiments, due to small variations in buoyancy with height, the layer thickness was always relatively large, and the stratification could not be regarded as two-layered. As the Richardson number increased, the calculated interface thickness decreased.

The density profiles for all experiments were examined to determine their interface thickness and the predominant flow regime. The various flow regimes, described in the previous section, were determined by visual inspection of the time-varying buoyancy profiles. The well-mixed regime was denoted for buoyancy profiles where the vertical variation in buoyancy was small compared to the mean buoyancy in the cavity. The continuously stratified case was denoted when there was significant vertical variation but the peak gradient in the profile was not significantly larger than the mean gradient. As the Richardson number increased, the inflection in the profiles became sharper until, for large Richardson numbers, there was a distinct two-layer stratification in which the lower layer was well mixed (low buoyancy gradient below the interface). Between the continuously stratified and two-layer regimes was a transition region in which there was a sharp inflection, but the fluid below the interface still had a significant gradient and was, therefore, not well mixed.

To illustrate the transition between these flow regimes the largest recorded value for the interface thickness δ for each experiment was plotted against the Richardson number (see

Figure 2.20). The plot clearly demonstrates that, as the Richardson number increases, the interface sharpens.

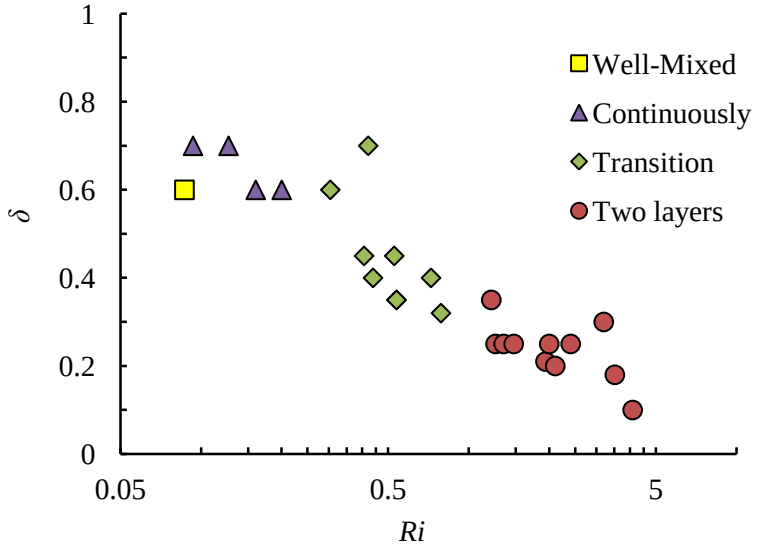

Figure 2.20: Maximum thickness of the density interface and the regime observed in the experiments as a function of the Richardson number.

2.3.3 Layer buoyancy decay

For experiments with high Richardson numbers, the buoyancy profile can be approximated by a two-layer stratification with a sharp interface separating the buoyant lower layer from the ambient upper layer. Once the interface height (ζ_i) was calculated, the layer buoyancy was taken to be the average buoyancy of all the fluid below the calculated interface, that is,

$$\gamma_l = \frac{\int_0^{\zeta_i} \gamma d\zeta}{\zeta_i} . \qquad (2.11)$$

A plot of the layer buoyancy over time is shown in Figure 2.21 for Ri=1.26. The Figure shows that the buoyancy of the lower layer decreases over time indicating that ambient fluid is being mixed down into the lower layer. Further, the buoyancy decay rate changes dramatically when the density interface gets close to the bottom of the cavity.

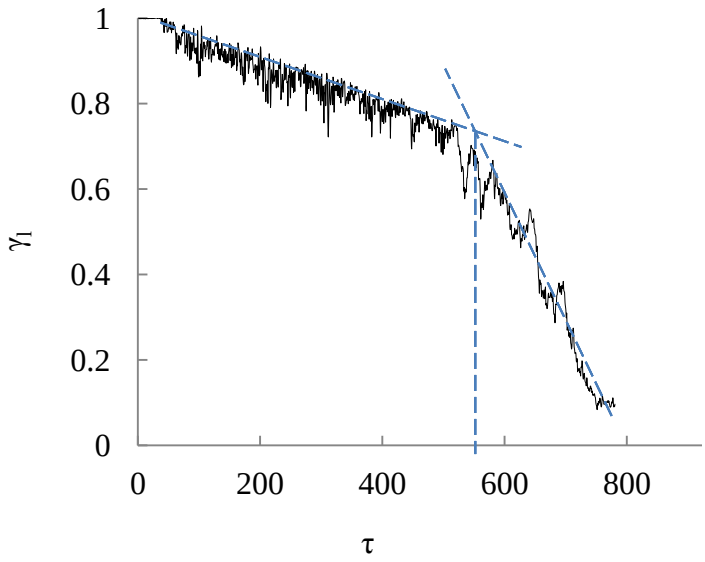

Figure 2.21: Plot of the layer buoyancy over the time for Ri=1.26. the vertical dashed line shows the time of buoyancy decay transition.

Defining a region of high shear between the top and the bottom layers (Figure 2.22), one possible explanation for this sharp transition is that the shear layer driving the mixing reaches the bottom of the cavity and so no source of buoyancy remains to entrain into the interface. Assuming the shear layer is symmetric about the interface height, it is possible to estimate the shear layer thickness, at the time when the buoyancy decay rate changes, as twice the height of the interface. That is

$$\delta_v = 2\zeta_i \tag{2.12}$$

at the time when the buoyancy decay rate increases. Interestingly, this calculated shear layer thickness was larger than the measured buoyancy interface thickness, defined in Figure 2.17, for all the experiments performed.

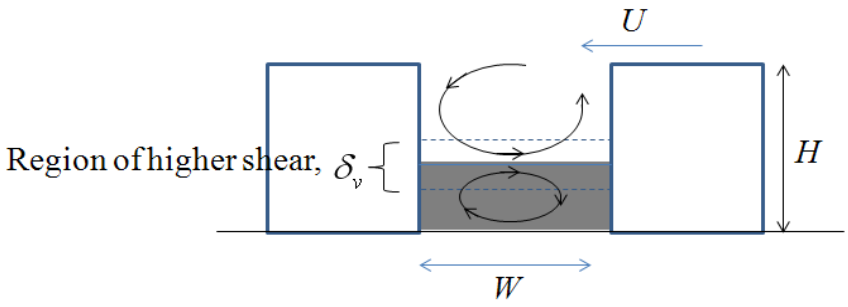

Figure 2.22: Schematic diagram of the high shear region symetric around the density interface.

The ratio of the shear layer thickness, δ_v, to the buoyancy interface thickness, δ_g, at the time of the buoyancy decay transition was calculated for each experiment and is plotted in Figure 2.23. Not only is the shear layer thicker, but the ratio of the thicknesses increases with increasing Richardson number. This is consistent with other experimental results for mixing in stratified shear flows which show that, for high enough Richardson numbers, the ratio of the shear layer thickness to the density step thickness increases with increasing Ri (Linden, 1979).

One point of difference between the results of this study and that of Debler and Armfield (1997) is that the measurements here indicate that, for the two-layer stratification case the density of the lower layer decreases over time. This indicates that the removal process is not simply a skimming process, but there is also an exchange flow across the interface in which ambient fluid is mixed down into the dense layer.

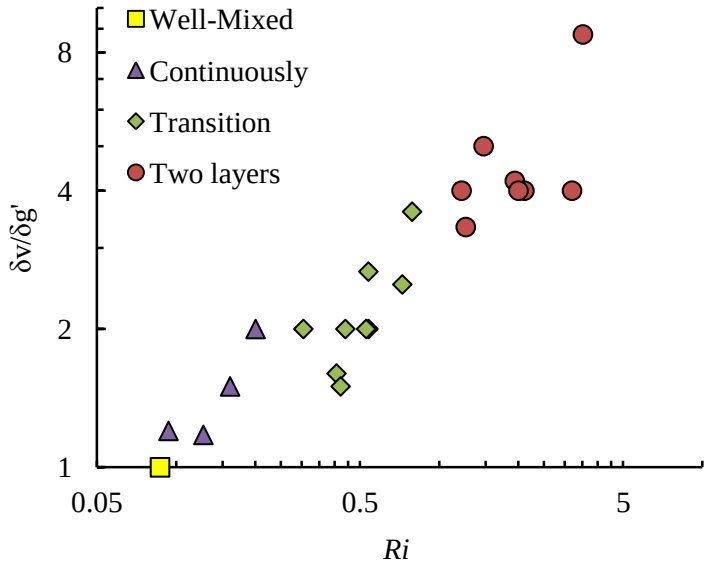

Figure 2.23: Thickness of shear layer divided by the thickness of the density interface as a function of the Richardson number at the time of the buoyancy decay transition.

2.4 Flushing parameterization

In order to quantify the rate at which buoyant fluid is removed from the canyon, the total buoyancy in the canyon was calculated at each time step and scaled on the initial total buoyancy contained within the canyon. The total scaled buoyancy at any time, Γ, is the total area under the vertical profile of the canyon (for example, in Figure 2.18) scaled on the area under the initial profile, that is

$$\Gamma = \int_0^1 \gamma d\zeta \tag{2.13}$$

This scaling is consistent with that used by Chang et al. (2007b) in their LES study of aspect ratio two canyons and Caton et al. (2003) in their experimental study of aspect ratio one cavities for $Ri = 0$.

2. 4.1 Exponential decay rate

Caton et al., (2003) indicates that the flushing of a finite volume of neutrally buoyant tracer from a canyon can be approximated by a first-order exchange process with a constant decay coefficient K, so:

$$\frac{C}{C_1} = e^{-Kt} \tag{2.14}$$

where C and C_1 are the spatially averaged concentration at any time, t, and t=0 respectively. K is the decay coefficient with units of 1/s. In the non-dimensional form the total concentration decay is

$$\Gamma = e^{-k\tau} \tag{2.15}$$

in which k is the non-dimensional decay rate coefficient, $k = KH/U$.

In order to quantify the effect of buoyancy on the flushing process, the total buoyancy decay profile was calculated for all 26 experiments using (2.13). Figure 2.24 and 2.25 show the examples of buoyancy effects on flushing profile, decay rate, and trapping time. The semi-log plots show the exponential decay as a straight line.

Decay curves in Figure 2.24 shows that for low Richardson numbers, the exponential function well represents the decay of buoyancy in the canyon. For the case of a dense fluid in the canyon, the decay rate was observed to be lower and to vary over time (see Chang et al., 2007b). The exponential decay rate increases over time since the buoyancy of the layer decreases during the purging process (Figure 2.24b). However, the initial 40-70% of the buoyancy decay rate for all experiments can be well approximated as constant (see Figure 2.25).

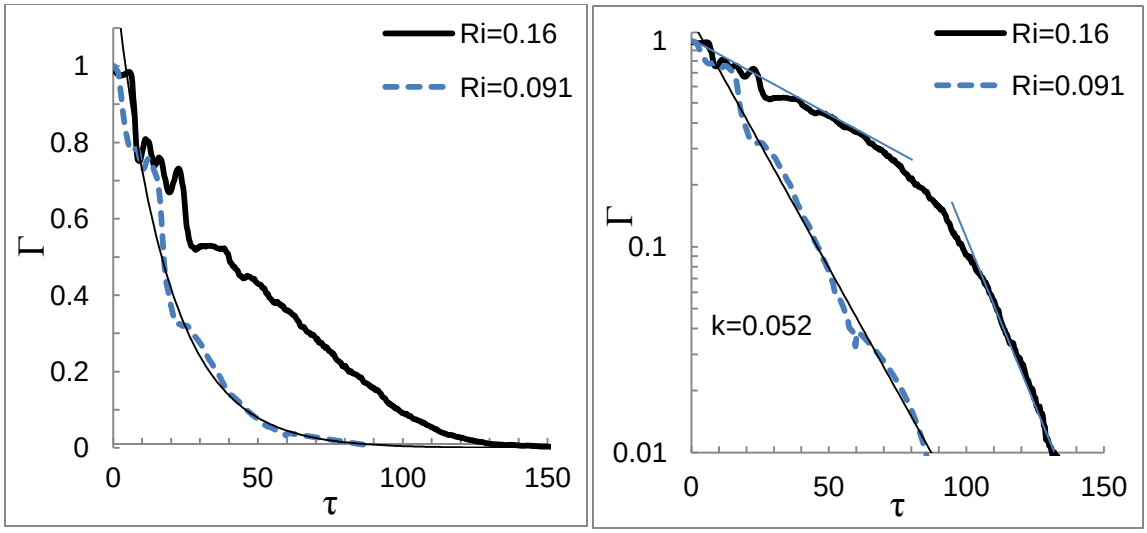

Figure 2.24: Buoyancy volume variation in the canyon for two tests with Ri=0.16 and 0.091 where (a) is a linear-linear scale plot and (b) a linear-log scale plot of the same data.

The constant initial decay rate (k) was calculated for each finite release experiment using data in the range of $1 > \Gamma > \Gamma_e$ where Γ_e is the maximum extent of the initial exponential decay. As an example, the dashed line in Figure 2.25 schematically illustrates how the exponential decay was fitted and Γ_e was obtained. The slope of the line is the exponential rate, k, for any given experiment.

The decay constant k was calculated for each Richardson number and results are plotted in Figure 2.26. It is reasonable to assume that for very low Richardson number flows ($Ri \approx 0$) the decay rate will be independent of Ri and will approach a constant. Further, the data suggest that the decay rate is a power law function of the Richardson number for higher Ri. It would therefore be possible to represent the data with an empirical equation of the form

$$k = \frac{1}{\left(a + bRi\right)^{c}} \tag{2.16}$$

A function of this form was fitted through the experimental data. The neutrally buoyant data point $k\left(Ri = 0\right) = 0.024$ from Caton et al. (2003) was shown in comparison with current data. A least squares fit gave the non-dimensional coefficients in (2.16) as $a = 18$, $b = 84$, and $c = 1.21$. The data for k vs Ri along with the curve fit are shown in Figure 2.26 showing that Eq.2.16 represents the data very well.

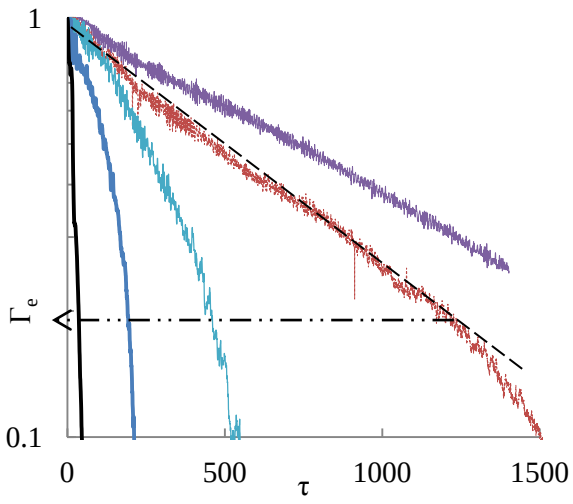

Figure 2.25: Buoyancy volume variation in the canyon for different Richardson numbers on a log- linear scale (from right to left, Ri= 4.1, 3.2, 1.26, 0.53, 0.091). Γ_e is the maximum extent of the initial exponential decay.

The exponential decay coefficients presented above are based on curve fits through data for the first stage of the flushing. It is expected that the exponential equation overestimates the time required to flush all the pollutant from the cavity for higher Richardson number flows as, in these cases, the actual decay rate was observed to increase over time (see Figure 2.25).

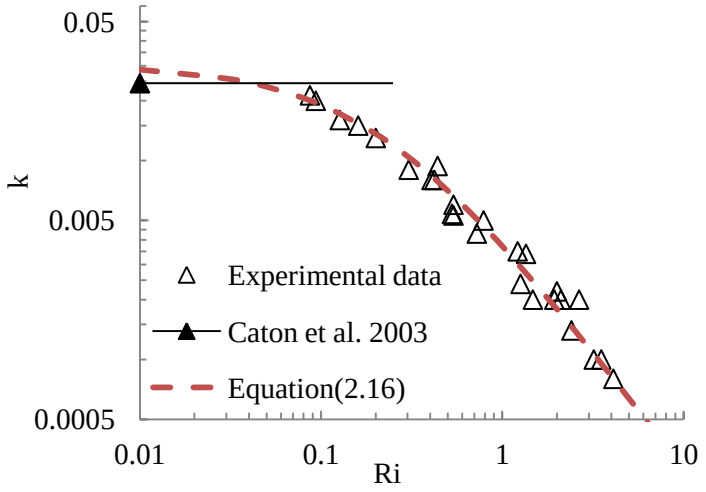

Figure 2.26: Decay rate coefficient for the initial 50% of the buoyancy removal. The horizontal line is k =0.024 found by Caton et al. (2003) for flushing a neutrally buoyant fluid. The dashed line shows the empirical equation (2.16) for k (Ri).

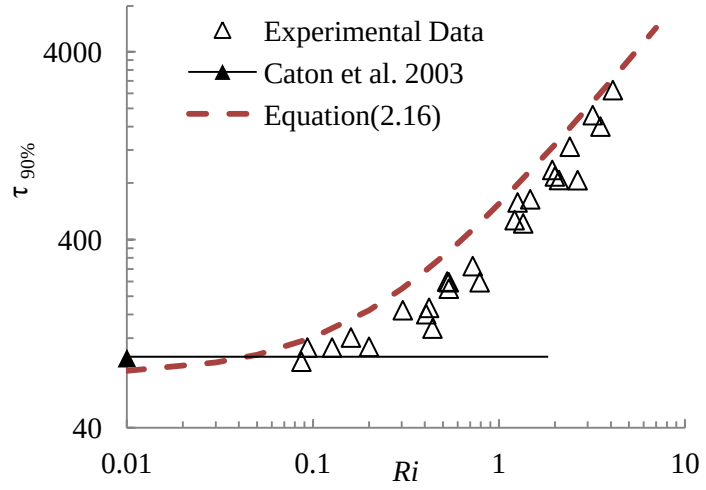

Figure 2.27: Non-dimensional time required to flush 90% of the buoyancy in the canyon, comparison of experimental and calculated data. The horizontal line is calculated from the results of Caton et al. (2003) for a neutrally buoyant fluid.

The effect of k value reduction is clear in Figure 2.27 which compares the measured time to flush 90% of the buoyant fluid with the time calculated, assuming that the buoyancy decays exponentially with a constant decay rate given by (2.16). As expected, the exponential decay model consistently over estimates the time taken to flush 90% of the pollutant.

2.5 Conclusion

A series of experiments were run to understand the mechanics of flushing a dense fluid from a cavity and to quantify the rate of flushing by a turbulent shear flow passing over the cavity top. Experiments were run for a broad range of Richardson numbers. The experiments were conducted in a water flume with using salt water as the dense fluid and fresh water for the ambient fluid. The density of the fluid in the cavity was measured continuously during the experiment using a light attenuation technique. The technique allowed mean vertical buoyancy profiles to be calculated at any time during the experiment.

When the flow first starts, the density interface at the top of the cavity is deflected down at the upstream end and up at the downstream end of the cavity. The deflection develops into a wave that travels across the top of the interface and generates a vortex that penetrates down the downstream cavity wall into the dense layer. The initial angle of deflection and vortex penetration depth are functions of the flow Richardson number. After this initial transient, a steady flushing flow is established. The buoyancy profiles exhibited three distinct flow regimes. For low Richardson numbers, the cavity remained well mixed and the buoyancy decayed exponentially over time. As the Richardson number increased, the cavity became stratified with the buoyancy increasing smoothly with height. For high Richardson numbers, a two-layer

stratification was observed in which a sharp density interface separated a well-mixed lower layer from the upper ambient layer. The thickness of the density interface decreased with increasing Richardson number (see Figure 2.20).

For the high Richardson number experiments, the density of the lower layer decreased linearly with time until the interface approached the cavity base. At this point the rate of decay of the layer buoyancy suddenly increased. The ratio of the distance of the interface from the cavity base to the interface thickness (defined in Figure 2.17) increased as the Richardson number increased (see Figure 2.23). This is consistent with the work of Linden (1979) who suggested that, for high Richardson number shear driven mixing in stratified flows, the ratio of the shear layer thickness to the buoyancy interface thickness should increase with an increasing Richardson number.

For the neutrally buoyant case the tracer concentration decays exponentially with time. This is also observed to be true for flushing the first half of a dense fluid. However, there are two major differences. First, the decay rate decreases with an increasing Richardson number as the density stratification suppresses vertical mixing (see Figure 2.25). Second, the decay rate increases over time as the stratification decreases, reducing its ability to prevent mixing (see Figure 2.24). The non-dimensional decay rate for flushing the first half of the pollutant was plotted against the Richardson number and shows that as the Richardson number increases, the decay rate is well represented by a power law function, whereas for low Ri, the decay rate approaches the neutrally buoyant value measured by Caton et al. (2003). The initial decay rate is well represented by an empirical expression given in (2.16). Measurements were also made for the time taken to flush 90% of the dense fluid form the cavity. The results show that using the

exponential decay rate from the first 50% will overestimate the time taken to flush 90%. This is due to the increase in decay rate over time as the stratification in the cavity becomes weaker.

Unlike in previous studies, present measurements indicate that the density of the layer decreases over time due to mixing across the interface and, therefore, flushing is due both to skimming of dense fluid off the top of the dense layer and to mixing across the interface.

CHAPTER THREE

EFFECT OF CANYON ASPECT RATIO

This chapter presents an experimental investigation of the effect of canyon aspect ratio on the flushing of a dense fluid from a canyon. Four series of experiments for different aspect ratios (η=0.45, 0.75, 1, 2) were conducted for a range of Richardson numbers. Not only did the flushing rate vary with both aspect ratio and Richardson number, but a range of flow regimes were observed exhibiting different flow kinematics. The qualitative and quantitative results for 64 experiments are discussed and compared.

3.1 Introduction

Pollutant mixing and transfer is dependent on the flow structure within the urban canyon. The influence of canyon aspect ratio, η, on the kinematics of urban canyon flow has been studied extensively. Three basic flow phenomena have been identified (Oke, 1988, Xie et al., 2007; Soulhac et al., 2008): Isolated roughness flow (η> 6.67) in which the atmospheric boundary layer (ABL) fully re-attaches between buildings, wake interference flow ($1.54 < \eta < 6.67$) in which the ABL does not fully re-attach and downwind buildings feel the effect of the wake behind any upstream buildings, and skimming flow (η <1.54) in which the ABL skims over the top of buildings and flow between buildings is driven by shear at the top the canyon formed by the buildings. The majority of studies on urban canyon flow are based on these categories to describe the kinematics in canyon.

The presence of recirculating cells and the number of vortices in the canyon can affect the pollution dispersion (Li et al. 2007). In a study by Simoens et al. (2007) the extent of the recirculation zone formed between the buildings was examined as a function of η. They showed that, for $1 < \eta < 6$ the cavity flow is dominated by a single vortex. A small secondary vortex develops at street level next to the upstream building for $\eta > 2$. For $\eta > 6$, a secondary vortex forms at the downwind end of the canyon and the flow fully reattaches to the street level for $\eta > 8$. Aspect ratios less than one were not considered in that study.

Baik et al. (2000) used a water flume to study the flow structure in canyons with different building heights and canyon aspect ratios of 0.33, 0.42, 0.5, 0.66, 1.They reported one vortex for η>0.5 and two counter rotating vortices for η<0.5. Sini et al. (1996) found that if the street is not symmetrical, or if it is narrow (η<0.66), then two counter-rotating cells may form (Soulhac et al., 2008). Cheng et al. (2008) modeled street canyon ventilation and pollutant removal, through a computational and analytical study. They considered aspect ratios 0.5, 1 and 2. It was found that the flushing time for a pollutant was a maximum for an aspect ratio of η =0.5 indicating that a longer time was required to flush a pollutant from the narrowest canyon investigated. Generally, the wider the canyon, the more rapidly a pollutant is flushed out as the ambient flow more easily penetrates down into the canyon (Park et al., 2004). Liu et al. (2005) also shows that for aspect ratio 2 the concentration is 67% lower than aspect ratio one and 0.5.

A study by Chang and Meroney (2003), for 3D urban street canyons, also showed that there are three flow regimes (skimming, wake interference and isolated roughness flow). It was reported that for the wake-interference regime, the higher pollutant concentration occurs on the upwind end of the canyon since the pressure is low and tends to draw pollutant into the cavity zone close to the upwind wall.

Pollution dispersion studies that considered canyon aspect ratio have focused almost exclusively on neutrally buoyant pollutants (Soulhac et al., 2008; Simoens et al., 2007; Park et al., 2004; Chang and Meroney, 2003; Liu et al., 2005; Cheng et al., 2008). There are some studies looking at thermal buoyancy effect in the canyon with different aspect ratios (Kim and Baik 2001; Xie et al., 2007; Cheng et al., 2009; Liu et al., 2003; Li et al., 2005). The buoyancy of the pollutant or thermal changes can affect the flow structure and the strength of the vortices in the canyon. It was shown that for some cases the thermal buoyancy can change the flow regime (defined based on Oke 1998) from one to another. As an example, heating the windward wall of the canyon causes multiple vortices in the canyon rather than one single stable vortex. This flow change can result in a reduction in the flushing rate since the pollutant is trapped longer in the recirculating flows (Sini et al., 1996). Thermal buoyancy also affects the pollution transport from the canyon. Unstable atmospheric conditions increase the rate of pollutant flushing due to a higher level of vertical mixing. Kim and Baik (2005) showed that heating the bottom of the canyon can strengthen the vortex so the rate of pollutant mixing is increased.

Besides thermal buoyancy, a dense pollutant has the potential to significantly alter the flow kinematics in different aspect ratio canyons, and requires detailed investigation. Debler and Armfield (1997) considered different aspect ratios ($1<\eta<16.7$) for rectangular and trapezoidal cavity geometries over a range of Richardson numbers ($0.45 < Ri < 31$). Another study on purging dense fluid from a wide trapezoidal cavities ($\eta>5$) under shallow water was undertaken experimentally, numerically, and analytically by Kirkpatrick et al., (2012). They examined shallow flow over a wide trapezoidal cavity. The in-cavity flow structure was different than the flow observed for canyons with vertical walls. The in-cavity vortex structure and the skimming process were mainly due to the separated shear layer above the cavity. Debler and Armfield

(1997) showed that for very wide trapezoidal cavities, there is no flow separation at the leading edge.

They also demonstrated that in addition to the canyon aspect ratio and the buoyancy, the canyon geometry and number of upstream canyons (or cavities) significantly affect the pollutant removal rate. It was shown that, compared to the single cavity, the multi-upstream cavity case increases the pollutant exchange rate due to the generation of turbulence upstream. However, Chang and Meroney (2003) demonstrated that, compared to a single canyon geometry, the upstream buildings have a sheltering effect for pollution transport. Because there is no flow separation at the leading edge of the isolated canyon generating extra turbulence and vortices (Figure 1.2).

In this study, assuming an open country street canyon, all aspect ratio models are used as single canyons. The flushing of dense fluid is considered for 4 different aspect ratios (Eq. 1.1) $\eta = 2, 1, 0.75, 0.45$. Experiments were run for a broad range of Richardson numbers ($0.09 < Ri < 4$) for each aspect ratio. The remainder of the chapter is structured as follows. The experimental technique and procedure is described in section 3.2. Experimental results investigating the effect of aspect ratio are presented in section 3.3. Transition in behavior from the initial purging to the later mixing is discussed in section 3.4, the comparison of existing data with this study results is presented in section 3.5 and conclusions are drawn in section 3.6.

3.2 Experimental procedure

A series of experiments were conducted to examine the effect of aspect ratio on the time taken to flush a finite volume of dense fluid from a model canyon. These experiments employed the same set-up and procedure explained in the past chapter for a total of 64

experiments. Two parallel square prisms with a height and width of 10 cm, separated from each other by 4.5, 7.5, 10 and 20 cm, formed the cavities of aspect ratios $\eta = 0.45,0.75,1,2$ respectively.

The surface roughness morphology for this series of experiments was kept the same as that employed for the experiments for aspect ratio η=1 presented in the previous chapter (a level gravel bed of d_{84}=1.14 cm). Analysis of the boundary layer produced by the aggregate bed led to an estimate of the surface roughness height of z_0=0.24 cm, a Jensen number of Je=42, and a prism top upstream turbulence intensity of $I = 0.15 \pm 0.02$.

3.3 Flow characteristics

The general purging process observed was similar to that reported in the previous chapter for a canyon with aspect ratio one and by Armfield and Debler (1993). A fast initial stage of purging occurred after abruptly initiating the flow. The interface was deflected and a slug of dense fluid was ejected out of the canyon (first row in Figure 3.1). The maximum vertical deflection of the interface, d/H, during the initial purging is plotted as a function of the Richardson number in Figure 3.2. It is shown that changing η affects the deflection depth but looking at the Figure 3.3 Indicates that only wide canyon (η=2) has influence on the initial slop of the interface surface. At a later stage a vortex formed over the interface surface due to the upstream flow separation and gradually moved into the canyon removing the dense fluid (5^{th} row in Figure 3.1). Observations indicate that at high aspect ratios (e.g. η=2 in this study) the shear flow and initial vortex penetrate more deeply into the canyon compared to η=1. For narrower canyons, the external flow skims the canyon mouth without penetrating vertically

down so the initial deflection decreases compared to higher aspect ratios. Further, the initial splash of dense fluid at this first stage is considerably lower for lower aspect ratios canyons.

In Figure 3.1 for all aspect ratios the steady vortex near the downstream wall and consequently higher leeward side concentration are discernable at the later stages. The initial purging process is qualitatively the same for all Richardson numbers and aspect ratios. However, after the initial purge, the different flow regimes (well-mixed, continuously stratified, or two-layer) were observed, depending on the canyon aspect ratio and the Richardson number.

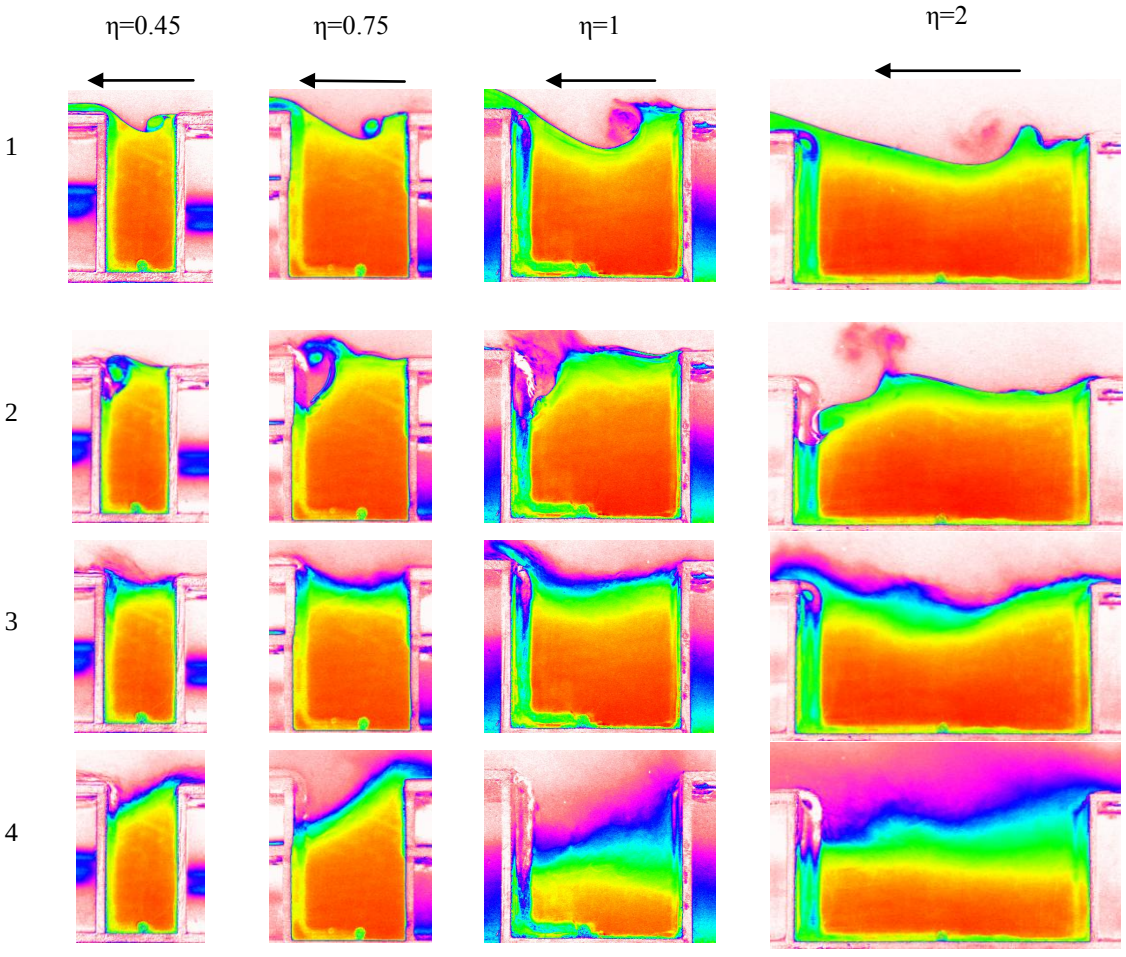

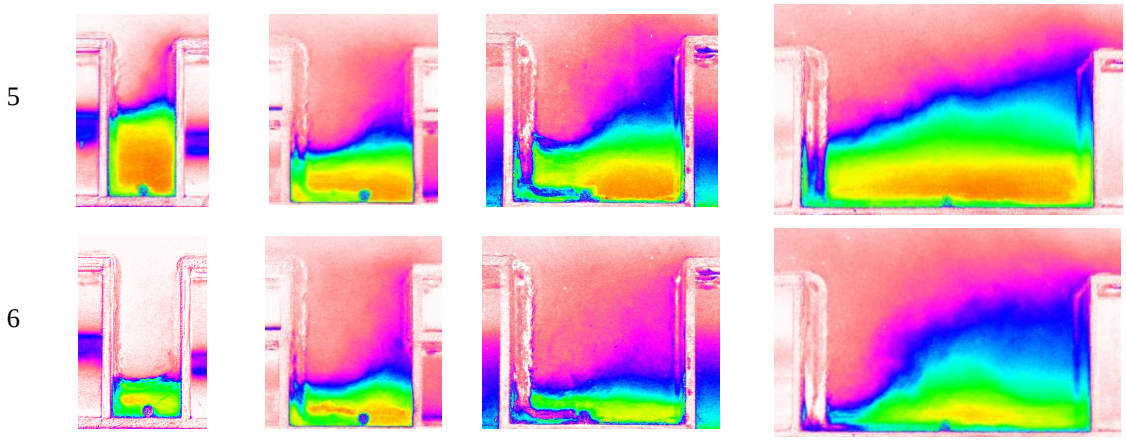

Figure 3.1: False color images of the flushing of canyons of different aspect ratio for Ri≈0.4. First row shows the initial deflection and flow penetration into the dense layer for different aspect ratios. The times for each image are: η=0.45, tU/H =3.5, 6, 13, 16, 158, 657; η=0.75, tU/H=4, 7, 15, 20, 85, 180 η =1, tU/H =5, 7, 14.5, 78, 103.5, 145; η =2, tU/H = 12.5, 16, 24, 50, 106, 143.

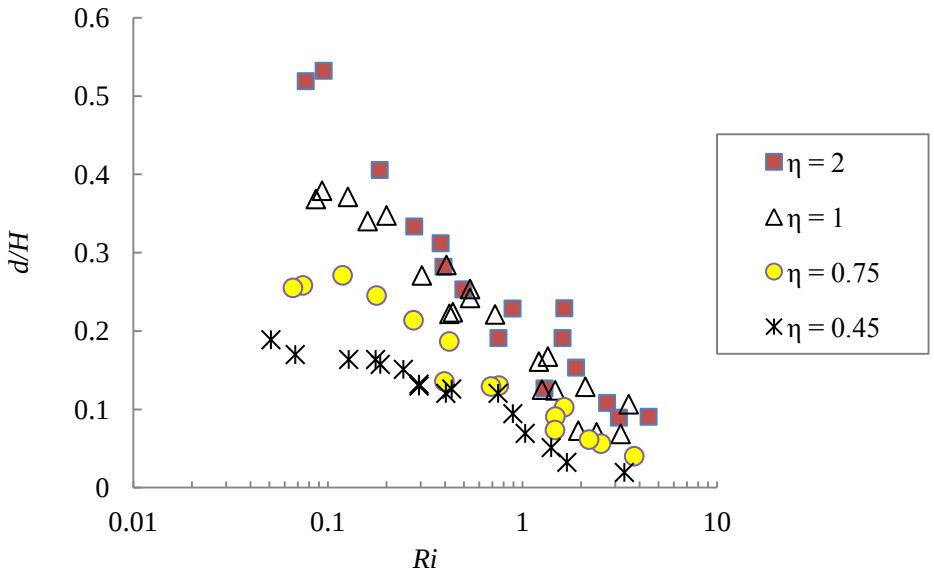

Figure 3.2: relative deflection observed for each aspect ratio, as a function of the Richardson number.

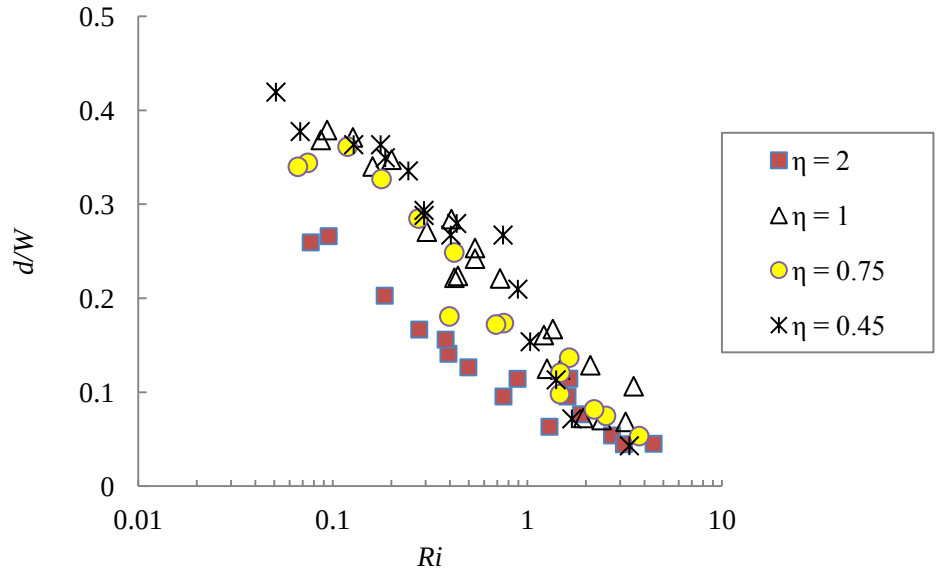

Figure 3.3: Initial slope of interface surface observed for each aspect ratio, as a function of the Ri number.

In the previous chapter the effect of buoyancy on the flow regime was explained in detail. For very low Richardson number the vortex inside the canyon is strong enough to fully penetrate the fresh water into the dense layer. The vortex can overturn the dense fluid and occupy the whole canyon. This results in a well-mixed canyon with exponential concentration decay throughout the flushing process. For higher Richardson numbers, turbulent mixing and the large vortex creates an interfacial layer between the bottom dense and top fresh layer. The density stratification in this interface varies continuously over the depth of the canyon. Depending on the thickness of this interface, δ, the regime inside the canyon changes from continuously stratified (high δ value) to a two-layer flow (low δ value).

The canyon aspect ratio influences the flow regime as well. As shown in Figure 3.1 a smaller aspect ratio cavity, that is tall and narrow cavity, maintained a stronger stratification at lower Richardson number compared to wider cavities. This is because the initial vortex does not

penetrate as deeply into narrower cavities compared to those with larger aspect ratios. Increasing the aspect ratio is qualitatively analogous to decreasing the Richardson number. As η increases, the initial penetration depth increases and the interface becomes more diffuse and thicker. Figure 3.4 shows the maximum interface thickness δ (based on the definition shown in Figure 2.17) observed during each experiment. As explained in chapter two increasing the Richardson number decreases the thickness of the interface layer. The peak density interface thickness is also strongly influenced by the canyon aspect ratio. For example, for a Richardson number of Ri=0.5, the interface thickness was measured to range from δ=0.2 for η=0.45 up to δ=1.0 for η=2. Narrower canyons (lower aspect ratio) produce thinner density interfaces and hence more stable stratifications.

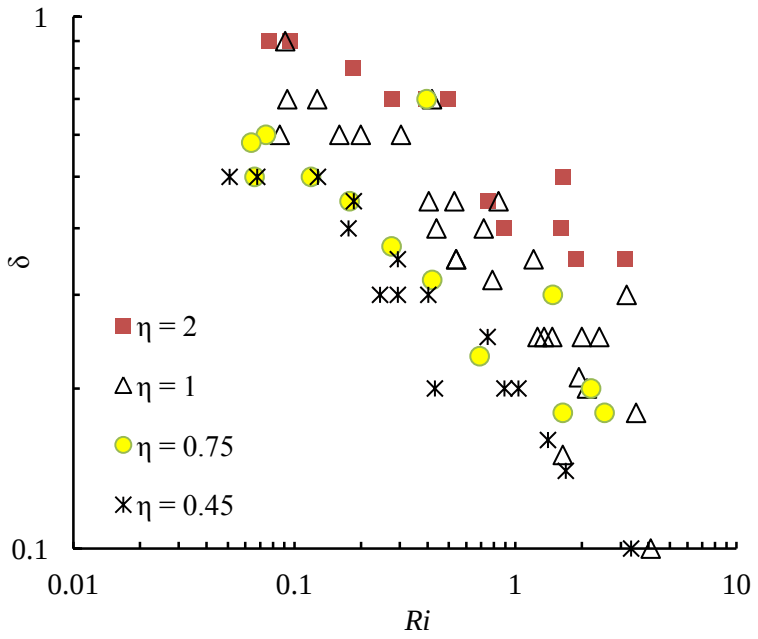

Figure 3.4: Maximum thickness of the density interface, observed for each aspect ratio, as a function of the Richardson number.

Generally when the vortex cannot penetrate into the dense layer (due to either high Richardson number or narrow width of the canyon) the purging phenomena is mainly performed by scouring the salt water from the interface surface. In this regime the interface is thin (δ is small) and a two-layer stratification is observed. For lower Richardson numbers or wider canyons, the interfacial mixing increases, the interface is considerably thicker and the density stratification is less stable.

Figure 3.5 shows example profiles of different regimes in different aspect ratios when the Richardson number is constant. Vertical buoyancy profiles at different times and the canyon concentration contours half way through the flushing process are shown together.

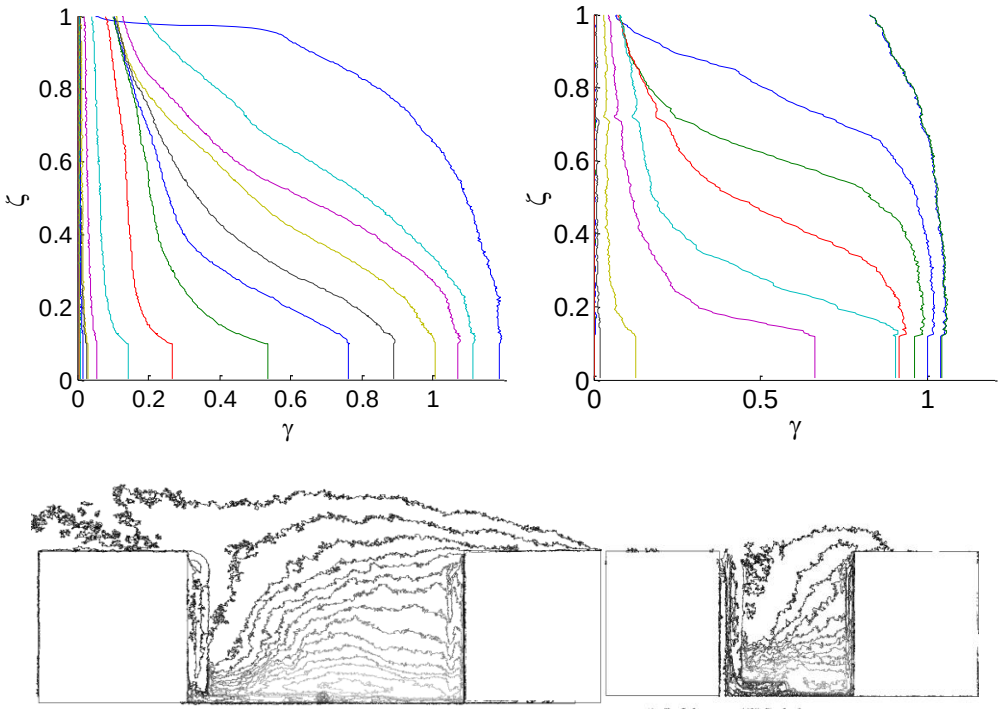

(a) η=2 (b) η=1

Figure 3.5: figure continues in next page

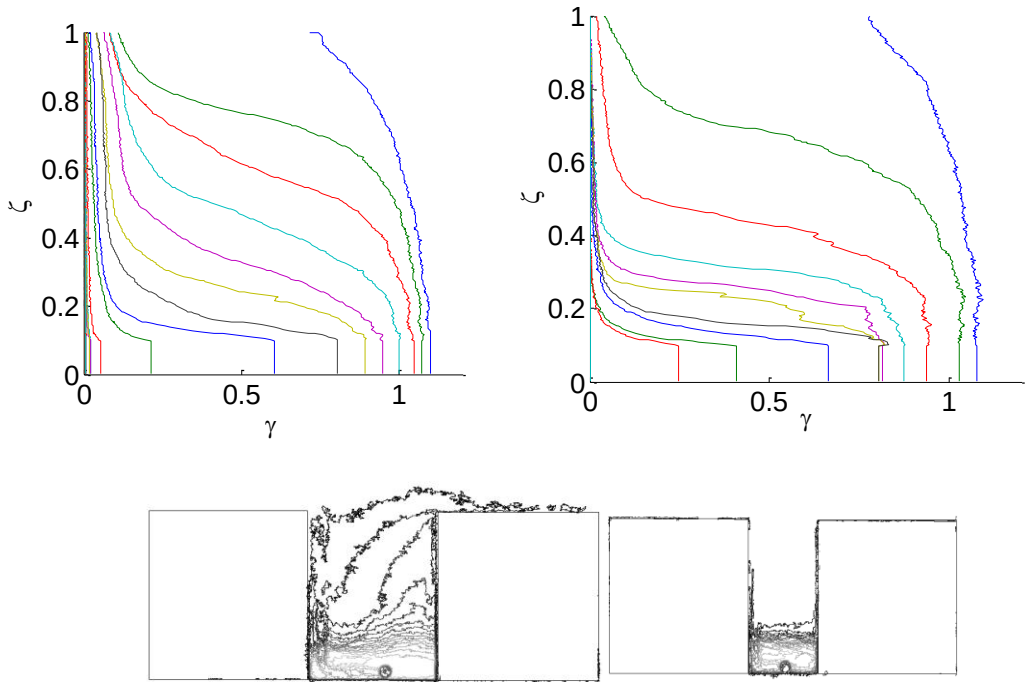

(c) η=0.75 (d) η=0.45

Figure 3.5: Contour plot images of the canyon concentration of different aspect ratio for Ri≈0.4 at 1/2 total time of flushing, along with the buoyancy profile at the equal time intervals during the test. a) continuously stratified flow, b&c) transition flow , d) two-layer stratification.

A clear difference between Figure 3.5 and results from cavity geometry studies is that dense fluid is drawn upstream on top of the upstream building due to the flow separation at that buildings leading edge. This is not observed in studies of cavities where there is no upstream flow separation. However, just as in neutral pollutant studies (e.g. Cheng et al., 2008), the pollutant concentration at the leeward side of the canyon is higher than the windward side because of the stationary vortex at the windward end of the canyon pushing dense polluted fluid toward the leeward wall (Figure 3.5).

The dominant flow regime that followed the initial purge was established for each experiment based on analysis of the vertical buoyancy profiles measured over the course of the test. The regimes are denoted as well-mixed (later stages of Figure 3.5a) when there is no significant vertical variation in buoyancy with height; continuously stratified when there is significant vertical variation in buoyancy, but the peak buoyancy gradient is similar to the mean buoyancy gradient (Figure 3.5a); and two-layered in which there is a clear two-layer stratification with a well-mixed lower layer and a sharp interface between the layers (Figures 3.5d). A transition regime is also included in which there is a region of relatively high buoyancy gradient, but there is no well-mixed lower layer (Figure 3.5b, c).

A regime diagram showing the observed flow regimes in Richardson number, aspect ratio space is shown in Figure 3.6.

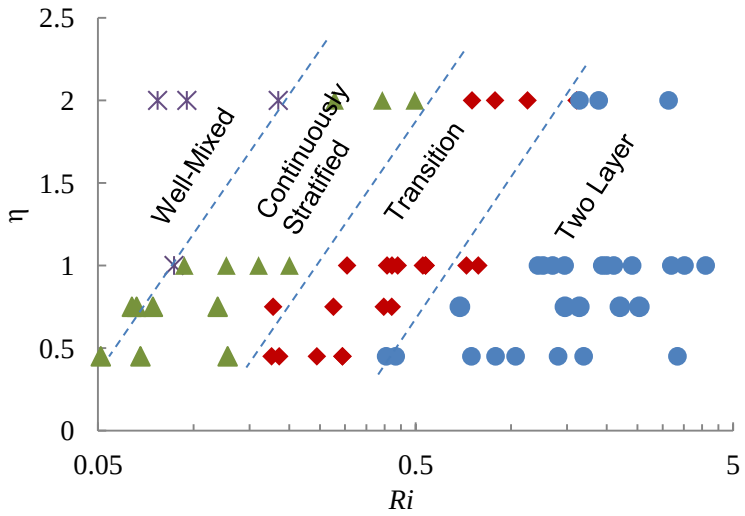

Figure 3.6: The flow regime observed as a function of the Richardson number and aspect ratio. Stars represent well-mixed flow; triangles, the continuously stratified flow; diamonds, transition state and circles represent two-layer stratified flow.

Each regime is shown with a different symbol. Approximate regime boundaries are also shown. As observed above, the higher the Richardson number and lower the aspect ratio the more stable the stratification.

For higher Richardson numbers the dense layer can significantly alter the flow kinematics. As noted above, the flow kinematics for a neutrally buoyant fluid depends on the aspect ratio. For high Richardson number flows, the dense lower layer inhibits vertical mixing and acts as a (soft) canyon base. Therefore, the flow kinematics is controlled by the effective canyon aspect ratio which is the width of the canyon divided by the vertical distance from the top of the canyon the density interface at the top of the dense lower layer. As the lower layer is eroded the effective aspect ratio changes resulting in different flow kinematics. For example, for very high Richardson numbers and wider canyons, no vortex can form within the canyon and the initial flushing is due to flow splashing from the up- and down-stream corners (Figure 3.7a). However, as the interface gets lower the aspect ratio decreases and a scouring vortex is established in the canyon (Figure 3.7b).

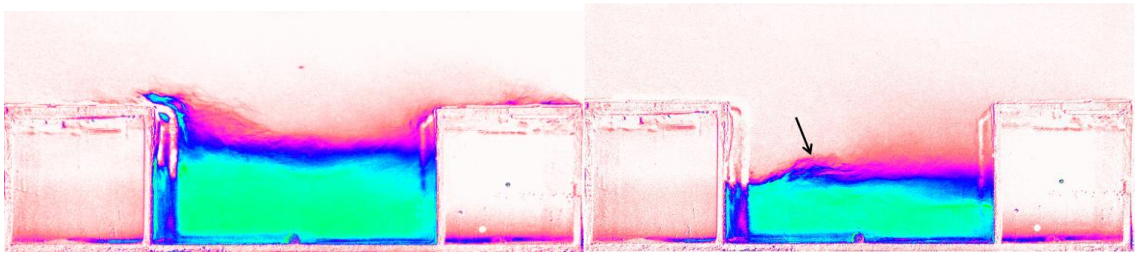

(a) (b)

Figure 3.7: Examples showing the removal mechanism at η =2 before and after vortex formation. The arrow in (b) shows the patches due to scouring vortex at the top of the layer.

Figure 3.8 shows the effective aspect ratio once the vortex has formed as a function of the Richardson number. For high Richardson numbers, the vortex forms at the same aspect ratio (η≈ 4.5) for all models. For lower Richardson number, a steady vortex formed in the canyon at the beginning of the experiment.

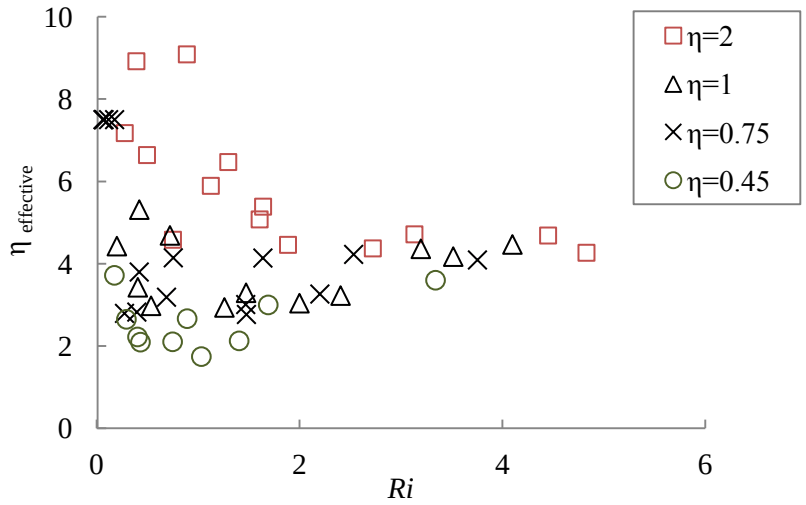

Figure 3.8: the interface height at the time of formation of the steady vortex at the downstream end of the canyon with η=0.45, 0.75,1,2.

3.4 Flushing rate and trapping time:

As was shown, canyon aspect ratio is an important parameter affecting the regime of the flow, buoyancy stratification and the vortex formation in the canyon. With the changes in flow structure, the rate of the pollution dispersion from the canyon varies. For example in a narrow canyon it is expected that the lateral restriction on the vortex reduces the pollutant removal rate as the rotating flow inside the canyon is not able to grow vertically (due to the width limitation) and reach deep into the canyon. To quantify the effect of aspect ratio on the buoyancy flushing process, the total buoyancy decay profile was examined for all 64

experiments. Figure 3.9 compares of the effects of the buoyancy (Figure 3.9a) with the effects of the aspect ratio (Figure 3.9b) on the flushing rate. The slop of the straight line shows the exponential decay, k.

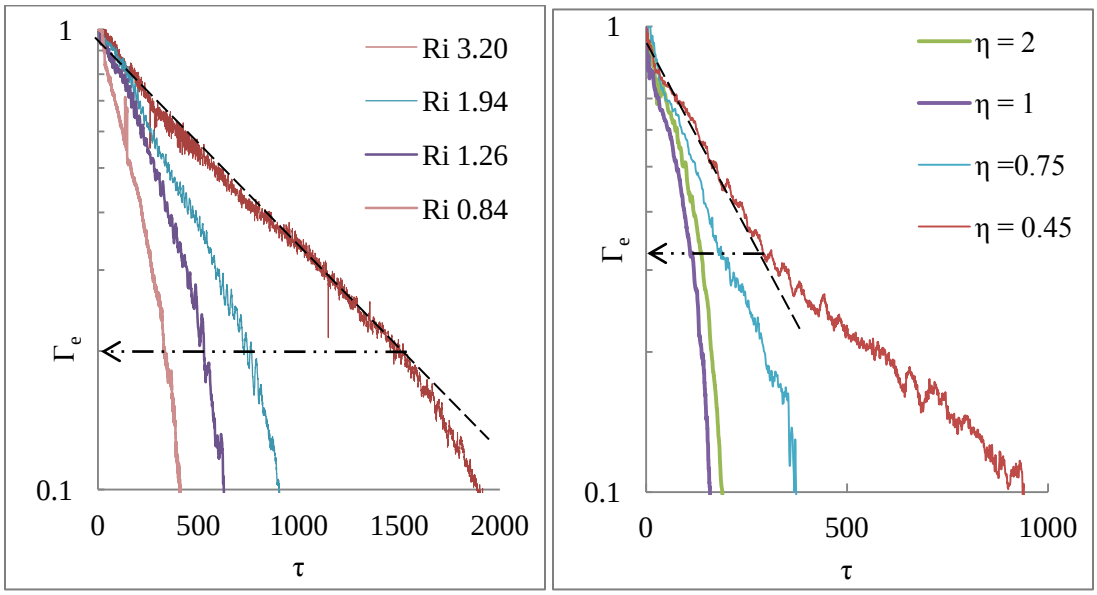

Figure 3.9: Buoyancy decay comparison for a) different Richardson numbers with aspect ratio=1, b) different aspect rations and Ri≈0.4.

For both sets of data shown in Figure 3.9a&b, the first phase of flushing decay (ignoring the initial splash and interfacial waves that cause an initial flushing at a slightly higher rate) is observed to be exponential. Exponential decay curves of the form given by (2.15) were fitted through $1 > \Gamma > \Gamma_e$, the range in which decay rate is exponential, and the decay constant k was calculated. The value of Γ_e changes, depending on the aspect ratio and Richardson number of the flow. The variation of Γ_e versus Ri number for different aspect ratios is discussed in detail in the next section. The decay constant k was calculated for each Richardson number and aspect

ratio tested. Results are plotted versus Richardson number in Figure 3.10 for different aspect ratios.

As expected from the previous chapter, for a constant η, the rate of flushing increases as Ri decreases and the stratification in the canyon becomes less stable. Comparing the results for all aspect ratios shows that, with the exception of η=0.45, the initial exponential decay rate varies only slightly with η. Since the maximum rate of flushing is expected to be observed for a neutrally buoyant pollutant, k values calculated from Caton et al.(2003) were used as a point of comparison. The upper limit for η=1. Caton's experimental data is relatively close to this study result for η=1 (though it should be noted that Caton et al., 2003 used a cavity rather that canyon geometry). Following the same arguments for equation (2.16), an empirical equation for k was found for each aspect ratio. The coefficients are presented in table 3.1. Figure 3.10 contains trend lines for η=1 & 0.45.

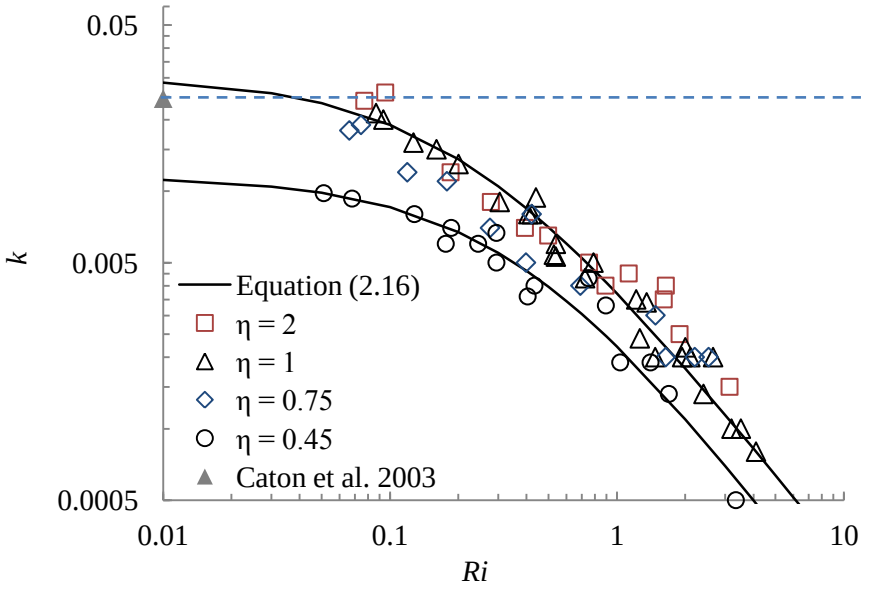

Figure 3.10: The exponential decay rate coefficients for all aspect ratios. Dashed line shows the k upper limit based on Caton et al., (2003), η=1. Solid lines show Eq. 2.16 for different aspect ratios η=0.45 &1.

Table 3.1: Curve fitting coefficients in Eq. 2.16 ($k = \frac{1}{\left(a + bRi\right)^c}$) for different aspect ratios.

η	a	b	c	R^2
1	18	84	1.21	0.98
2	16.5	91.6	1.19	0.93
0.75	21	109	1.2	0.95
0.45	31	79	1.3	0.94

Figure 3.10 only quantifies the rate of flushing in the first part of the experiment. To examine the later stages of the flushing process, the time taken to flush 90% of the initial buoyancy, $\tau_{90\%}$, was measured. The resulting times are plotted in Figure 3.11 as a function of Richardson number for each aspect ratio. As is expected from chapter two, the trapping time increases with Richardson number for each aspect ratio. Based on the initial decay rate data (Figure 3.10), the aspect ratio one and two canyons showed similar results. The trapping time for η=0.75 is slightly higher than that for aspect ratio one, while for η=0.45, a dramatic change in $\tau_{90\%}$ was observed (Figure 3.11). The increasing trapping time with decreasing aspect ratio is consistent with the case of flushing neutral pollutant tested by Cheng et al., (2008) who showed that when η=0.5 the air quality is the worse than for η=1&2 because of slower pollutant flushing. Following the same reasoning to establish the form of (2.16) the data should be well described by a function of the form

$$\tau_{90\%} = \left(a + bRi\right)^c . \qquad (3.1)$$

Table 3.2 shows the coefficients of the best fitted curves in form of (3.1). The results for η=1 & 0.45 are shown in the graph.

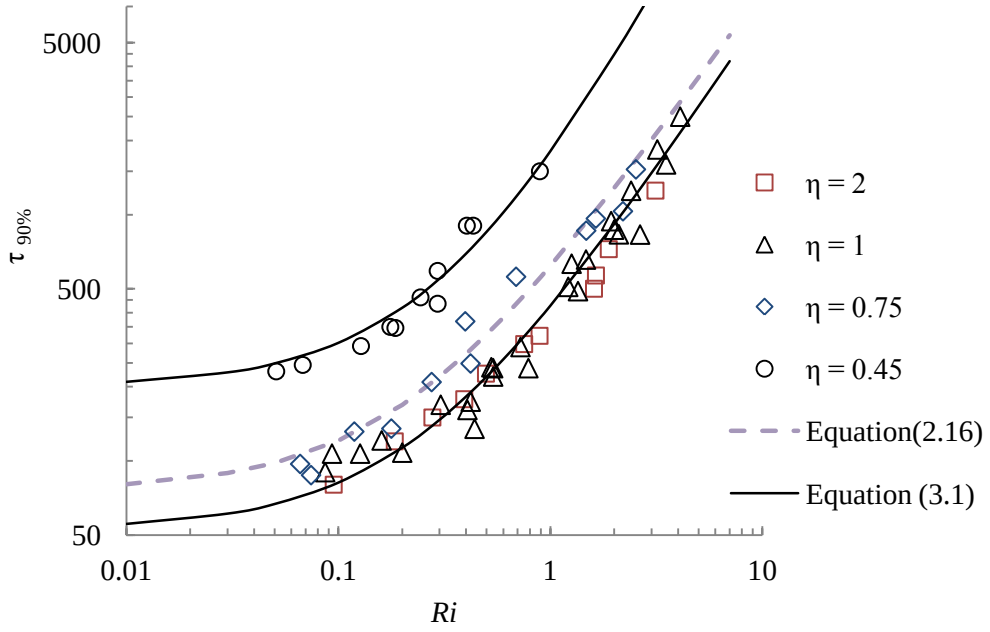

Figure 3. 11: The time of flushing 90% of the canyon buoyancy for all aspect ratios. Solid lines are examples of Eq.3.1 for η=1 &0.45. Dashed line compare the extrapolated $\tau_{90\%}$ from Eq.(2.16) for η=1.

Table 3.2: Curve fitting coefficients in Eq. 3.1 for different aspect ratios.

η	a	b	c	R^2
1	22.5	84	1.3	0.95
2	27	84	1.25	0.99
0.75	23	86.5	1.35	0.93
0.45	25.8	74	1.63	0.94

The analytical work of Caton et al. (2003) implies that, for an external flow with low turbulence, the decay rate, k is

$$k = A_1 \tag{3.2}$$

where A_1 is a non-dimensional parameter dependent on the shear layer turbulence intensity, I, and for high inflow turbulence, the decay rate is

$$k = A_2(I)^{1/2}\left(\frac{l}{W}\right)^{1/2} \tag{3.3}$$

where l is the turbulence length scale of the external flow and A_2 is a constant. Therefore, flushing times based on Caton's equation are expected to be independent of canyon aspect ratio in case of low external turbulent flow. For high turbulent flow the time of flushing should decrease for narrower canyons based on (3.3). This is not observed in the experiments for dense fluid flushing presented here. As the aspect ratio decreases (W decreases), the decay constant decreases and the total flushing time increases.

3.5 Flushing mechanisms

The above sections have focused on qualifying the flow regimes observed and quantifying the flushing rate for different aspect ratios over a range of Richardson numbers. This section presents a detailed discussion of the various mixing mechanisms that were observed and that can be inferred from the flushing data. As shown above for all experiments, the initial decay in total buoyancy is exponential. After this initial exponential phase, the flushing rate, k, varies. The time and nature of this change depends on the canyon aspect ratio.

For low Richardson numbers the dense fluid in the canyon rapidly gets mixed, reducing the mean buoyancy in the canyon and, therefore, reducing the instantaneous Richardson

number based on the total canyon height. This in turn results in the exponential flushing rate (k) increasing (e.g. Figure 3.9a). However, for larger Richardson numbers a stable stratification develops in which there is a clearly distinct dense lower layer. Over time this layer is thinned and the buoyancy of the layer decreases. As the buoyancy interface moves further away from the top of the canyon more work is required to raise the dense fluid up into the ambient flow above. Therefore, there are two competing changes that influence the flushing rate, the reduction in mean buoyancy and the increase in height over which dense fluid must be lifted in order to flush it. If the rate of reduction of the layer buoyancy (mixing into the layer) is rapid enough then the mean flow is able to continue flushing the diluted fluid at a relatively constant exponential rate (later profile in Figure 3.9a). However, for a two-layer stratification, if the mixing across the interface is significantly suppressed by for example a narrow canyon or high Richardson number, then a point is reached at which the flushing rate, k, must decrease. This can be seen most clearly in Figure 3.9b for the narrowest canyon, $\eta = 0.45$, and in Figure 3.12a&b as the Richardson number increases.

Figures 3.12 a&b show the flushing decay changing due to increasing Ri number for η=0.75 and 0.45 respectively. Comparing these two graphs with the decay profiles for canyon aspect ratio in Figure 3.9a clearly demonstrate the aspect ratio influence on flushing rate. In Figure 3.9a for the canyon with aspect ratio one, the range of exponential decay ($1 - \Gamma_e$) increases with increasing Ri number. However for narrow canyons the side walls inhibit the vertical penetration of the vortex which reduces the mixing at the interface and hence flushing rate, k (Figure 3.12). Figure 3.13 compares the fraction of the initial buoyancy flushed during the exponential decay for the different aspect ratio experiments. The fraction of total buoyancy flushed during the initial purge ($1 - \Gamma_e$) for the tall and narrow canyon with η=0.45 is different

from those of the other aspect ratios (Figure 3.13). A more detailed discussion of the initial exponential decay and transition is presented in the following chapter.

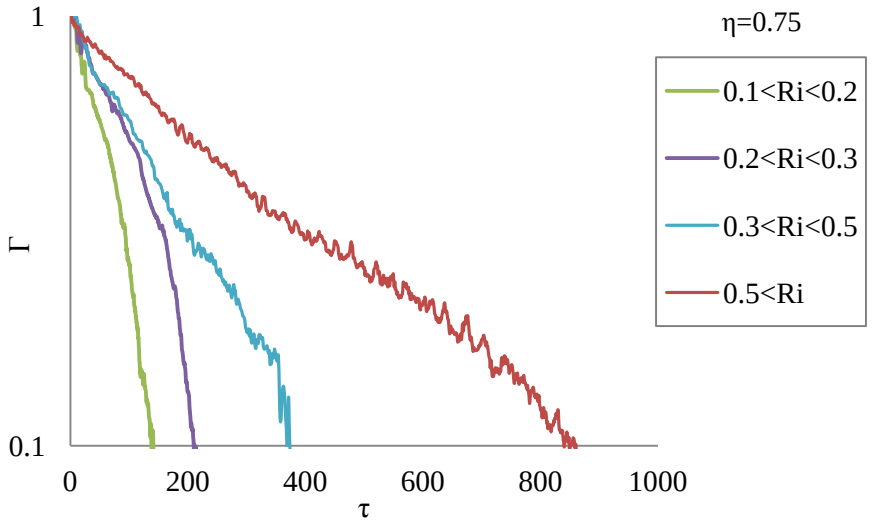

(a)

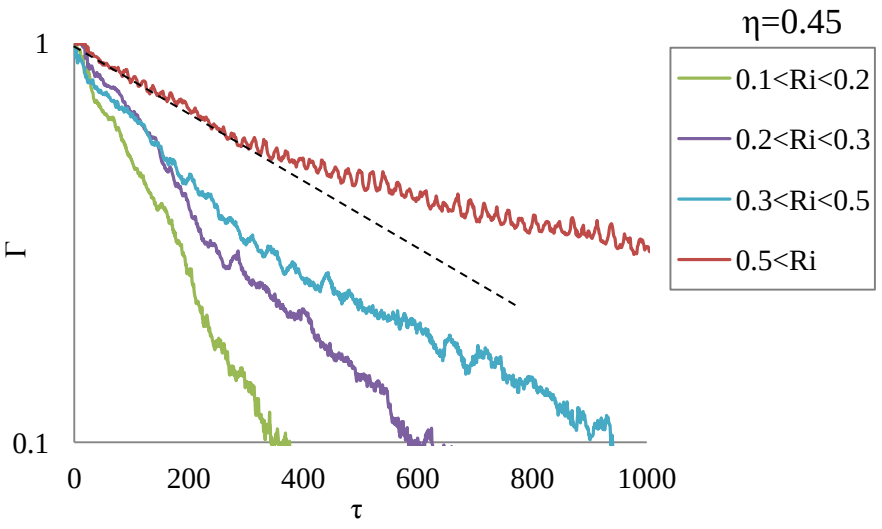

(b)

Figure 3.12: Flushing decay profiles for a) η=0.45 and b) η=0.75. Dashed line slope illustrate the initial decay rate.

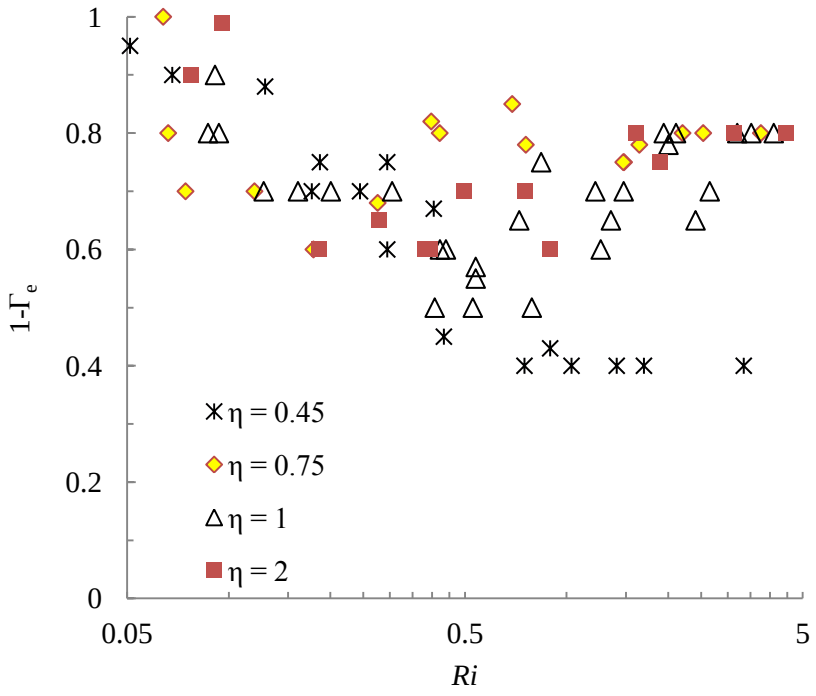

Figure 3.13: Fraction of the total buoyancy flushed during the initial exponential decay ($1 - \Gamma_e$) versus Ri number for. η=0.45, 0.75, -1, 2.

3.6. Comparison with the other studies

There are multiple studies in the literature that have presented results of individual experiments or simulations that consider flushing of a dense fluid from a cavity or canyon (see table 3.3). In this section these results are compared to the empirical expressions developed in this study. For each published result, the estimated decay rate, k, is calculated using (2.16) and compared to the published flushing rate in Figure 3.14. Excluding Caton et al. (2003) and Chang et al. (2007b), the exponential rate of pollutant removal from the canyon, k, for all the numerical or experimental data in table 3.3 was calculated from steady state experiments or simulations. For a steady-state flow the exponential rate is

$$k = \frac{U}{Ht_r} \tag{3.4}$$

Which t_r is the time scale for flushing, given by

$$t_r = \int \frac{\bar{C}dV}{Q}. \tag{3.5}$$

which $\bar{C}$ is the average pollution concentration in the canyon, V is the volume of the canyon and Q is the rate at which pollution is released from a ground source. The reference velocity used in each study is either the upstream velocity which is assumed to be uniform (e.g. Cheng and Liu 2011) or the velocity at a reference height above the plane of the canyon top (e.g. Cheng et al., 2009).

Table 3.3: Some studies on the effect of aspect ratio and Richardson number.

	η	Ri	number of upstream cavities	upstream velocity profile	
Chang et al., 2007b	2	0, 0.2	0	channel flow	CFD
Caton et al., 2003	1	0	0	free stream flow	EXP
Cheng and Liu 2011	1	0, 0.18, 0.35	1	free stream flow	CFD
Cheng et al., 2009	1	0	6	power law	CFD
Liu et al., 2005	0.5,1,2	0	∞	free stream flow	CFD
Cheng et al., 2008	0.5,1,2	0	6	free stream flow	CFD

To compare the calculated k from (2.16) with the existing data, the corresponding coefficients in table 3.2 were employed for different aspect ratios (η=0.5, 1, 2). The coefficients for η=0.75 and 0.45 in that table were used to interpolate an equation for η=0.5. For the experiments published in this paper, 90% of the experimental data fell between ±40% of equation (2.16). This error range is indicated by the dashed lines in Figure 3.14. There are clearly

significant differences between the empirical prediction of the flushing time based on the experiments conducted in this study, and those previously published in the literature. In fact there are significant differences between the previously published studies. For example, the second top row of five points are all for a square cavity and Ri=0. The k values for these points range from 0.01 to 0.025.

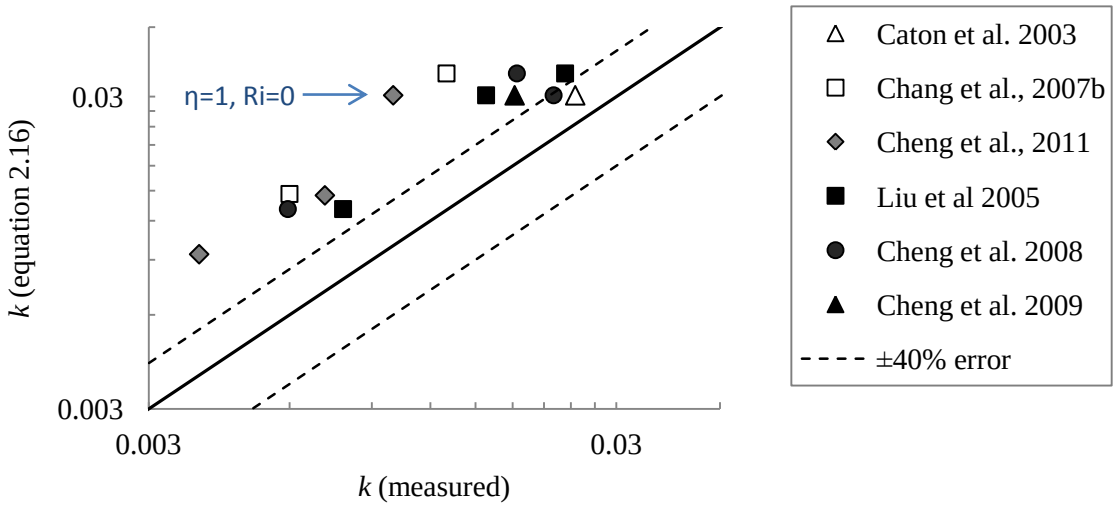

Figure 3.14: Comparison of initial flushing rate based on Eq.2.16 and previously published data. The hollow symbols are based on published decay rates from finite release studies and the solid symbols are based on steady-state studies using Eq. (3.4 & 3.5). The solid line is the line of 100% agreement, dashed lines shows 40% error.

All of the data from previous studies lie above the line implying that the measured decay rates are smaller than those measured in this study. There are a number of explanations for this. First, the different studies use different reference velocities for scaling time. The most significant difference however is the geometry. In all the previously published data in table 3.3 the multiple cavities geometry (appropriate for urban canopies) are used (refer to Table 1.1) while in this

study we focused on street canyon (suitable for open country). As shown in chapter one, Figure 1.2, for the cavity geometry case, the upstream flow has been a skimming flow with the boundary layer flowing at roof height, whereas, in the case of an isolated canyon, the boundary layer is at ground level. The resulting flow separation over the roof top significantly alters the flow kinematics and results in higher velocities over the top of the cavity compared to a fully developed boundary layer skimming over the roof top.

3.7. Conclusions

In this study the effect of aspect ratio on flushing a dense fluid from a canyon was examined. Four series of experiments for different aspect ratios (η=0.45, 0.75, 1, 2) were presented and the qualitative and quantitative results were discussed. Each series of tests was conducted for a range of Richardson numbers.

It was shown that increasing the Richardson number and decreasing the aspect ratio results in a stronger stratification. The effect of aspect ratio on the initial flushing is discernible from the interface deflection depth which increases with η (Figure 3.2). The in-canyon flow regime also changes as a result of changing the aspect ratio. For large aspect ratios, the vortex in the canyon penetrates more deeply into the dense layer compared to the narrow canyon. As a result, the density interface gets more diffuse and thicker and a weaker stratification is maintained compared to the lower aspect ratios (Figure 3.4 & 3.6). The flushing rate is also influenced by changing η. A small canyon width restricts the vortex size and strength. Therefore, less dense fluid is skimmed from the top of the dense layer and the flushing time increases. Thus narrow street canyons represent the worst case in terms of ventilation. For aspect ratio two, although the flow regime is different, the flushing rate and time are similar to those for η=1.

For all aspect ratios the concentration is higher at the leeward side of the canyon, due to the counterclockwise vortex located at the downstream side of the canyon (first row in Figure 3.1). This is consistent with studies that examined the flushing of a neutrally buoyant pollutant (Cheng et al., 2008).

CHAPTER FOUR

EFFECT OF UPSTREAM SURFACE ROUGHNESS

In this chapter the effect of upstream surface roughness on the pollutant removal from a single canyon is investigated experimentally. Three series of tests for different upstream surface roughness (d_{84}= 1.14, 0.83 and 0.0 cm) were conducted for a range of Richardson numbers. The results are discussed both qualitatively and quantitatively in order to compare the flushing rate and canyon flow regimes under each boundary condition, smooth and rough

4.1 Introduction

The upstream terrain has a significant effect on the wind flow in an urban area and it is usually parameterized in terms of a surface roughness length. The surface roughness height (z_0) affects the boundary layer turbulence (Jensen 1958, Roth 2000, Al-Jiboori, 2005) and hence the dispersion process (Deaves 1992, Roberts et al., 1994, Pascheke et al., 2008). Based on Macdonald et al. (1997), larger surface roughness generates high turbulence around the obstacles and within the urban canopy layer. The upstream flow condition, the surface roughness length scale, z_0 and especially turbulent intensity are reported as important parameters in urban canyon studies (Sini et al., 1996). A number of different studies indicate that the turbulence properties of the upstream flow effect the dispersion of a neutrally buoyant pollutant (Caton et al., 2003, Kim and Baik 2003, Huang et al., 2000, Rotach, 1999). An analytical study by Caton et al., 2003 showed that the flushing timescale (the time to complete the

ventilation and removal process) of a neutrally buoyant pollutant decreases by increasing the external velocity, turbulence intensity, and turbulence length scale.

Kim and Baik (2005) experimentally, and Kim and Baik (2003) numerically, investigated the effect of Inflow turbulent intensity on the in-canyon flow. It was shown that increasing the turbulent intensity raises the turbulent kinetic energy, increases turbulent mixing and enhances the pollutant flushing rate. Huang et al. (2000) mentioned that both the turbulent intensity profile and mean velocity profile of the upstream flow are important factors in urban pollution dispersion.

Cheng et al. (2008) emphasized that both the mean flow and the turbulence parameters influence the ventilation process of neutral buoyancy pollutants. They demonstrated that the mean flow induces pollutant removal at the windward side and the turbulence induces ventilation at the leeward side of the canyon. Chang et al. (2007a& b) examined the difference between a laminar and a turbulent upstream boundary layer for negatively buoyant pollution. It was shown that the turbulence intensity accelerates the flushing rate of the pollutant due to a stronger and bigger vortex within the cavity.

The majority of cavity flushing studies use only the upstream boundary layer mean velocity to parameterize the flow (e.g. Strang and Fernando, 2004). In case of shallow upstream flow the depth of the layer was also considered as an important parameter (e.g. Armfield and Debler 1993; Debler and Armfield 1997; Kirkpatrick and Armfield 2005 and Kirkpatrick and Armfield, 2012). Debler and Armfield (1997) used a hand-held food mixer at the upstream of the cavity in several of their experiments to investigate effects from upstream turbulence on the rate of purging. Considering that the scale of the turbulence generated was small compared to the flow, no significant change was observed in the results.

The study presented herein examines the role of three different upstream boundary layer properties on the flushing time for a dense pollutant. In total 54 experiments were run for a range of Richardson numbers for the upstream topography considered. Section 4.2 describes the experimental procedure and section 4.3 describes the results and the effect of different upstream boundary layer properties on canyon flow regime. The flushing rate and mechanism are discussed in section 4.4 and 4.5 respectively. The conclusion is presented in section 4.6.

4.2 Experimental procedure

In general, the surface morphology should be considered as a parameter in any model. Larger surface roughness generates higher turbulence within the urban canopy layer. It is therefore important to know the roughness length used in any experimental model (Macdonald et al. 1997).

To investigate the effect of upstream surface roughness and consequent change in inflow turbulence properties, a series of experiments were run using a canyon model with aspect ratio η=1 and two different upstream surface morphologies created using a gravel bed of aggregate sizes d_{84}=0.83 cm and d_{84}=1.14 cm. A further set of tests were run for a smooth plate upstream of the test section. The velocity profiles and the effective aerodynamic surface roughness estimation (based on Smart, 1999) for each upstream morphology are shown in Figure 4.1a,b&c. The turbulence intensity profiles are shown in Figure 4.1d. During each experiment the mean velocity (U) and turbulence intensity (I) was measured using an ADV. Otherwise, the experiments were conducted in a manner identical to that described in chapter 2.

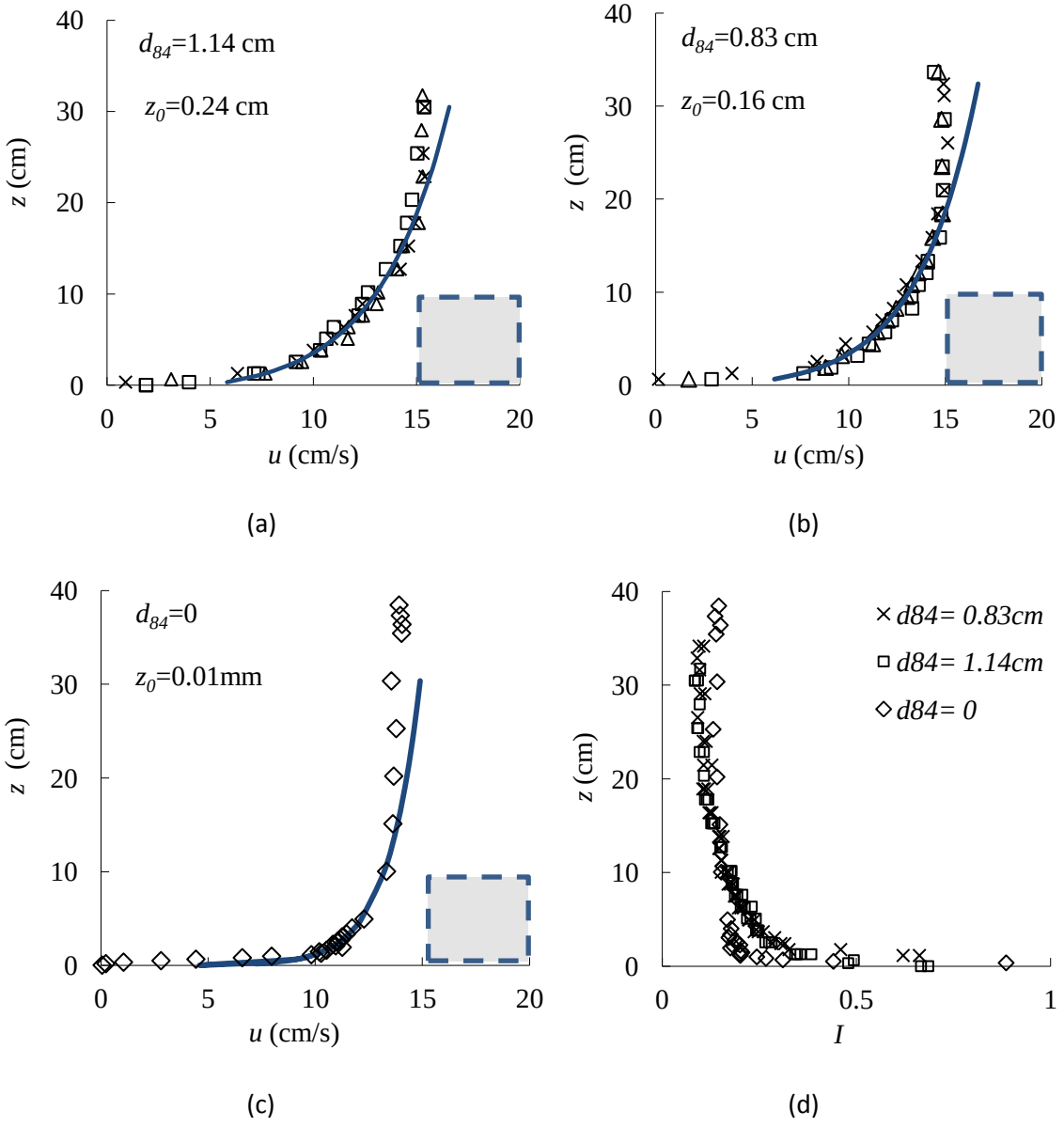

Figure 4.1: Vertical velocity profiles with the best fitted logarithmic profiles for gravel bed size of a) d_{84}=1.14 b) d_{84}=0.83 cm, and c) the smooth turbulent boundary layer. d) Turbulent intensity profiles for all three surface parameters. The block represents the height of the model buildings.

4.3 Flow characteristics

Qualitative investigation of the effect on the flow structure caused by up-stream surface roughness was undertaken. The scaled initial interface deflection, d/H, maximum interface thickness, δ, and the observed flow regimes during the tests were examined for each upstream bed morphology. Changing the upstream surface roughness was not observed to have a significant effect on the initial stage of the purging process compared to changing the canyon aspect ratio (see section 3.3). Figure 4.2 compares the initial deflection on the interface surface following the abrupt initiation of flow in the flume. Although the flow was able to penetrate slightly deeper into the canyon for d_{84}=1.14 cm, the results of d_{84}=0.83 cm and the smooth bed channel are indistinguishable.

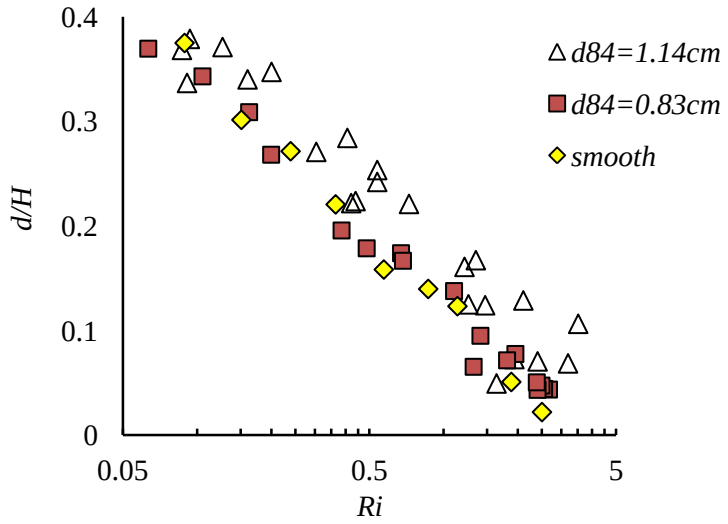

Figure 4.2: initial deflection difference for rough (d_{84}=1.14 & 0.83 cm) and smooth channel.

Figure 4.3 presents the maximum measured density interface thickness for each test plotted against the Richardson number showing that the interface sharpens (δ decreases) with

increasing Richardson number. There is considerable scatter in the observed maximum interface thickness and no clearly discernible difference is seen between the different upstream morphologies. This suggests that the initial purging is dominated by the large scale mean flow rather than by small scale turbulent mixing.

Sample scaled buoyancy profiles and contours for $Ri \approx 0.4$ are shown in Figure 4.4 for each of the three upstream bed morphologies. Based on the regime definitions given in section 2.3, the buoyancy profiles for the two rough channel conditions are in the transition regime (Figure 4.4a&b). This regime changes to the two-layer stratified regime for the smooth channel bed (Figure 4.4c).

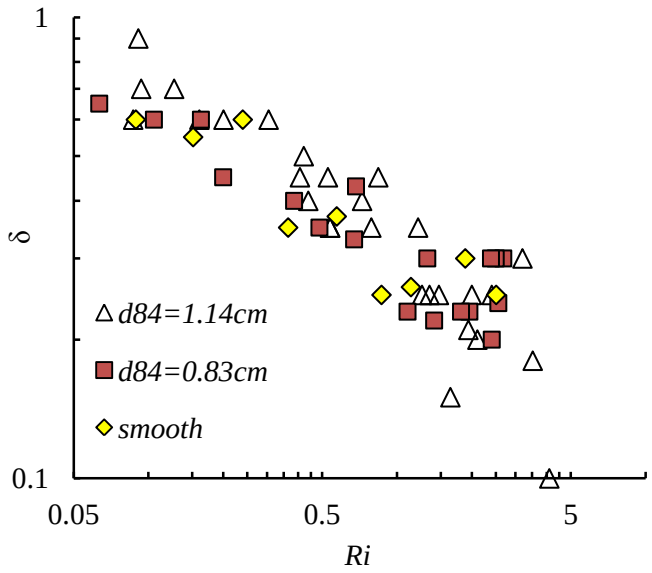

Figure 4.3: maximum thickness of the density interface, observed for each surface roughness, as a function of the Richardson number.

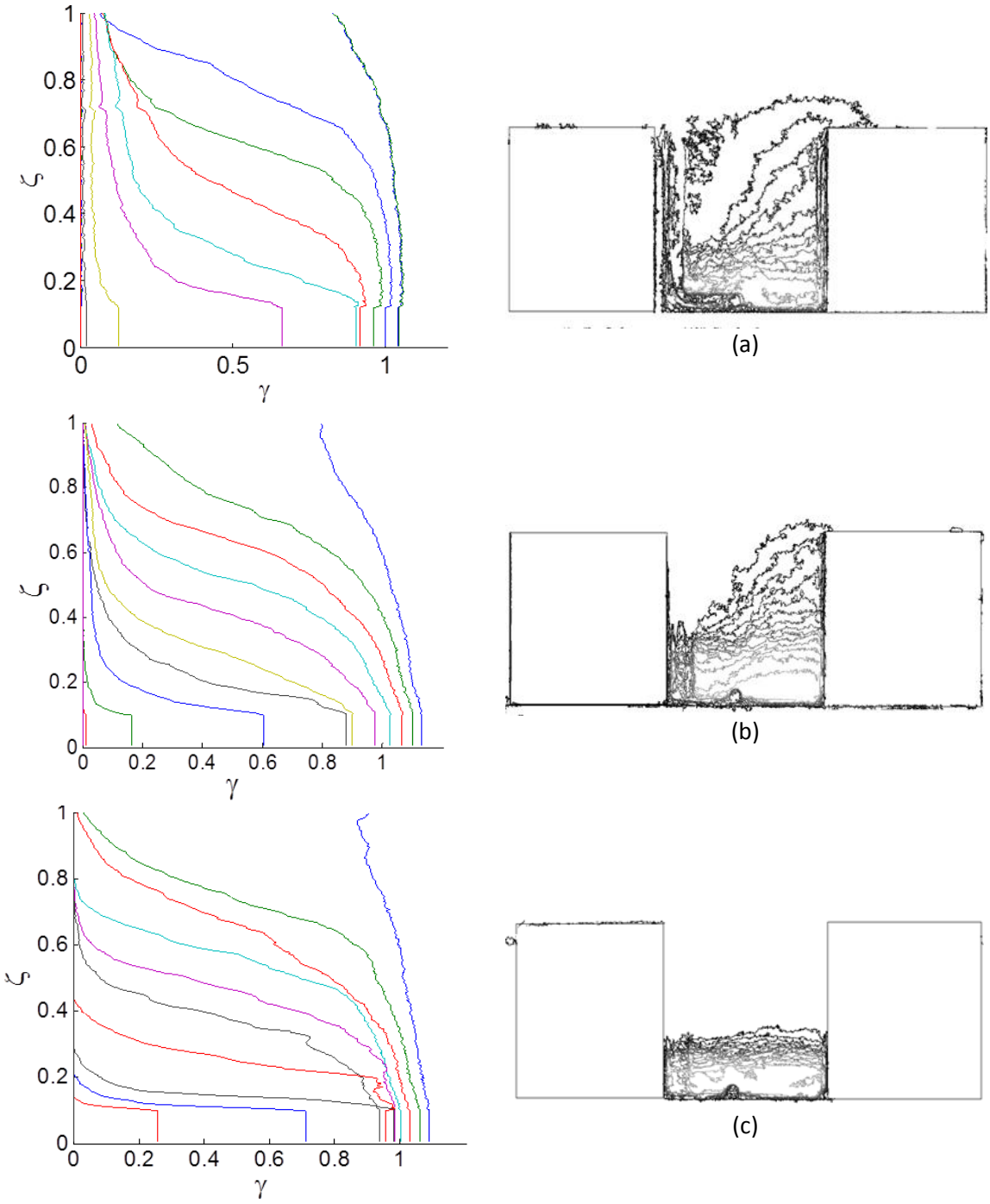

Figure 4.4: Contour plot images of the canyon concentration of different surface roughnesses for Ri≈0.4 at about 1/2 total time of flushing, along with the buoyancy profile at the equal time intervals during the test. First two rows are transition flow regime, last row is two-layer stratification. a) d_{84}=1.14 cm, b)d_{84}=0.83 cm, c) smooth boundary layer.

The contour plots show that the mixing in the canyon is higher for the rough channel experiments and δ is bigger. Also the extent of the fluid drawn upstream diminishes as the thickness of interface decreases (Figure 4.4c).

Previous studies (e.g. Armfeild and Debler 1993) and present flow observation indicate that, in all cases, there is a recirculation flow inside the canyon on top of the dense layer. Since, for all three experiments shown in Figure 4.4, the velocity, aspect ratio and initial density were the same, it can be concluded that the upstream turbulent parameters influence the vortex structure and the mixing process inside the canyon. The flow regime for all boundary layer conditions are illustrated in Figure 4.5 based on inspection of the vertical buoyancy profiles as described in section 2.3.1. The smoother the upstream topography, and the higher the Richardson number, the more stable the stratification.

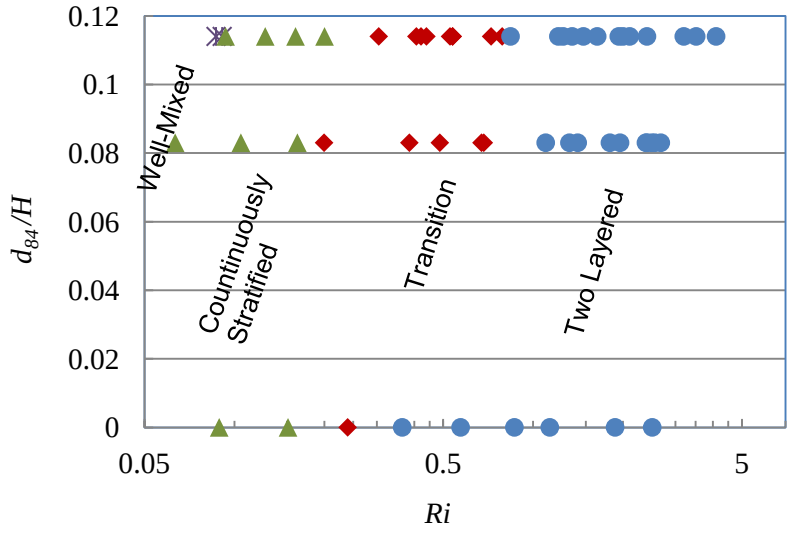

Figure 4.5: Different flow regime observed for each set of experiments and η=1.

4.4 Time of flushing

In the previous section it was shown qualitatively that the mixing process and density interface thickness are enhanced by increasing the upstream boundary layer surface roughness length. In order to quantify this enhanced level of mixing, the buoyancy decay profiles for all experiments were evaluated. Plots of the scaled total buoyancy in the canyon over time ($\Gamma(\tau)$) are presented in Figure 4.6 for Ri≈0.16, 0.4 &2.4. For the low Richardson number case ($Ri \approx 0.16$) the flushing profiles are the same regardless of the upstream surface roughness (Figure 4.6a). However, at higher Richardson number, the turbulence properties of the upstream boundary layer significantly influence the time rate of flushing. For all three decay rate plots, the initial flushing rate is not significantly altered by the upstream bed morphology. However, at later stages in the flushing process, and for higher Richardson numbers, there is a distinct divergence in the decay rate depending on the upstream surface roughness.

Figure 4.6c most clearly illustrates the difference in the rate of flushing over time at high Richardson number. The initial decay rate is independent of the surface roughness. However, once approximately 50% of the buoyant fluid has been flushed there is a transition in behavior. The decay rate increases for higher surface roughness and decreases for lower upstream roughness. This transition is discussed in detail at the end of this section.

The initial exponential decay rate was calculated for each of the 54 experiments conducted and is shown in Figure 4.7. An equation of the form of (2.16) was fitted through all initial phase data in Figure 4.7 regardless of the upstream surface roughness. The resulting equation,

$$k = \frac{1}{\left(19 + 88Ri\right)^{1.19}}, \qquad (4.1)$$

is plotted in Figure 4.7. This equation is almost the same as Eq.2.16 showing that the change in upstream surface roughness has no significant effect on initial exponential decay.

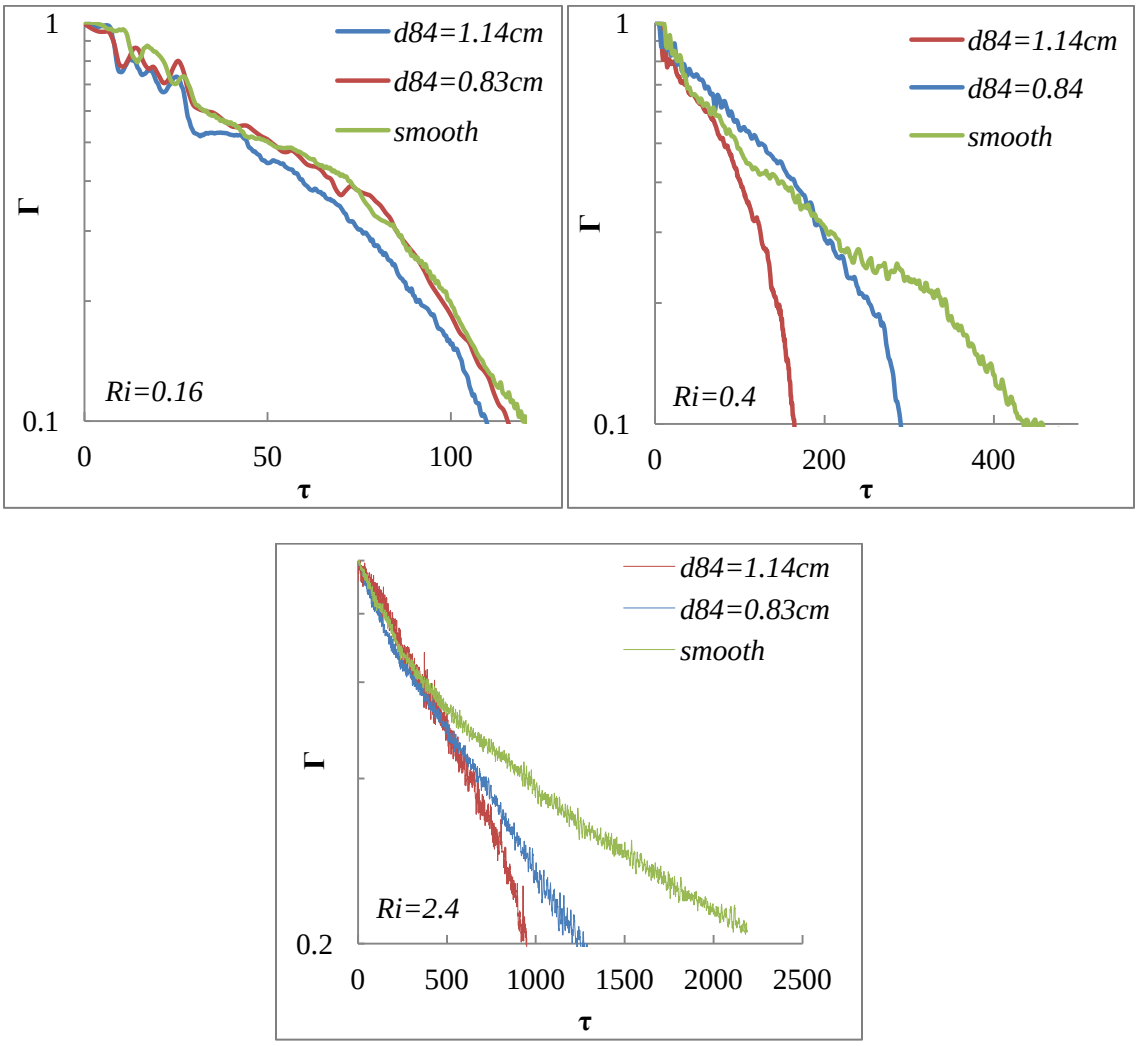

Figure 4.6: Buoyancy decay comparison for different Richardson numbers in canyon with aspect ratio=1, a) $Ri \approx 0.16$ b) $Ri \approx 0.4$ c) $Ri \approx 2.4$.

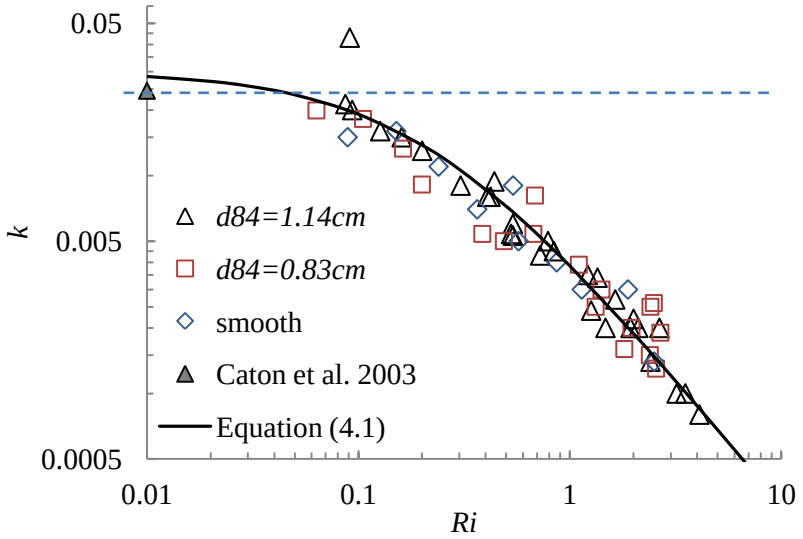

Figure 4.7: The exponential exchange coefficients for all surface roughness experiments. The data plotted on the vertical axis are data for a neutrally buoyant pollutant ($Ri = 0$). Dashed line show the k upper limit from Caton et al. (2003) for smooth channel flow, η=1.

While there is some scatter in the data in Figure 4.7, there is no discernible difference between the three sets of experiments. Consistent with the profiles plotted in Figure 4.6, it shows that surface roughness only influences the flushing rate at a later point in the process.

The effect on later stage flushing can be revealed by looking at Figure 4.8a showing the time taken to remove 90% of the initial volume of buoyant fluid. The higher the upstream surface roughness, the higher the measured turbulence intensity at the height of the model building roof, and the shorter the flushing time. However, there are some inconsistencies in the data in Figure 4.8a. For example, for $Ri \approx 0.6$ and $Ri \approx 2$ the measured time to flush 90% of the fluid for a smooth upstream bed is significantly below the other smooth plate data. Analysis of the raw data showed that these experiments were run at relatively low speed (Re<6000) and that the roof top turbulence intensity for these experiments was higher than for the other

smooth plate experiments. The increase in flushing rate for low Re numbers (Re<4500) was also reported by Briggs et al. (1990).

The data in Figure 4.8a were re-plotted in Figure 4.8b with the data segmented by bands of turbulence intensity rather upstream bed morphology. The resulting plot shows significantly greater consistency within each turbulence intensity band. As predicted by Caton et al. (2003), Eq. 3.3, the flushing time increases with decreasing the turbulent parameters. This is also consistent with the experimental results from Kim and Baik (2005).

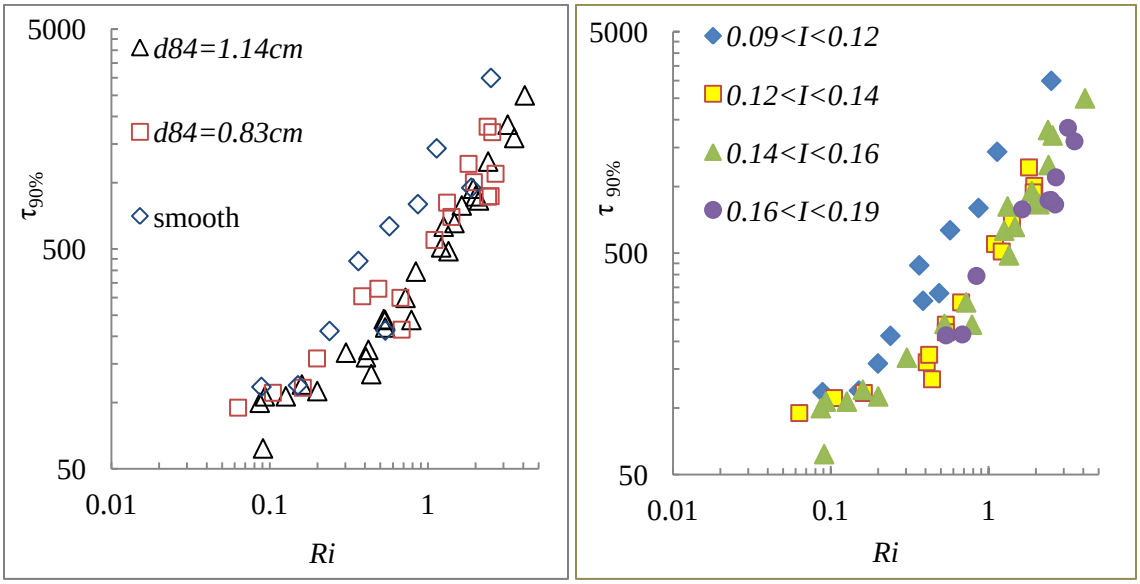

(a) (b)

Figure 4.8: The time of flushing 90% of the canyon buoyancy based on a) Richardson number b) turbulent intensity ranges.

This information strongly suggests that, for higher Richardson number ($Ri > 0.2$ based on Figure 4.8a), there is a transition in the flushing process. Figure 4.6 indicates that, for a given aspect ratio and Richardson number, the initial flushing rate is independent of the upstream

turbulence intensity. Therefore, the initial flushing is controlled by the mean flow rather than the upstream turbulence. After an initial exponential decay, there is a rapid transition to a new decay rate. The new rate is strongly dependent on the upstream turbulence intensity and must therefore be due to the influence of small scale turbulence on the mixing process in the canyon. In summary, two stages of the purging process can be explained as follows:

1. Initial purging is due to the mean flow and the large vortex at the downstream end of the canyon.
2. Transition to smaller scale mixing (due to turbulent fluctuations) occurs once the mean flow has exhausted its capacity to skim the dense fluid. From this point on, the mixing is dominated by small turbulent eddies lifting patches of buoyant fluid up into the vortex above the interface. These patches are then rapidly mixed and swept out of the canyon and up into the ambient flow above.

Kirkpatrick and Armfield (2005) also showed that the first three stages of the purging process (see section 2.1) can be modeled accurately by large eddy simulation. But the streamers, leaving the interface surface at the last stage, cannot be parameterized adequately by LES since they are formed by the small turbulent eddies.

For Richardson numbers greater than 0.2, Figure 4.9 shows the thickness of the dense layer and the fraction of the buoyancy remaining in the canyon at the time of transition (for example the test in Figure 4.6c).

Figure 4.8b indicates that above $I \approx 0.12$ the time to flush 90% is only weakly dependent on the turbulence intensity, whereas for lower intensities, the flushing time increases significantly. The introduction of a correction factor to the Richardson number of $I^{-3/2}$ was found to collapse the data onto a single line. The resulting data is shown in Figure 4.10.

A function with the same form as (3.1) was fitted through the data of Figure 4.10 to yield an empirical expression,

$$\tau_{90\%} = \left(4.3 + 0.16 \frac{Ri}{I^{3/2}} \right)^3, \qquad (4.2)$$

for the time taken to flush 90% of the initial fluid. Equation (4.2) is also plotted in Figure 4.10.

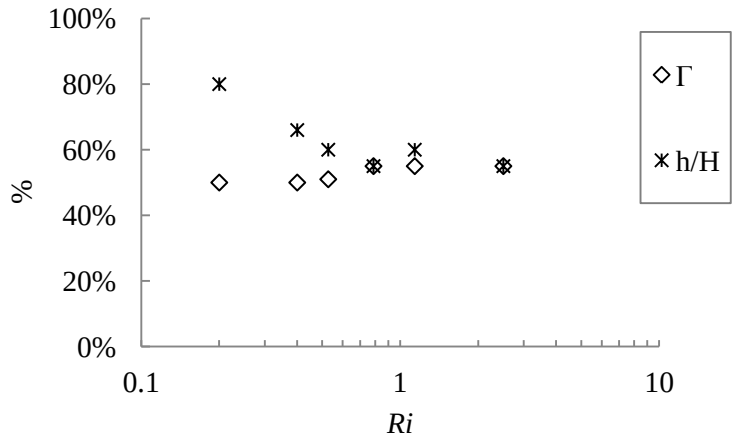

Figure 4.9: The height of interface surface and the fraction of buoyancy remaining in the canyon at the time of transition.

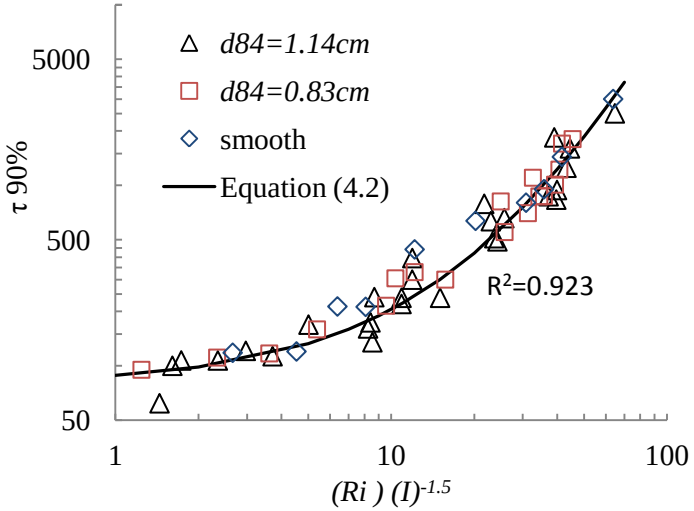

Figure 4.10: The time of flushing 90% of the canyon buoyancy versus Richardson number based on $Ri(I)^{-1.5}$.

4.5 Flushing mechanisms

Figures 4.11 a, b & c show the flushing decay changing due to increasing Ri number for d_{84}=1.14, 0.83 and 0 respectively. Comparing these graphs clearly demonstrates the turbulence intensity influence on flushing rate. For a rough boundary layer, d_{84}=1.14, 0.83 cm, the range of exponential decay, $1-\Gamma_e$, (based on the definition in Figure 4.11a) expands with increasing Ri number. However, for the smooth boundary layer in Figure 4.11c, a different behavior is observed.

As was explained in Chapter 3 (Sec.3.5) for the two-layer stratification regime, if the mixing across the interface is suppressed significantly, then the k value decreases with decreasing the height of interface surface. Interface mixing can be suppressed by narrow canyon width, very high Ri number and (based on this chapter's results) a low level of upstream turbulence intensity. This can be seen in Figure 4.11c for the smooth channel flow.

Figure 4.12 shows the fraction of the initial buoyancy flushed during the initial exponential decay for the different surface roughness experiments classified in the bands of turbulence intensities. For turbulence intensity less than 12% the decay rate decreases over time and the exponential decay range ($1-\Gamma_e$) shows significant difference from higher intensity experiments.

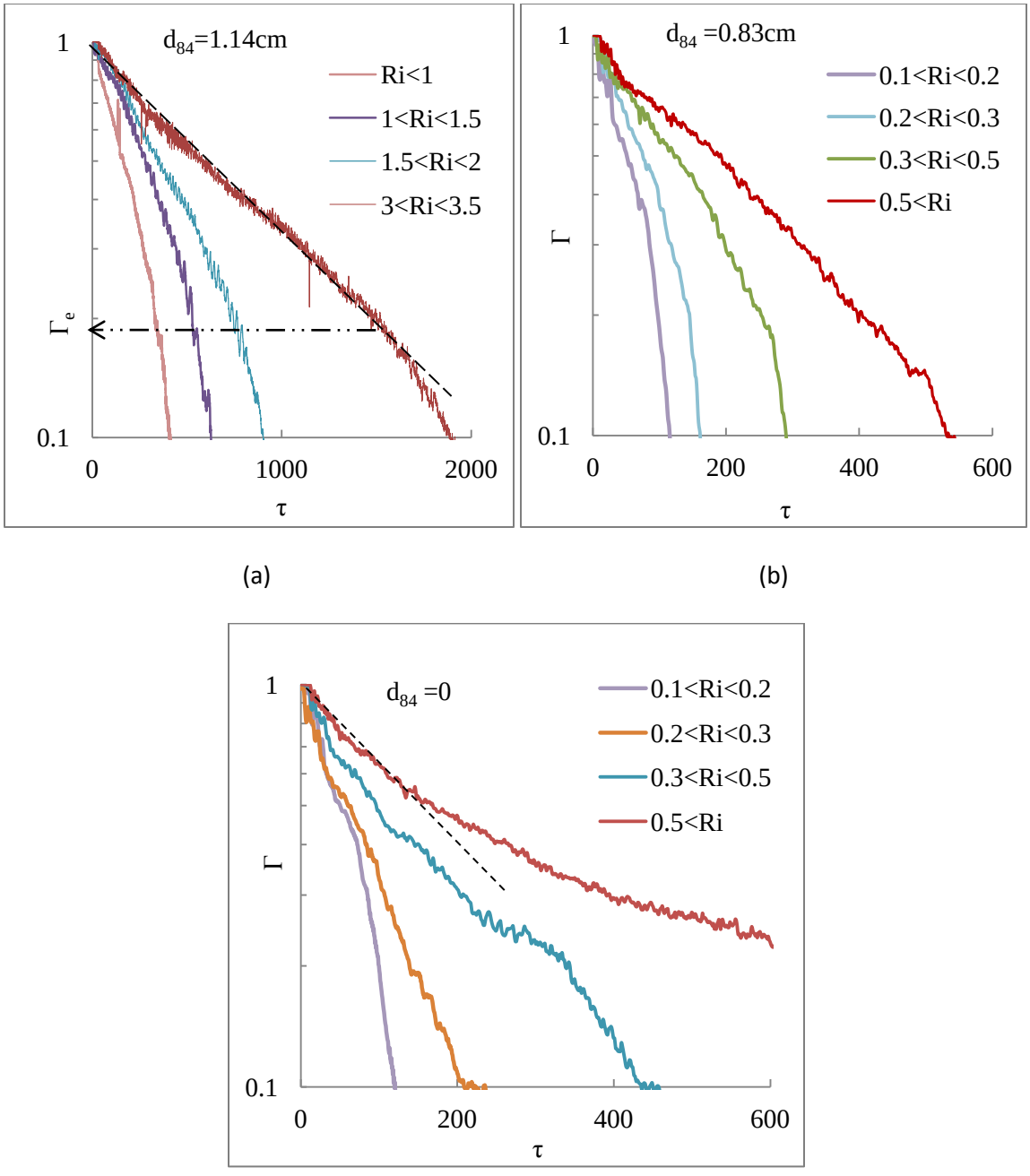

Figure 4.11: Flushing decay for a) upstream surface roughness d_{84} =1.14 cm b) d_{84} =0.83 cm and c) d_{84}=0.

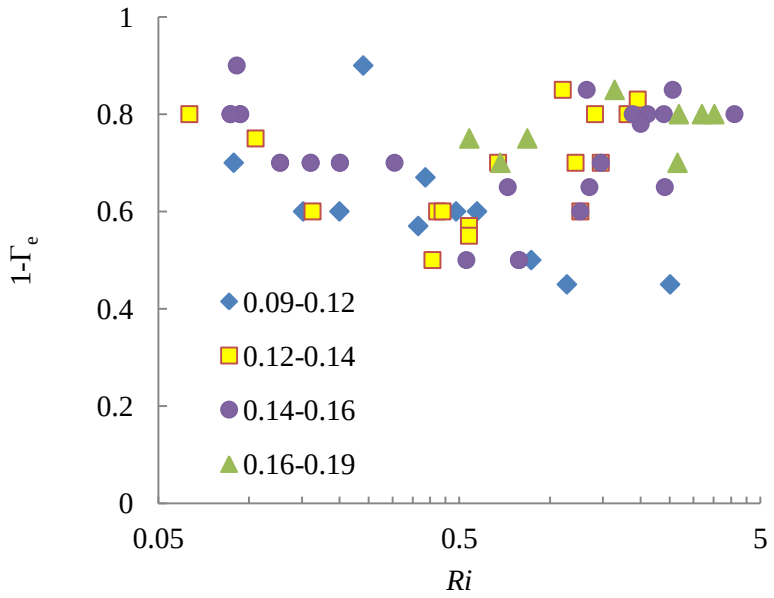

Figure 4.12: Fraction of the total buoyancy flushed during the initial exponential decay ($1-\Gamma_e$) versus Ri number for different turbulent intensity ranges. The lowest range shows different behavior than the other three ranges.

4.6. Conclusions

The effect of upstream turbulence intensity on flushing a dense fluid from a canyon was examined in this chapter. In section 4.3 three series of experiments for different upstream surface roughness and η=1 were compared. It was demonstrated that a dramatic change in results can be observed when the rough boundary layer is replaced by a smooth one. The change in inflow turbulence intensity changes the vortex properties inside the canyon and hence the regime of the stratified flow. Results from decreasing surface roughness are analogous to those from decreasing aspect ratio. Having a smooth boundary layer reduces the mixing in the canyon and increase the time of flushing. This effect in not clearly discernible during the first stage of each experiment, when the large scale flow dominates the mixing

process (Figure 4.6c, 4.7). The turbulent mixing transition from large scale to the small scale flow is discernible for Ri>0.2 in Figure 4.8 and it was observed to occur when about half of the total buoyancy is removed from the canyon.

CHAPTER FIVE

FLUSHING OF A CONTINUOUS RELEASE

In the previous chapters, the flushing of dense fluid from the canyon was investigated through experiments in which the basin contained a finite volume of stagnant dense fluid, representing an instantaneous buoyancy release condition. This chapter develops an analytical model for the flushing profile of a dense fluid based on the Richardson number for a canyon under a rough turbulent boundary layer (d_{84}=1.14 cm). The results of a series of steady-state experiments are presented to find the mixing parameters in the theoretical model.

5.1 Introduction

In the previous chapters, the flushing of dense fluid from the canyon was investigated through finite release experiments. Such experiments can simulate the case of an instantaneous accidental toxic release. However, conditions exist in which the release time scale is significantly longer than the time taken for dispersion (e.g., gas leaking from a pipe). These situations can be modeled by considering a continuous release of pollutant with a constant source emission rate. Also these types of experiments can be employed to find the rate of contaminant flushing by crosswind overflow. When the contaminant is released at a constant rate q_s, and the experiment is in an equilibrium (steady-state) condition, the rate of purging of the contaminant is the same as the pollutant inflow rate. Therefore, the flushing rate can be measured directly by measuring the rate of addition of buoyancy.

For a neutrally buoyant pollutant, Liu et al. (2005) and Cheng et al. (2008) used a continuous release model for a cavity with different aspect ratios to find the pollutant flushing

rate, k, at the steady-state condition (see Eq. 3.4 & 3.5). Caton et al. (2003) also analytically modeled the neutral contaminant decay when there is a continuous source of emission.

Continuous release of pollutant was also considered by some studies to examine the effect of thermal buoyancy on the rate of flushing by studying the steady state concentration (e.g., Cheng and Liu 2011; Cheng et al., 2009). In terms of density-driven buoyancy effects, Strang and Fernando (2004), Castro et al. (1993) and Briggs et al. (1990) used continuous release experiments. Running 92 steady state wind tunnel experiments on CO_2, Briggs et al. (1990) found the dense gas volume flux removal rate for a V-shaped topographical depression. They showed that, for high Re numbers and Fr numbers less than 1, the volume flux, v, depends on the reference velocity, U, on top of the dense gas pool and the reduced gravity acceleration, g':

$$v \propto \frac{U^3}{g'} \tag{5.1}$$

For low Re numbers, the molecular diffusivity and the width of the valley become important as well. Briggs et al. (1990) defined an empirical entrainment rate relationship applicable for both situations.

Similar depression geometry was used by Castro et al. (1993) in another wind tunnel study, albeit focused on low Ri numbers and using a low rate of source gas emission to avoid the pooling of the dense gas in the valley. Therefore, the two-layer stratifications observed in the finite release experiments presented in the previous chapters were not observed in their study. The concentration contour plots of their experiments are similar to those of the continuously stratified flow regime. The rate of flushing, k, was shown to depend on the Ri of the whole cavity

$$k = \frac{a}{(1+b\ Ri^c)} \tag{5.2}$$

in which a, b, and c are empirical constants found from the steady state experiments and

$$Ri = \frac{g'H}{U^2} C/C_s \tag{5.3}$$

where H is the depth of V-shaped valley, U is the wind velocity on top of the valley, C is the valley average concentration estimated by sampling, and C_s is the source concentration. The form of this equation is similar to that of the exponential decay rate k function presented in Chapter 2 and 4 (Eq. 2.16 & 4.1). A series of finite release experiments were also presented to verify Equation (5.2). Although Castro's wind tunnel results showed good agreement with the form of Equation (5.2) when c =0.5 and a =16.7, the constant value for b found by steady state and finite release experiments was not the same. This may be because the assumption of a well-mixed regime in the cavity was incorrect, or because of the dependency on the actual concentration stratification over the depth.

For high Ri numbers for which the interface height is discernible, Debler and Armfield (1997) presented an equation to calculate the entrainment rate based on finite release experiments. They employed an energy and mixing efficiency model for parameterizing the rate of flushing and the entrainment velocity at the interface. The flushing rate was dependent on the cavity geometry, Ri number, layer thickness, the upstream flow depth, and the velocity. However, their model only accounts for flushing by skimming of dense fluid from the top of the dense layer. Although their experimental results were in the range $0.45 < Ri < 31$, they did not consider mixing across the density interface, assuming that the flushing was largely due to skimming of dense fluid off the top of the layer.

Kirkpatrick et al. (2012), in a similar study, showed that the entrainment rate at the interface surface can be described by a power law function of the Richardson number. This study also focused on the two-layer stratification regime in the cavity. In summary, Caton et al.

(2003) and Castro et al. (1993) modeled flushing only as an exchange flow. Debler and Armfield (1997) and Kirkpatrick et al. (2012) only measured the rate at which the dense layer is skimmed over time so they did not account for the decrease in density of this layer. In this chapter, a series of steady-state experiments are presented in order to find the exchange rate coefficients experimentally for different buoyancies. In addition, a two-layer theoretical model is presented to predict the flushing rate of a buoyant pollutant from an isolated canyon under a turbulent rough boundary layer. It is the goal of this chapter to quantify both exchange and skimming flow for high Richardson number flow and to improve the models presented by Caton et al. (2003) and Castro et al. (1993) for neutral and low Ri number flows.

5.2 Theoretical analysis

In the theoretical framework of this study, a simple two-layer stratification model is considered for the exchange of a dense pollutant from an idealized street canyon (Figure 5.1). Assuming that the mixing above the buoyant layer is rapid compared to transport across the density interface, we can take the fluid directly above the dense layer to be at the ambient conditions ($g'_a = 0$).

A canyon of width W and depth H was considered with a lower layer of buoyancy g'_l and depth h, with a rooftop wind speed of U (Figure 5.1). The finite release experiments described in the previous three chapters show that, for a two-layer stratification, the layer depth and the layer buoyancy decreased over time. Based on this observation during the experiments, the removal of the dense fluid is clearly carried out by two processes: skimming the dense fluid from across the density interface at the top of the dense layer (see Figure 5.2a) and an exchange flow that mixes the fresh fluid into the bottom layer (see Figure 5.2b).

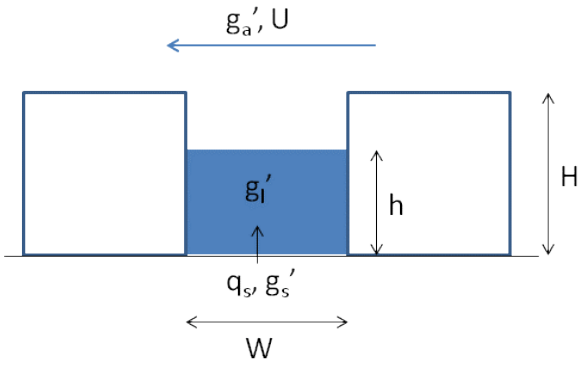

Figure 5.1: Two layer stratification model. g'_a, g'_l, g'_s are the ambient flow buoyancy, layer buoyancy and source buoyancy respectively.

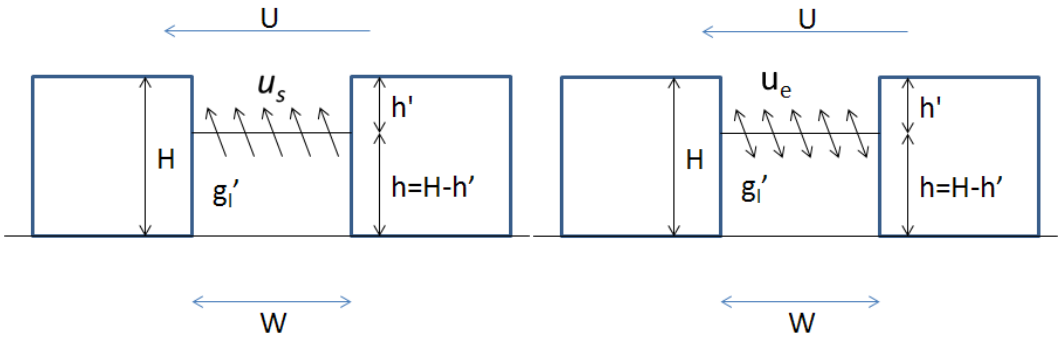

(a) (b)

Figure 5.2: a) Skimming the dense fluid from across the density interface. b) The exchange flow mixing the fresh fluid into the bottom layer.

The skimming flow accounts for the change in depth of the layer while the exchange flow changes the buoyancy of the layer over time. Therefore, we can write equations for the rate of change in the layer depth

$$\frac{dh}{dt} = -u_s \,, \tag{5.4a}$$

and layer buoyancy

$$h\frac{dg'_l}{dt} = -u_e g'_l. \tag{5.4b}$$

Superimposing these two situations in Figure 5.2, the time rate of change of the buoyancy in the canyon is:

$$\frac{d(hg_l')}{dt} = g_l'\frac{dh}{dt} + h\frac{dg_l'}{dt} = -g_l'(u_e + u_s). \quad (5.5)$$

Adding a source of buoyancy to (5.5) gives:

$$\frac{d(hg_l')}{dt} = -g_l'(u_e + u_s) + \frac{q_s g_s'}{W} \quad (5.6)$$

where q_s and g_s' are the source flow rate per unit length and source buoyancy respectively.

In the extreme case of a very high Richardson number, no mixing is observed into the dense layer (u_e=0) and all the flushing is carried out by the skimming flow (Figure 5.2a). On the other hand, when the Ri is very low, no buoyancy stratification appears in the canyon and it remains well-mixed (h=H). In this case, the skimming flow is equal to q_s/W, which means when there is no source of buoyancy ($q_s = 0$), then only an exchange process (u_e) accounts for the flushing of the dense fluid (u_s=0).

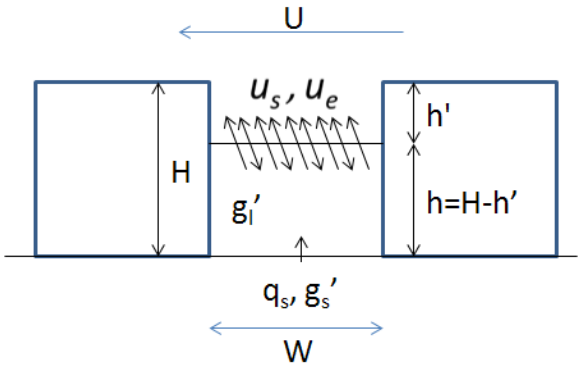

Figure 5.3: Superposing skimming and mixing process.

If the exchange velocity (u_e) is parameterized in terms of an entrainment coefficient (α) such that the fluid exchanged per unit width is given by

$$u_e = \alpha U, \tag{5.7a}$$

and the skimming parameter (β) is defined as

$$u_s = \beta U. \tag{5.7b}$$

Substituting (5.7a) and (5.7b) in (5.4a) and (5.6),

$$\frac{dh}{dt} = -\beta U + \frac{q_s}{W}, \tag{5.8}$$

and

$$\frac{d(hg_l')}{dt} = -g_l' U(\alpha + \beta) + \frac{q_s g_s'}{W} \tag{5.9}$$

Defining non-dimensional parameters as:

$$\Gamma = \frac{\int g' dA}{g_s' HW}, \tag{5.10}$$

$$\gamma_l = \frac{g_l'}{g_s'}, \tag{5.11}$$

$$\zeta_i = \frac{h}{H}, \tag{5.12}$$

$$\tau = \frac{tU}{H}, \text{ and} \tag{5.13}$$

$$\varphi = \frac{q_s}{UW}, \tag{5.14}$$

and assuming that there is no significant buoyancy in the upper layer (that is, $hg_l' = \Gamma$),

Equations (5.8) & (5.9) can be written in a non-dimensional form as:

$$\frac{d(\zeta_i)}{d\tau} = -\beta + \varphi, \text{ and} \tag{5.15}$$

$$\frac{d(\Gamma)}{d\tau} = -\gamma_l(\alpha + \beta) + \varphi. \tag{5.16}$$

The parameterization of the entrainment coefficients (α, β) can be estimated experimentally from steady state experiments, when the differential term in (5.15) and (5.16) are zero:

$$\beta = \varphi \tag{5.17}$$

$$(\alpha + \beta) = \frac{\varphi}{\gamma_{ss}} \quad (5.18)$$

where γ_{ss} is the non-dimensional buoyancy of the layer at steady state. From (5.17) & (5.18) the relationship between (α+β) and β at the steady state condition is

$$(\alpha + \beta) = \frac{\beta}{\gamma_{ss}}. \quad (5.19)$$

As explained before, when the Richardson number increases, γ_{ss} tends to one so the α value goes to zero showing a low level of the mixing into the layer.

5.3 Experimental procedure and results

To find empirical equations for α and β, a series of the continuous release experiments were conducted for different Ri and q_s. The experiments were run until a steady state was reached with a constant canyon buoyancy. The same set-up as in Chapter 2 was used for the steady state experiment. The test procedure was slightly different, as explained below.

Tests were conducted for a canyon with aspect ratio (η=1). Different source inflows, q_s, source buoyancies, g'_s, and overflow velocities, U, were used. Density and flow rate of the fluid emitted from the evenly perforated pipe were kept constant over the course of any given experiment. Constant density was provided by the large volume of salt water prepared in the constant head tank. Constant rate of buoyancy emission was controlled by a calibrated inline rotameter flow rate meter (Figure 2.5). Tests were run until the total buoyancy in the canyon did not change over time, that is, until it reached a steady state. At this time the rate of flushing of dense fluid from the canyon is the same as that of the emissions from the perforated pipe. For high Richardson numbers, the tests were stopped when the thickness of the layer in the cavity was observed to be constant over time. For low Ri numbers, the tests usually reached a steady

state faster, so running the experiments for a considerable amount of time (about 15 minutes) assures a valid result.

The initial condition in the experiments could be either a full or an empty canyon. The graphical examples of the horizontal averaged buoyancy profile over time are shown in Figure 5.4 for each of these initial conditions.

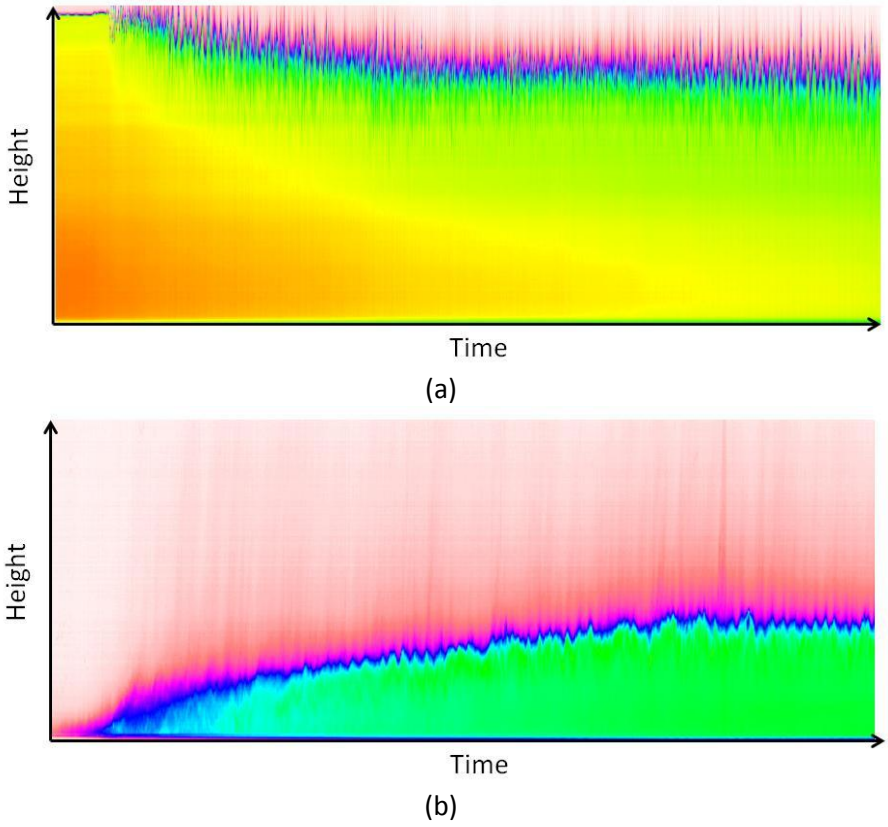

Figure 5.4: Horizontal averaged buoyancy over the time at a) a full canyon initial conditions, number (Ri_s= 3.52), b) an empty canyon initial conditions, number (Ri_s = 2.66).

In this study the majority of the experiments were run using a full canyon initial condition. A few experiments were conducted with an initially empty canyon to compare the

results. Regardless of the initial condition, the buoyancy of the source was used to scale the data. Although the LAT was employed in all experiments to measure the buoyancy in the canyon at any time of the experiment, the densitometer was also used to measure the density of samples taken at the steady state time.

Tests were conducted for a wide range of source Richardson number ($Ri_s = g_s' H/U^2$) and inflow rate, q_s. The interface height, ζ_i, can be found at any time, using the method explained in Chapter 2 (Figure 2.17). The total buoyancy in the canyon and the buoyancy of the layer were calculated from Equations (2.11) and (2.13) respectively. Examples of ζ_i and Γ profiles over time for a continuous experiment are shown in Figure 5.5.

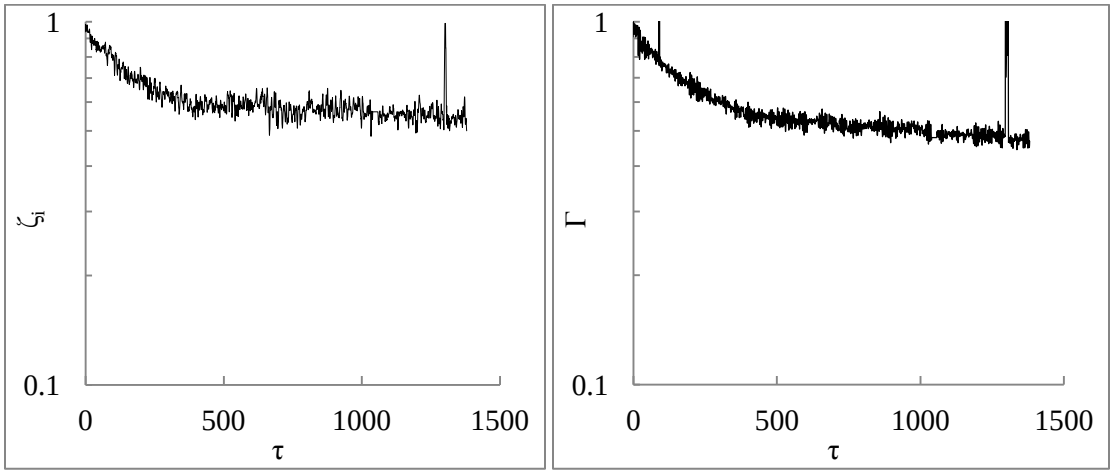

Figure 5.5: ζ_i, Γ profiles for a continuous release experiment test, Ri= 1.35.

Depending on the Richardson number and inflow rate, q_s, the regime of the steady-state stratified flow in the canyon differs. Figure 5.6 shows examples of two-layer and continuously stratified flow regimes. For continuous and well-mixed regimes, the interface

height is not clearly observable. However Figure 5.6, shows all the continuous release experiments for different Ri numbers and steady state interface height calculated, ζ_{ss}.

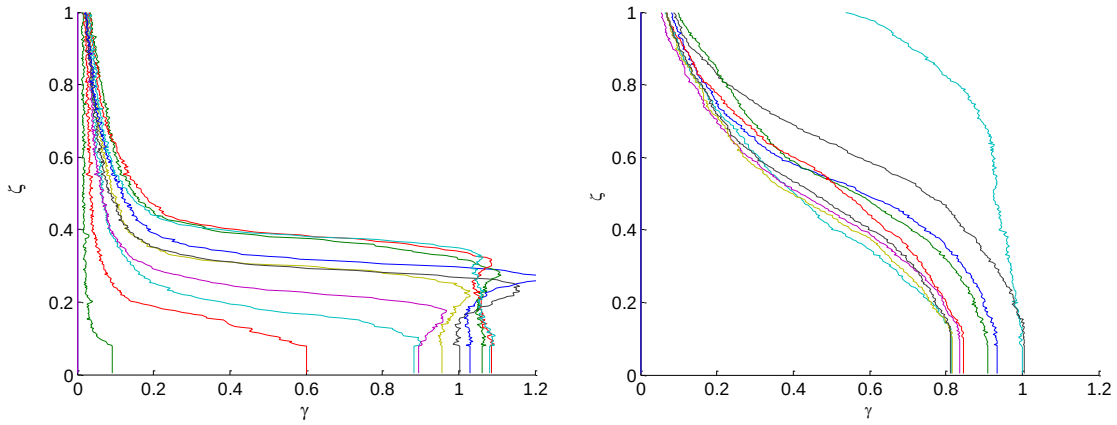

(a) (b)

Figure 5.6: Horizontal averaged buoyancy profile a) for two-layer stratification (empty canyon initial condition, Ri=2.66), and b) for continuous regime, where no interface is discernible (full canyon initial condition, Ri=0.72).

Recalling the deflection depth of the interface surface, d/H, at the initial stage of the finite release experiments (Figure 2.13), it is expected that two-layer steady-state tests cannot be run for $\zeta_{ss} = \frac{h_{ss}}{H} > (1 - \frac{d}{H})$. Therefore, the maximum expected value for ζ_{ss} was found from fitting a line through data for the deflection depth versus Ri, in Figure 2.13.

The initial condition of each experiment and the stratification regime based on the observed steady-state buoyancy profile is shown in Figure 5.7. Consistent with the finite release experiments in Chapter 2, it is hard to maintain a two-layer stratification when the Richardson

number is less than 0.8. For Ri<0.8 the interface height was not discernible, so the two layer model cannot be applied.

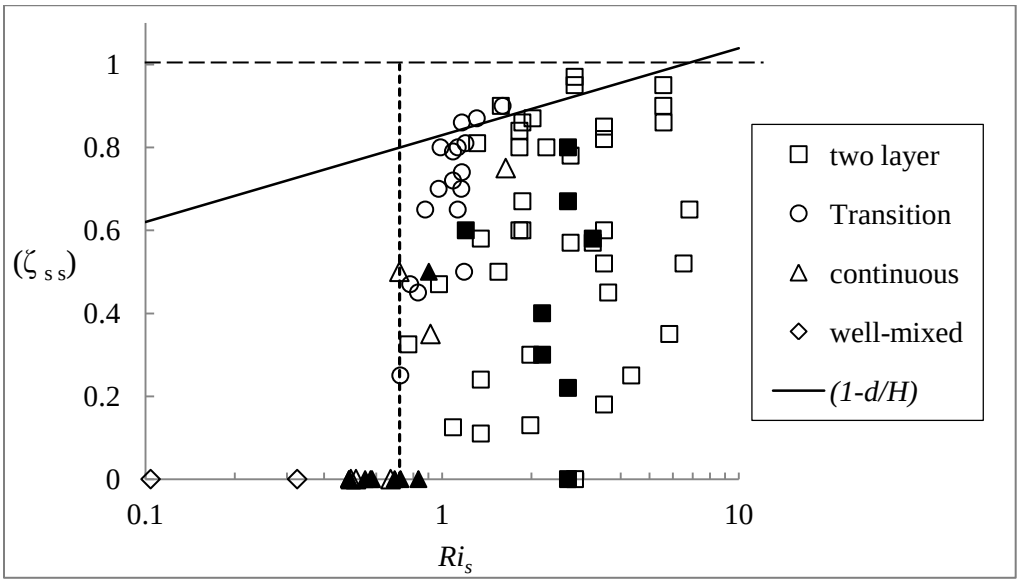

Figure 5.7: Total continuous release experiments conducted for different Ri numbers (η=1). The solid symbols are the tests with empty initial conditions. The vertical line shows the lowest Ri number in which that two-layer stratification regime was observed. The values on the horizontal axis are the tests at which no interface was observed.

The majority of the continuous release experiments were run for an initially full canyon. In order to investigate whether the effect of the initial condition on the steady state results is significant, multiple experiments were conducted for an initially empty canyon. The data showed that for high source Ri numbers, the results are the same. However, for intermediate Ri numbers and the empty canyon initial condition, the pool of dense fluid was not established due to the rapid mixing of the salt water at the time of emission. Therefore, the height of the interface surface is not clearly defined for that case. As an example, the buoyancy profiles of two experiments at high buoyancy and low buoyancy are presented in Figure 5.8 comparing

their different initial conditions. The Richardson number limit for the effect of initial conditions was not investigated in this study. Only the data in Figure 5.9 were used in analysis in this chapter in order to have consistency in the initial conditions and the range of overflow turbulent intensity.

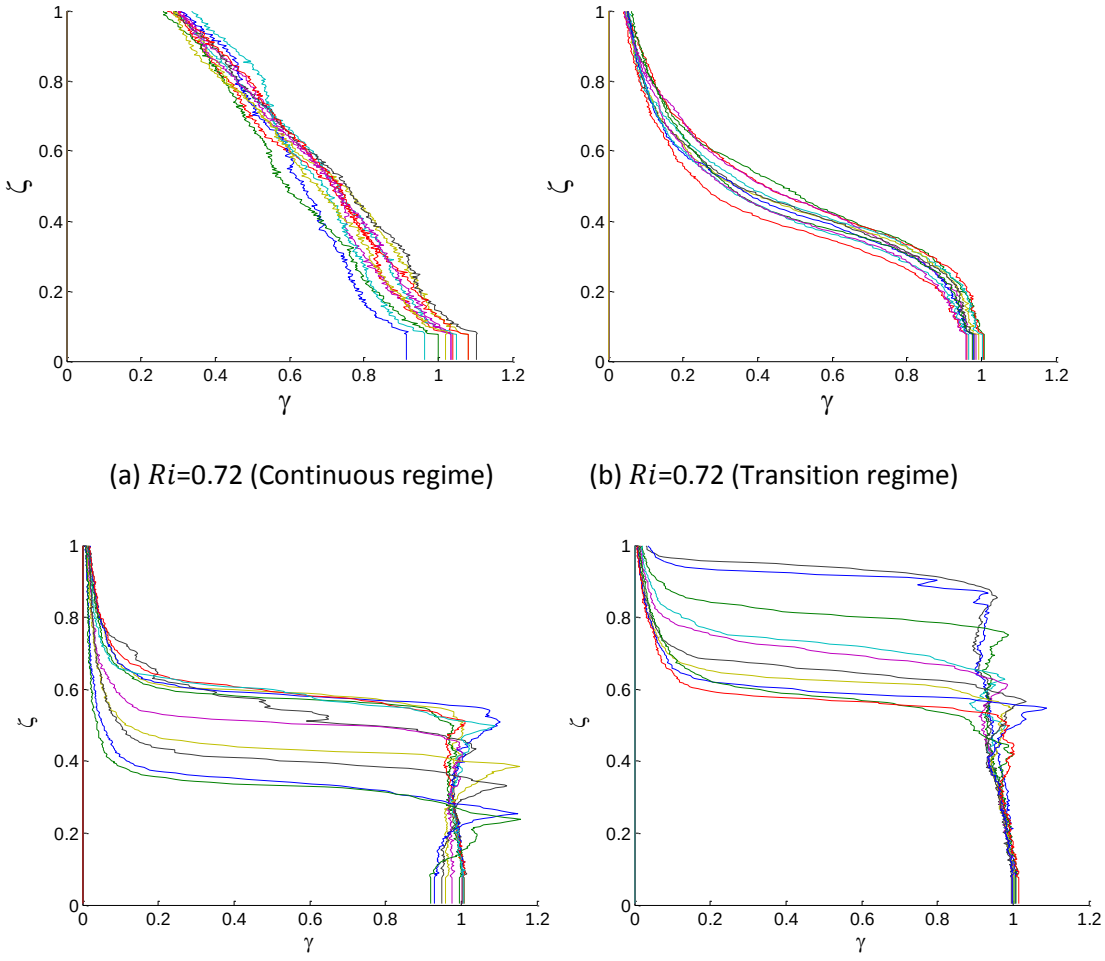

(a) Ri=0.72 (Continuous regime)

(b) Ri=0.72 (Transition regime)

(c) Ri=3.22 (two-layer)

(d) Ri=3.22 (two-layer)

Figure 5.8: Steady state buoyancy profile (a)&(c) empty canyon initial condition (b)&(c) full canyon initial condition

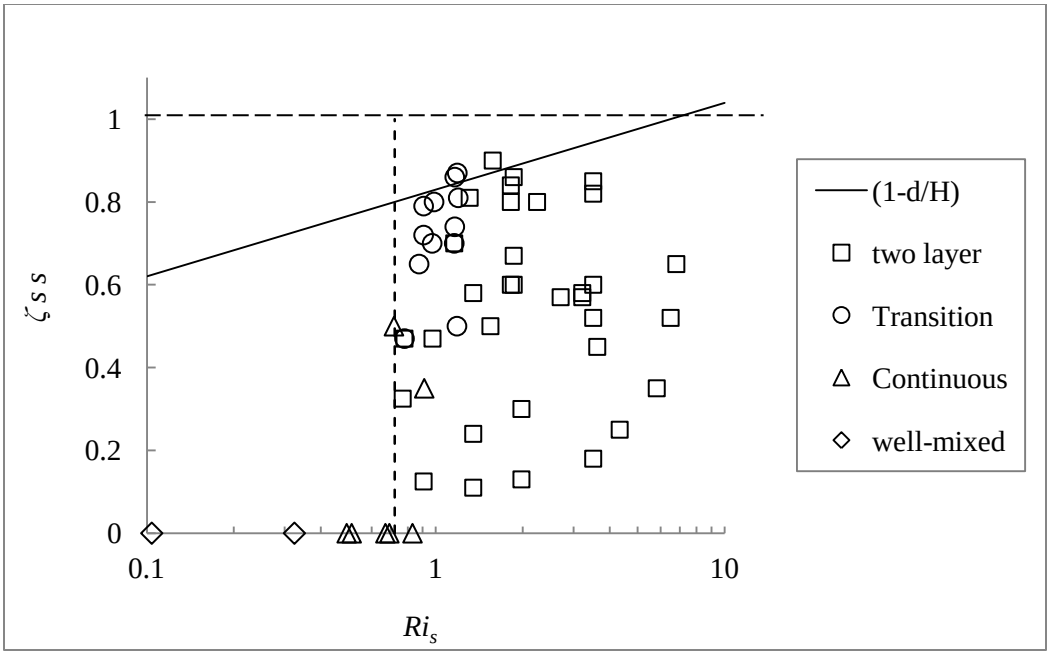

Figure 5.9: Total continuous release experiments employed for the modeling.

5.4 Model development

5.4.1 Two-layer stratification regime

To find empirical equations for α and β in the suggested model (Eq. 5.15 & 5.16), experimental values were calculated for all those data in the two-layer stratification regime. For each test, measuring the velocity, U, the source flux, q_s, the steady state interface height, h_{ss}, and steady state layer buoyancy, γ_{ss} , allowed α and β values to be calculated using (5.17) and (5.18). Figure 5.10 shows α and β values for each steady-state layer Ri number (that is, a Richardson number based on the layer buoyancy not the source buoyancy) $Ri_l = Ri_s\gamma_{ss}$ and the steady state interface height, h/H. The mixing coefficients are dependent on Ri_l and h/H, so

$$(\alpha, \beta) = f(Ri_l, \frac{h}{H}) \qquad (5.20)$$

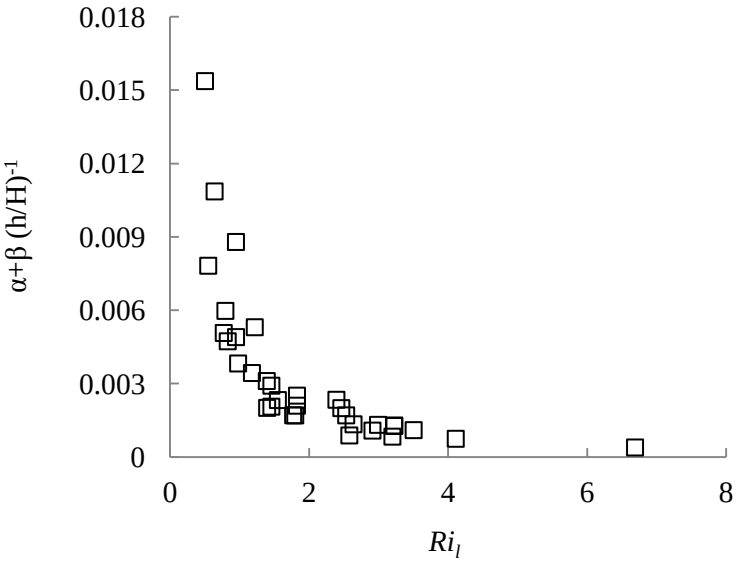

(a)

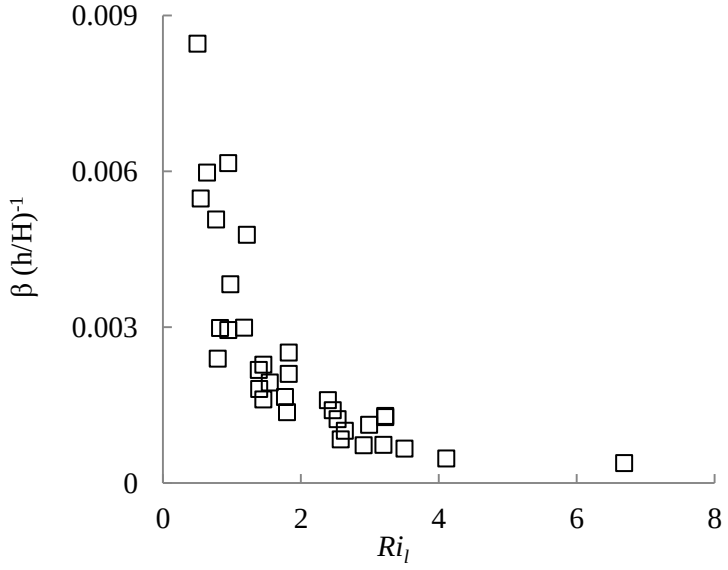

(b)

Figure 5.10: Skimming and exchange parameters as a function of layer Richardson number from steady state experiments.

Using an energy balance argument, Debler and Armfield (1997) relate the rate of supply of kinetic energy to the interface with the rate at which the flow gravitational potential energy is increased (by lifting dense fluid):

$$qg_l'(H-h) = \Delta KE = k_{ET}u^2UD \tag{5.21}$$

where q is the flow rate leaving the cavity (equal to q_s at steady state time), $\mathrm{k_{ET}}$ is a constant defining the mixing efficiency, u is the ambient velocity just above the interface, and D and U are the depth and the average velocity of the upstream flow respectively. From Eq. (5.21), they found a power-law function for skimming coefficients as:

$$\beta = \varphi = A\left(\left(1-\frac{h}{H}\right)\left(1-\frac{H-h}{D}\right)^2 Ri_l\right)^{-1} \tag{5.22}$$

where A(<1) is a mixing efficiency that depends on the cavity geometry. The second bracketed term accounts for the deceleration of the flow as it passes over the cavity due to the finite depth (D) of the overflow. For an infinite depth overflow boundary layer (large D) this term approaches one and β will be

$$\beta = A\left(1-\frac{h}{H}\right)^{-1}(Ri_l)^{-1}. \tag{5.23}$$

In their study α was considered to be very small so, for the continuous release case, Ri_l is the same as Ri_s.

Since $(\alpha+\beta) = \frac{\beta}{\gamma_{ss}}$, α also can be modeled as a power-law function of the layer Richardson number and layer thickness. Using the data in Figure 5.10 for α and β, two power-law equations were fitted, in the forms of

$$\alpha+\beta = m_1\left(\frac{h}{H}\right)^{m_2}(Ri_l)^{m_3} \tag{5.24}$$

$$\beta = n_1\left(\frac{h}{H}\right)^{n_2}(Ri_s)^{n_3} \tag{5.25}$$

where m and n are constant. Based on present experimental data, $m_1 = 4.61 \times 10^{-3}$,$m_2 = 1.0$, $m_3 = -1.27$, $n_1 = 3.33 \times 10^{-3}$, $n_2 = 1.0$, and $n_3 = -1.14$.

Using the empirical equations (5.24) and (5.25), the differential equations (5.15) and (5.16) can be solved to model the buoyancy flushing profile, the interface height decay, and the buoyancy of the layer over time for each finite or continuous release experiment.

5.4.1.1 Model verification with the finite release tests

The two layer model was employed to estimate the canyon buoyancy decay, Γ, and layer thickness profiles ζ_i. The results for different experiments from Chapter 2 are presented in Figure 5.11.

Figure 5.12 shows the time of 90% flushing, predicted by the two-layer model and equation (2.16) in Chapter 2. To evaluate the performance of the model, the calculated time of 90% and 50% flushing for each experiment is compared to the measured value in Figure 5.13. Almost all the data collapses well within the range of +/-40% agreement with the model.

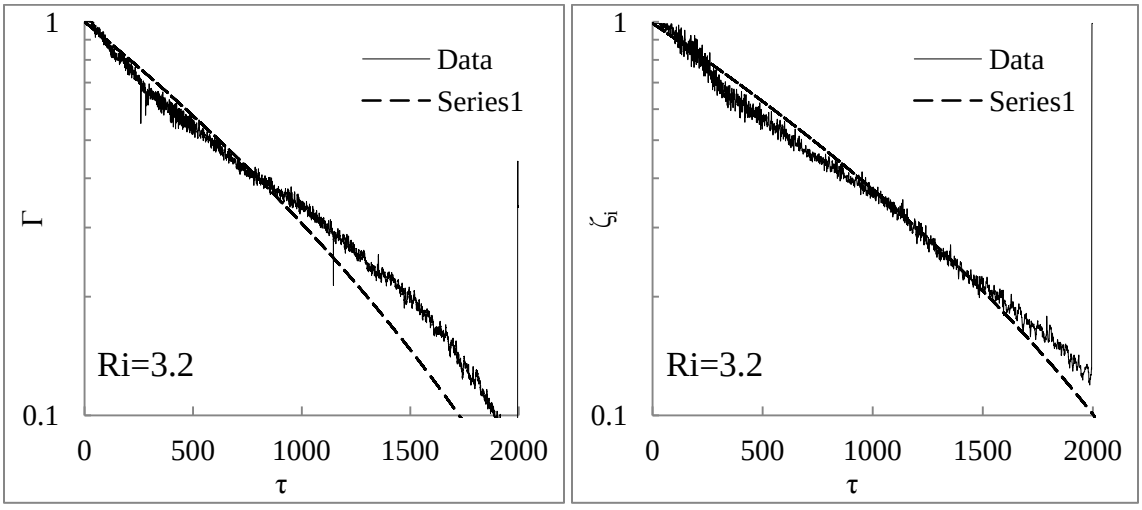

(a) (b)

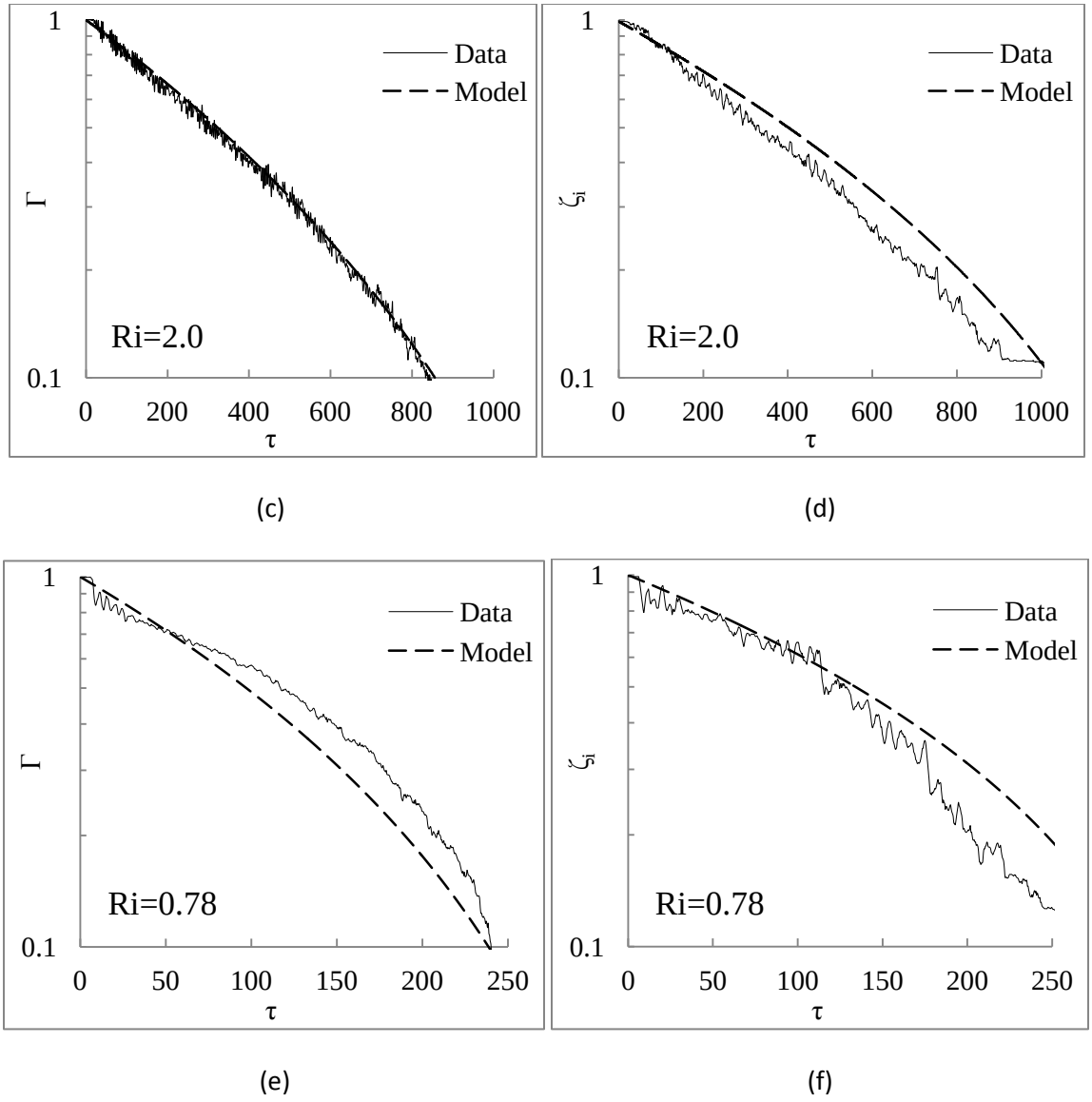

Figure 5.11: Model and data comparison for finite release experiments: (a, c, & e) are total buoyancy profile, Γ (from Eq. 5.16 and experiments), and (b, d, & f) are layer thickness decay profiles, ζ_i (based on Eq. 5.15 and experiments) for Ri_s=3.2 , 2, & 0.78.

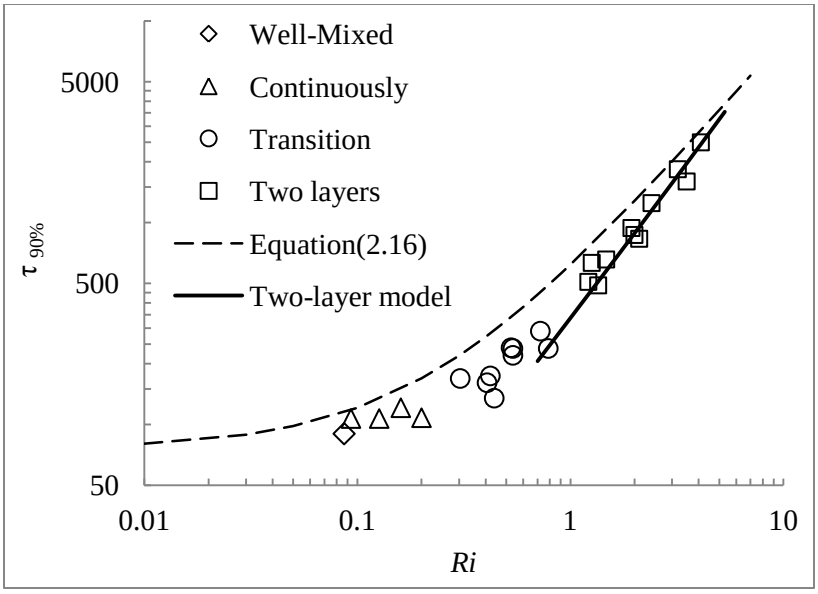

Figure 5.12: Time of 90% flushing from finite release experiments and models (for Ri>0.8). The dashed line is based on Equation (2.16). The solid line is based on two layer modeling with interfacial mixing as well as skimming.

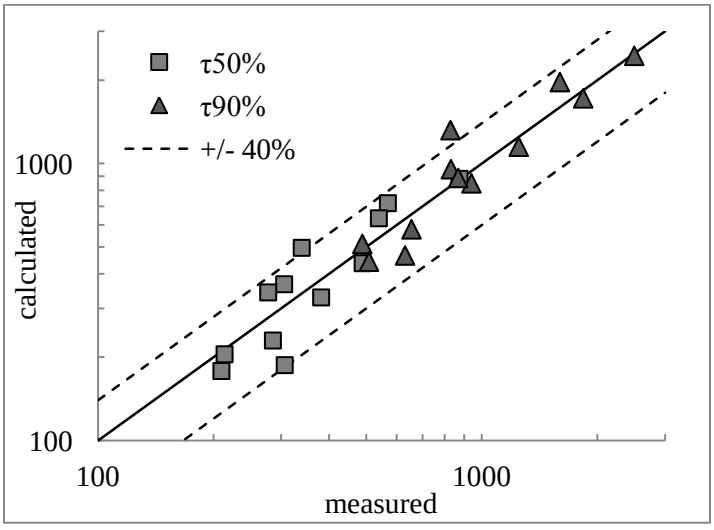

Figure 5.13: Comparison of the calculated and measured time for a) 90% flushing and b) 50% flushing.

5.4.1.2 Model verification with the continuous tests:

Equations (5.15) & (5.16) can be used to simulate the transition flow in the continuous tests as well. Figure 5.14 shows the transient flow in a continuous experiment with Ri=1.35.

The calculated steady state canyon total buoyancy is compared with the measured ones for all of the data involving a two-layer stratification regime presented in this chapter. The range of +/-40% agreement was shown for comparison in Figure 5.15. The model predicts the thickness of the layer more accurately than it predicts the buoyancy, due to the sensitivity of the solution to the α value, which is the difference between two small numbers and is therefore hard to measure accurately.

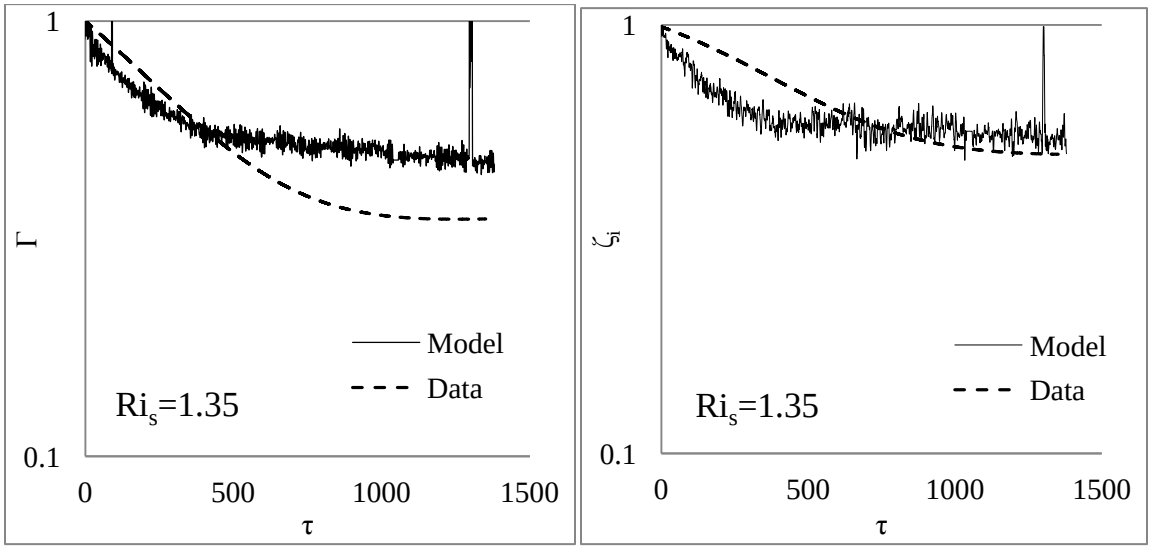

(a) (b)

Figure 5.14: Total buoyancy and layer thickness decay profiles for a continuous release experiment with Ri_s=1.35.

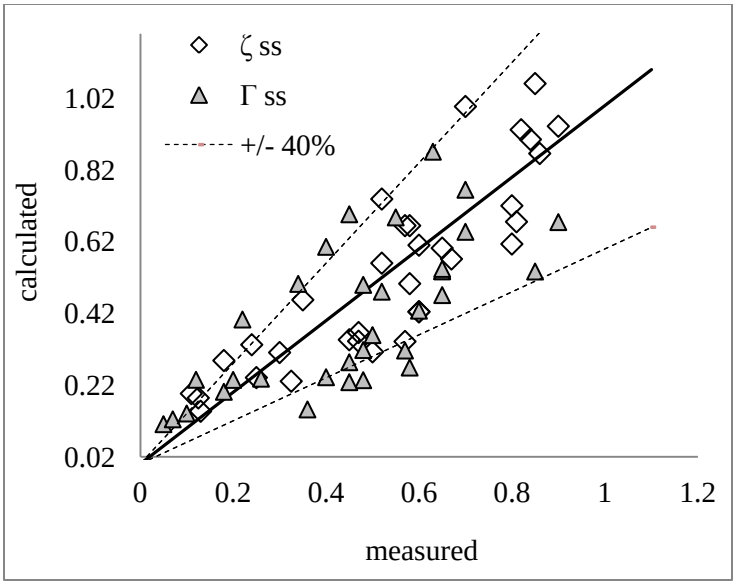

Figure 5.15: Comparison of the calculated and measured values for steady state total buoyancy and steady state interface height.

5.4.2 Continuous stratified and well-mixed regime

The theoretical model assumed a two-layer stratification. Hence the results will not be accurate if the model is applied to a continuous or well-mixed flow. In the case of a low Richardson number ($Ri < 0.8$), the density interface thickness grows and no distinct interface surface can be observed in the canyon. When the whole canyon is full with either a continuous stratification or a well-mixed flow, then the thickness of the layer is considered equal to the canyon depth and the buoyancy of the layer is defined as the average buoyancy of the canyon (see Figure 5.16):

$$g_l' = g_{ave}' = \frac{\int g' dA}{HW}. \tag{5.26}$$

So the dense layer is modeled as shown in Figure 5.16, and (5.9) will be:

$$\frac{d(Hg_{ave}')}{dt} = -g_{ave}' U(\alpha + \beta) + \frac{q_s g_s'}{W}. \tag{5.27}$$

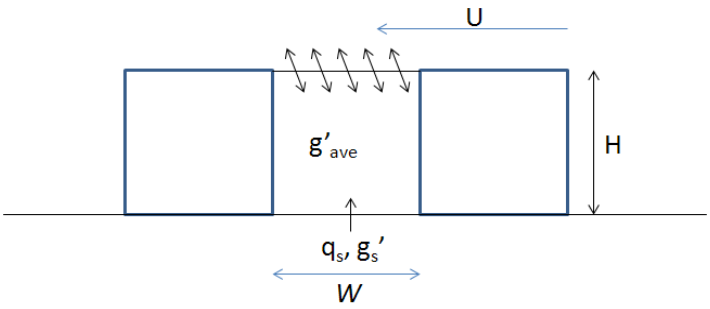

Figure 5.16: The exchange flow model for continuous and well-mixed flow regime

Since the interface height is constant at the top of the canyon, $\zeta_i = 1$ and $\beta = \varphi$. So $\Gamma = \gamma_l$ and (5.27) in non-dimensional form will be

$$\frac{d(\Gamma)}{d\tau} = -\Gamma(\alpha + \beta) + \varphi \qquad (5.28)$$

which is the same functional form of concentration decay for neutral contaminants introduced by Caton et al. (2003) and for weakly stratified flow by Castro et al. (1993).

For the case of no source emissions ($\varphi = 0$), solving differential equation (5.28) gives the same exponential function used for the total concentration decay in Chapter 2:

$$\Gamma = e^{-\alpha\tau}. \qquad (5.29)$$

So the exponential decay constant, k, defined in the previous chapter, is actually the exchange coefficient at the top of the canyon:

$$k = \alpha \qquad (5.30)$$

when $\varphi = 0$ since β= φ for the continuous release case . In general

$$k = \alpha + \beta. \qquad (5.31)$$

So the same form of equation (2.16) is expected to appropriately model $(\alpha + \beta)$. As was shown in Chapter 2, for the case of a neutrally buoyant fluid and a well-mixed regime, k is constant during the flushing process. Solving the derivative equation (5.29) for a constant k gives:

$$\Gamma = \Gamma_0 \mathrm{e}^{-\mathrm{k}\tau} + \frac{\varphi}{\mathrm{k}}\left(1 - \mathrm{e}^{-\mathrm{k}t}\right) \quad (5.32)$$

for a well-mixed flow where $\Gamma_0 = 0$ if the cavity is empty initially, and $\Gamma_0 = 1$ when the cavity is initially full.

When the role of buoyancy is important, k changes depending on the canyon Ri number at any time of flushing:

$$k = f(Ri_l) \quad (5.33)$$

This function was found in Chapter 2 for an aspect ratio one canyon based on the initial Richardson number. Using the empirical equation (2.16) for $(\alpha + \beta)$ in (5.28) gives a differential equation to model the flushing profile for continuous regime flows:

$$\frac{d(\Gamma)}{d\tau} = -\Gamma\left(\frac{1}{a+bRi_l}\right)^c + \varphi \quad (5.34)$$

for the continuous regime where $a = 18$, $b = 84$, and c = -1.21 from Equation (2.16).

5.4.2.1 Model verification for finite release experiments:

Equation (5.34) was used to model the continuous, well-mixed, and transition regime experiments presented in chapter 2. Figure 5.17 shows some example plots of the total buoyancy decay profile over time. The model simulates the decreasing decay rate over time.

For finite release experiments, Castro et al. (1993) suggested the following equation to calculate the time varied concentration of a V-shaped valley:

$$-Ln(C') + \frac{b}{c}Ri_0^c(1 - C'^c) = \tau/d_t \quad (5.35)$$

in which $C' = C(t)/C_s$, Ri_0 is the Ri number at t=0, c=0.5, and d_t is a time decay constant, suggested to be 15 based on their experiments. Values for b of 3.7 for continuous release tests

and 7.9 for the finite release tests were obtained from their experiments. The results from this model are also shown in Figure 5.17.

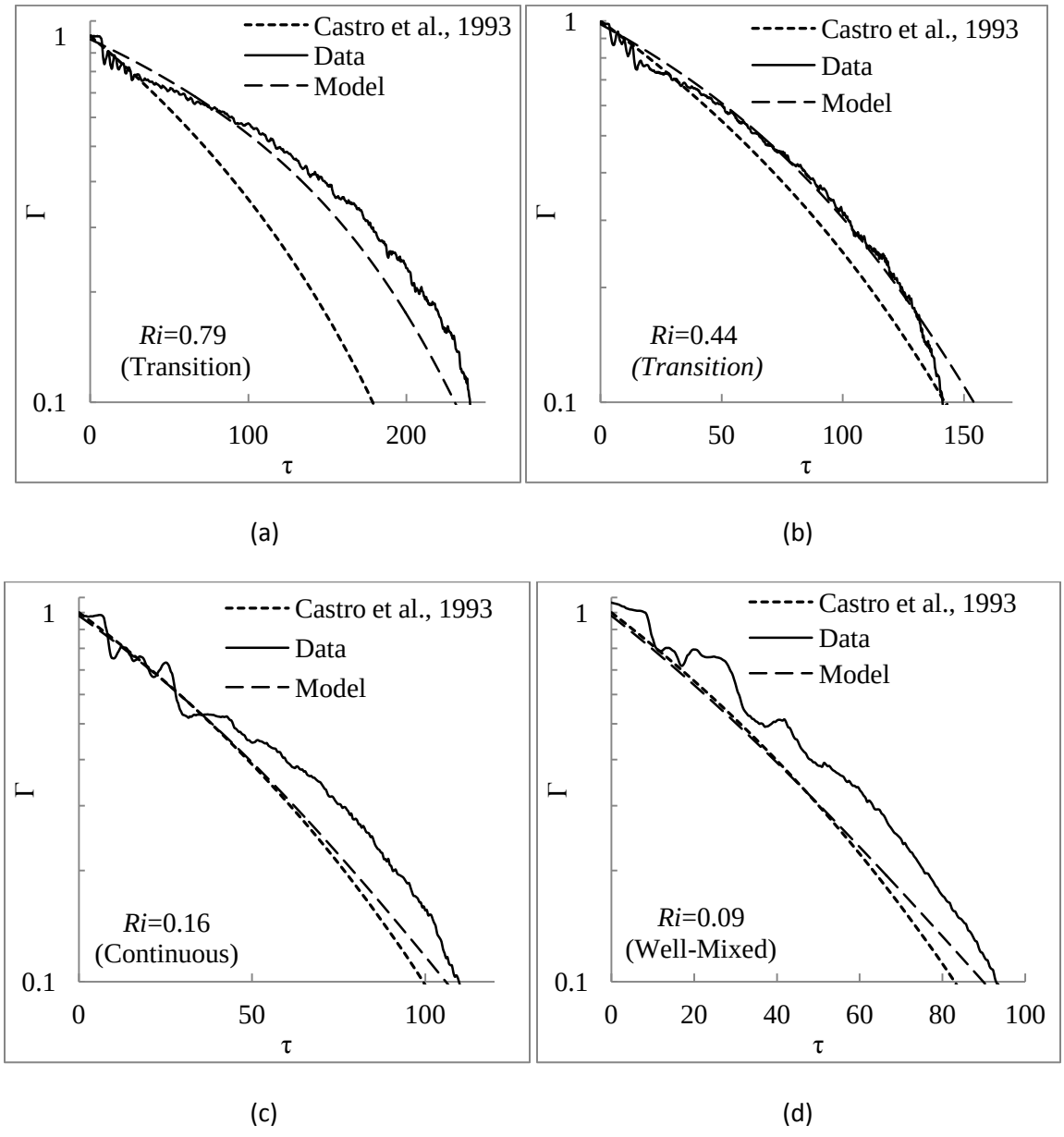

Figure 5.17: Total buoyancy decay profile for finite release experiments in different regimes: Transition, Continuous, and Well mixed.

To compare the models' performance, the time of 90% flushing was calculated based on both models and compared with the finite release experiments (only for non-two-layer stratification regimes, Ri<0.8, when both the models are valid). The comparison is shown in Figure 5. 18. As is shown in Figure 5.17, Castro's model does not work well for the transition regime while suggested model reasonably predicts the decay rate profile for all regimes: transition, continuous, and well mixed. Generally Castro's model under predicts the time of flushing. This might be explained by the V-shaped canyon geometry that was used in Castro's experiments.

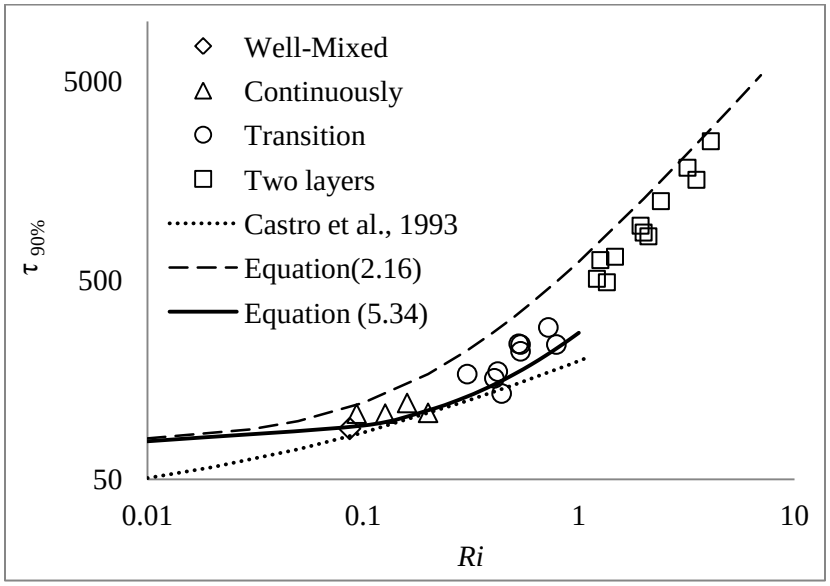

Figure 5.18: Time of 90% flushing from experiments and different models (for Ri<1). The dashed line is based on k as a function of the initial Ri number. The solid line is based on k as a function of the layer Ri number. The dotted line is based on the valley model of Castro et al. (1993).

Figure 5.19 presents the comparison of 90% and 50% flushing time measured from finite release experiments and predicted by Equations (5.34 & 5.35). As shown in Figure 5.19 suggested model results collapse in +/- 40% region.

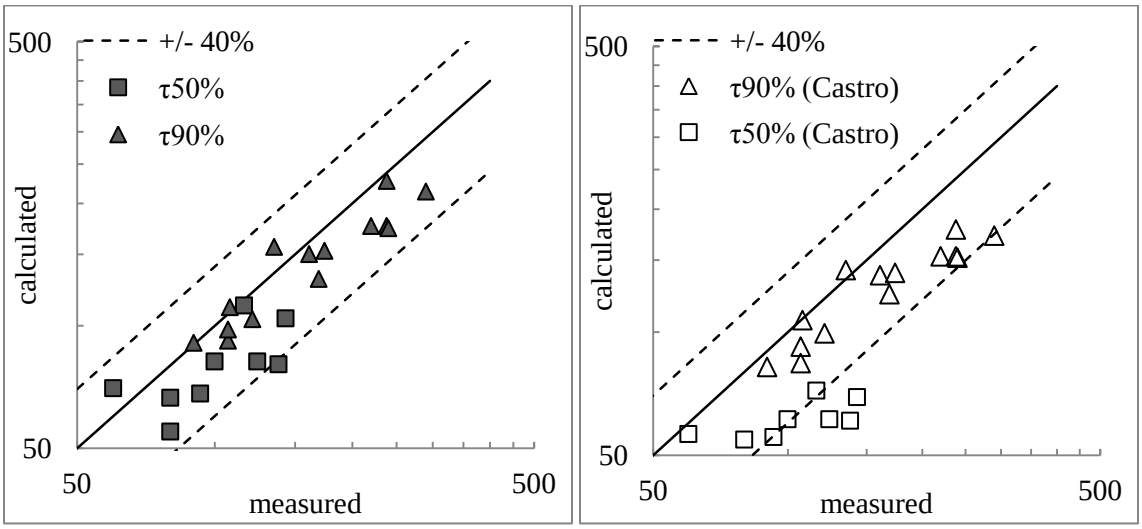

(a) (b)

Figure 5.19: Comparison of calculated and measured time of 90% and 50% flushing for the continuous, well-mixed and transition regime experiments in Chapter 2, with a) suggested model by Eq.(5.34) and b) Castro et al. (1993).

5.4.2.2 Model verification for continuous release experiments:

Based on Equations (5.28) and (5.30), the steady-state k value can also be measured from steady state tests by:

$$k_{ss} = \frac{\varphi}{\Gamma_{ss}} \tag{5.36}$$

The results of the experiments shown in Figure 5.9 are compared with the predicted k value from the empirical function (2.16) and finite release experiments. Figure 5.20 shows the

measured k_{ss} for all tests based on the layer Richardson number. Notably, the layer buoyancy for a two-layer stratified flow regime is based on the density of the dense layer, while for the other regimes the average buoyancy of the canyon was used. The results from steady state experiments show good agreement with the empirical equation (2.16) and finite release tests. This confirms that the effect of initial condition and running the flume abruptly at the finite release experiments had no significant effect on the k value and flushing rate calculated over the initial stage in Chapters 2, 3 and 4.

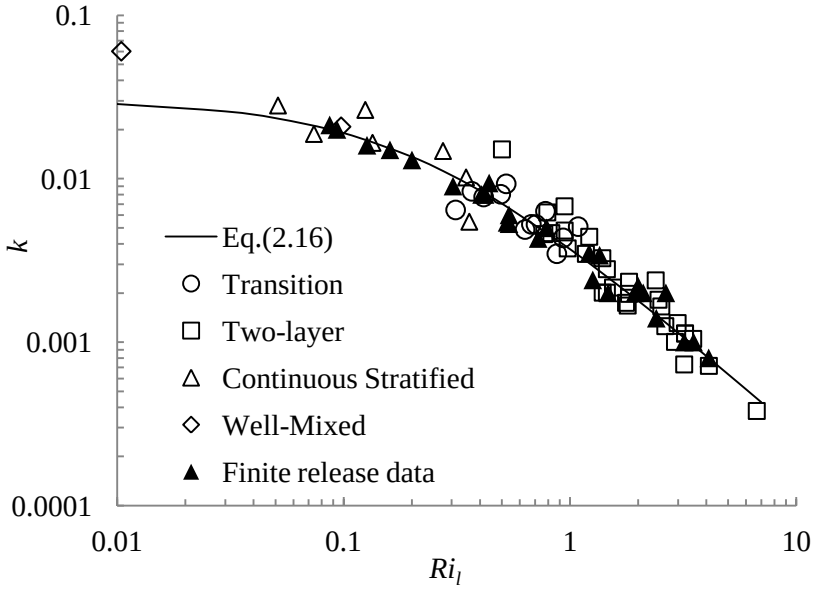

Figure 5.20: Experimental steady state k value in comparison with the empirical equation (2.16) and the finite release tests for the same canyon geometry and upstream conditions.

5.5 Discussion and conclusions

An ordinary differential equation was presented to model analytically the total buoyancy flushing from a two-layer stratified canyon and the thickness of the dense layer (Eqs. 15.15 & 15.16). A series of constant buoyancy influx experiments were employed to find the

empirical equations (5.24) and (5.25) for the exchange and skimming parameters in this ODE model. The continuous release experiments were conducted over a range of source buoyancy, 0.1<Ri_s<7 and for different source flow rates.

The results from model simulations were compared with the experimental buoyancy decay and interface height profiles (Figure 5.11 for finite release and Figure 5.14 for continuous release experiments). For the non-two-layer flow regimes (i.e., transition, continuous, and well-mixed flow) a differential equation similar to the form used by Castro et al. (1993) was introduced based on the empirical function (2.16) for the exponential decay as a function of the Richardson number. Using the Richardson number of the layer, Ri_l, in (2.16) rather than Ri_s significantly improves the flushing time prediction for the finite release experiments (Figure 5.12). Using Ri_l also improves the prediction of the decay rate profile as it models the increase in decay rate, k, over time.(Figure 5.11). Compared to the Castro's model, suggested equation (5.34) shows better agreement in the flushing time prediction (Figure 5.13) and buoyancy profile (Figure 5.11a). This model (Eq. 5.34) can be used for well-mixed flows and, hence, neutrally buoyant pollutants as well as dense pollutants (e.g. Figure 511d).

A plot of the experimental k values, from the steady state experiments, versus the layer Richardson number collapse perfectly over the finite release averaged k data and (2.16).

Both models from sections 5.3 and 5.4 can be summarized for use in a numerical calculation. Two regions were defined to specify the k and β parameters: two-layer when 0.8<Ri, and continuous when Ri<0.8.

$$\frac{d(\zeta_i)}{d\tau} = -\beta + \varphi, \tag{5.15}$$

$$\frac{d(\Gamma)}{d\tau} = -\Gamma(\mathrm{k}) + \varphi. \tag{5.37}$$

$$\begin{cases} k = \left(\frac{1}{18+84Ri_l}\right)^{1.21} & for\ Ri_s < 0.8 \\ k = \frac{(\alpha+\beta)}{\zeta_i} = 4.61 \times 10^{-3}(Ri_l)^{-1.27} & for\ Ri_s > 0.8 \end{cases} \quad (5.38)$$

$$\begin{cases} \beta = \varphi & for\ Ri_s < 0.8 \\ \beta = 3.33 \times 10^{-3}(Ri_l)^{-1.14} & for\ Ri_s > 0.8 \end{cases} \quad (5.39)$$

Figure 5.21 graphically shows the equation used in (5.38) for each Richardson number. The flushing results from suggested model were presented over a wide range of Richardson numbers in comparison with the experimental data in Figure 5.22.

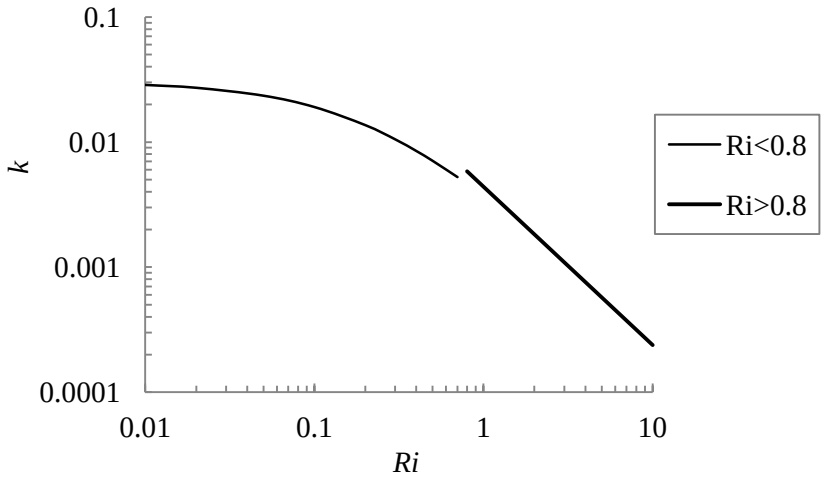

Figure 5.21: Exponential decay coefficient, k, in the model Eq.(5.37) for different Richardson numbers.

The steady state layer thickness and canyon buoyancy for data in Figure 5.9 can be calculated based on Equations (5.15)& (5.37), regardless of the regime observed and only based on the initial Ri numbers. The steady state data for the two-layer regime was already presented in Figure 5.15. The well-mixed, continuous, and transition experiments in Figure 5.9 are compared with the results of the model in Figure 5.23, showing a good agreement of +/- 40% .

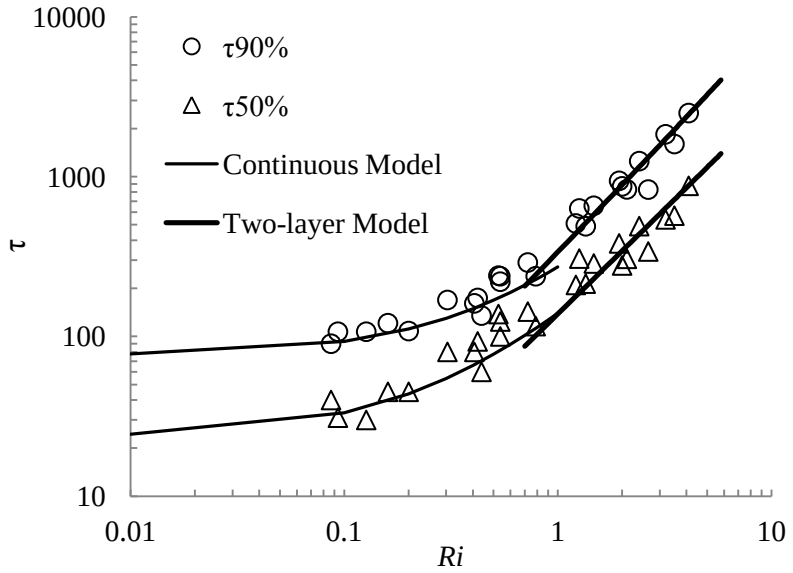

Figure 5.22: 90% and 50% flushing from Model Eq.(5.15)&(5.37) for two regions (Ri<0.8 & Ri>0.8) in comparison to the data from finite release experiments.

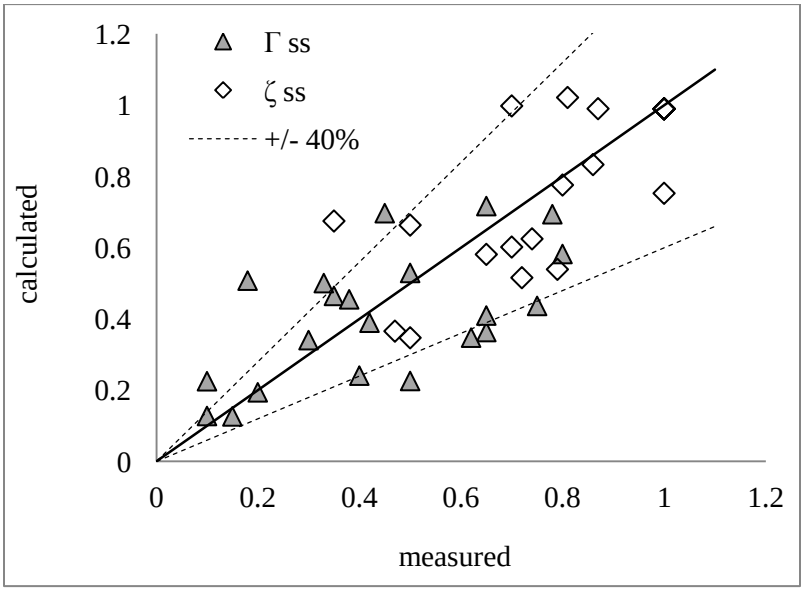

Figure 5.23: Steady state total buoyancy and interface height for well-mixed, continuous, and transition experiments in Figure 5.9. Measured ζ_{ss} was considered 1 when the interface height was not discernible.

CHAPTER SIX

SUMMARY, CONCLUSIONS, AND RECOMMENDATIONS

6.1 Summary

This study has presented an experimental investigation of the effect of buoyancy, canyon aspect ratio, and the upstream surface roughness on the flushing of a dense fluid from a street canyon. Chapter One reviewed and summarized previous studies on urban canyon flows and dispersion. The specific problem and its parameterization were explained in Section 1.3.

To understand the mechanics of flushing, four series of finite release experiments for different aspect ratios (η=0.45, 0.75, 1, 2) and three series of tests for different upstream surface roughness (d_{84}= 1.14, 0.83, and 0.0 cm) were conducted over a range of Richardson numbers. The experiments were conducted in a water flume and salt water was used as the dense fluid. The LAT technique was employed to measure the buoyancy in the canyon during the experiment. The details of the experimental set-up and technique were discussed in Section 2.2.

Qualitative and quantitative examination of the results was presented to discuss the effects of different parameters on the flow regime and flushing rate from a canyon. Based on finite release experiments, empirical equations were presented in Chapters 2, 3, and 4 to estimate the rate of buoyancy decay in a canyon with different aspect ratios and different upstream turbulence intensities.

In Chapter 5, an analytical model for an ideal canyon was presented to predict the total buoyancy of the canyon, Γ, at any time during the flushing. This model was developed for a

canyon of aspect ratio one, based on the empirical equations found from finite release and continuous release tests (Eq.5.58).

6.2 Conclusion

The flow is both qualitatively and quantitatively influenced by the buoyancy of the pollution, canyon geometry, and upstream boundary layer properties. The main results stemming from the experiments and the conclusions based on each chapter's findings are highlighted as follows.

6.2.1 Initial purging:

The Richardson number and aspect ratio strongly affects the initial flushing mechanics, i.e. deflection depth and vortex penetration into the dense layer. The initial angle of deflection and vortex penetration depth are a function of the cavity aspect ratio and flow Richardson number. For higher Richardson numbers and lower aspect ratio, the vortex penetrates less deeply into the dense layer due to the higher stability of the stratification. However, the upstream boundary layer properties have no effect on this stage.

For a constant Richardson number, changing the upstream surface roughness did not affect the initial purging mechanism because this stage is dominated by the large scale interfacial waves and vortices that are functions of the mean flow upstream of the canyon.

6.2.2 Flow regime

For all geometric configurations and upstream surface roughnesses, the dynamics of the mixing has been examined and three separate flow regimes were identified based on Richardson numbers.

For low Richardson numbers, the cavity remains well mixed during the flushing process and the density difference decays exponentially (as observed for flushing a neutrally buoyant tracer). As the Richardson number increases, the cavity becomes more stably stratified and a continuous stratification is maintained. Finally for high Richardson numbers, a strong two-layer stratification was observed.

The transition Richardson numbers among these three different regimes is a function of the canyon geometry and upstream surface morphology. For taller, narrower cavities or lower upstream turbulence intensity, a two-layer stratification was observed for lower Richardson numbers compared to wider cavities or rougher turbulent boundary layers.

6.2.3 Layer buoyancy decay

Data analysis and inspection of the buoyancy profiles revealed that for the two-layer regime experiment, the lower dense layer gets thinner over time. This indicates that dense fluid is being skimmed from the top of the layer. The layer also gets less dense, indicating that ambient fluid is being mixed down into the dense layer. This is in contrast with previous studies that only observed flushing by skimming. Mixing into the layer decreases as the layer stability increases (e.g., higher Ri, lower aspect ratio, or lower turbulence intensity).

The layer buoyancy decreases linearly over time until the shear layer reaches the bottom of the cavity, at which point there is a dramatic increase in the rate of layer buoyancy

reduction. Results also indicate that the density interface is thinner than the shear layer that is driving the mixing, and that the difference in thicknesses increases with increasing Richardson number. This result is consistent with previous studies of mixing in stratified shear flows.

6.2.4 Initial exponential decay rate, k

Although the decay rate is observed to increase as the total buoyancy in the canyon decreases, for all experiments it can be well approximated as constant over an initial range of the buoyancy flushing (usually between $0.3 < \Gamma < 0.7$).

The initial exponential decay rate was calculated for each experiment and is well described by the empirical relationship in Eq.(2.16). Once the first portion of the dense fluid has been flushed, the decay rate increases if the stratification weakens and decreases if the mixing in the layer is suppressed (due to very high density, a low aspect ratio canyon, or low turbulence intensity).

In addition to the Richardson number, the decay rate (k) varies for different aspect ratios but not for different upstream turbulence intensities. Lowering the aspect ratio restricts the initial purging flow and consequently reduces the decay rate. The upstream surface roughness increases the turbulence intensity. This does not alter the initial flushing and only influences the flow for more stable stratifications when small scale eddies dominate the mixing process. This small scale nibbling is not observed when the Richardson number is too low, because all the flushing is done by the large scale flow and the large vortex that penetrates into the canyon.

For large Richardson numbers, the time of transition (from large scale to the small scale mixing flow) was found at $\Gamma = 0.55$. After this stage, the reminder of the purging process is dominated by small scale turbulent eddies.

6.2.5 Time of flushing

The time taken to flush a dense fluid from a canyon increases with the Richardson number. It also rises when a particularly tall and narrow canyon is considered, rather than a square canyon. Narrower street canyons limit the width of large scale vortices in the canyon and hence reduce vertical mixing.

Replacing the rough boundary layer with a smooth one has no effect on the time taken to flush 50% of the canyon buoyancy, since it approximately corresponds to the initial exponential decay rate which is dominated by the large-scale flushing flow. The time taken to flush 90% better illustrates the effect of upstream surface roughness. Decreasing surface roughness has the same effect as decreasing aspect ratio and causes a dramatic change in time of flushing due to lower turbulent intensity generation.

In general it was observed that increasing the Richardson number, decreasing the canyon aspect ratio, and decreasing the upstream surface roughness resulted in an increasingly strong stratification within the canyon and longer trapping times for the pollutant.

6.2.6 Continuous release experiments and modeling

A two-layer model was developed to parameterize the mixing and skimming processes observed during both the finite release and continuous release experiments. The continuous release experiments allowed for the direct measurement of the flushing rate for any layer depth

and Richardson number. Both the skimming rate and the interfacial mixing rate were found to be power-law functions of the Richardson numbers of the layer. The sum of these two parameters is equivalent to the exponential decay rate measured by the finite release experiments. A high degree of consistency was found between the finite release data and the continuous release data as shown in Figure (5.21). This agreement acts as an excellent check on measurement techniques, as the finite release data was based on curve fitting through buoyancy versus time data while the continuous release data was calculated directly by measuring the rate of addition of volume and buoyancy once a steady state was established.

6.3 Recommendations

While this dissertation presents the first detailed analysis of the role of buoyancy on mixing in a street canyon for a wide range of aspect ratios and upstream boundary layer conditions, much work remains. It includes:

1. Different geometries: this dissertation has only considered isolated street canyons. The role of an array of upstream buildings should be studied as well as a broader range of aspect ratios.
2. More detailed parameterization of the role of aspect ratio and turbulence intensity on the initial and later stage mixing: While the initial decay rate and time to flush 90% of the buoyancy has been measured, parameterizations based on continuous release experiments would improve the modeling of the decay rate over time.
3. In depth analysis of the role of turbulence intensity on the flushing rate: The role of turbulence intensity has been explored in this dissertation by examining the effect of different upstream turbulence intensities on the flushing rate. The detailed mechanics

could be explored by looking at the time varying velocity field within the canyon using PIV.

4. Computational modeling: A 2D CFD model of the current work could be developed and compared with the experimental results of this study and the analytical model predictions. A 3D numerical model might be able to capture the small scale eddies that skim patches of dense fluid off the dense layer at the later stages of the purging process.

REFERENCES

Allgayer, D. and Hunt, G. R., “On the application of the light-attenuation technique as a tool for non-intrusive buoyancy measurements ”Experimental Thermal and Fluid Science, 38, (2012): 257–261.

Al-Jiboori, M. H., and H. U Fei. "Surface roughness around a 325-m meteorological tower and its effect on urban turbulence." Advances in Atmospheric Sciences 22.4 (2005): 595-605.

Armfield, S. W, and W. Debler. "Purging of density stabilized basins." International Journal of Heat and Mass Transfer 36.2 (1993): 519-30.

ASCE “Wind tunnel studies of buildings and structures”, ASCE manuals and reports on engineering practice No. 67, ASCE, Reston, VA, USA, (1999).

ASCE / SEI 7-10, “Minimum design loads for buildings and other structures”, American Society of Civil Engineers, Reston, VA, USA, (2010).

Baik, J.J., Park, R.S., Chun, H.Y., Kim, J.J., "A laboratory model of urban street-canyon flows." Journal of Applied Meteorology 39.9 (2000): 1592-600.

Briggs, G. A., R. S. Thompson, and W. H. Snyder, “Dense gas removal from a valley by crosswinds”. J. Hazardous Mater. 24 (1990): 1–38.

Buckley, R. L., C. H. Hunter, R. P. Addis, and M. J. Parker. "Modeling dispersion from toxic gas released after a train collision in graniteville, SC." Journal of the Air & Waste Management Association 57.3 (2007): 268-78.

Castro, I. P., A. Kumarb, W. H. Snyder and S. P. S. Aryad. "Removal of slightly heavy gases from a valley by crosswinds." Journal of hazardous materials 34.3 (1993): 271-93.

Caton, F., R. E. Britter, and S. Dalziel. "Dispersion mechanisms in a street canyon." Atmospheric Environment 37.5 (2003): 693-702.

Cenedese, C., Dalziel, S. B., “Concentration and depth field determined by the light transmitted through a dyed solution” Proceedings of the 8th international symposium on flow visualization, (1998).

Chang, C. H., and R. N. Meroney. "Concentration and flow distributions in Urban street canyons: wind tunnel and computational data." Journal of Wind Engineering and Industrial Aerodynamics 91.9 (2003): 1141-54.

Chang, K., G. Constantinescu, and S. O. Park. "Purging of a neutrally buoyant or a dense miscible contaminant from a rectangular cavity. I: Case of an Incoming Laminar Boundary Layer." Journal of Hydraulic Engineering 133 (2007a): 361.

Chang, K., G. Constantinescu, and S. O. Park.. "Purging of a neutrally buoyant or a dense miscible contaminant from a rectangular cavity. II: Case of an Incoming Fully Turbulent Overflow." Journal of Hydraulic Engineering 133 (2007b): 373.

Chan, T. L, G. Dong, C.W. Leung, C.S. Cheung, W.T. Hung. "Validation of a two-dimensional pollutant dispersion model in an isolated street canyon." Atmospheric Environment 36.5 (2002): 861-72.

Cheng, W. C, C. H. Liu, and D. Y. C. Leung. "On the correlation of air and pollutant exchange for street canyons in combined wind-buoyancy-driven flow." Atmospheric Environment 43.24 (2009): 3682-90.

Cheng, W. C, and C. H. Liu. "Large-Eddy simulation of turbulent transports in urban street canyons in different thermal stabilities." Journal of Wind Engineering and Industrial Aerodynamics 99 (2011): 434–442

Cheng, W. C, C. H. Liu, and D. Y. C. Leung. "Computational formulation for the evaluation of street canyon Ventilation and pollutant removal performance." Atmospheric Environment 42.40 (2008): 9041-51.

Christen, A., E. van Gorsel, and R. Vogt. "Coherent structures in urban roughness sublayer turbulence." International Journal of Climatology 27.14 (2007): 1955-68.

Coates, M. J., Guo, Y. and Davies, P.A. “Laboratory model studies of flushing of trapped saltwater from a blocked tidal estuary” J. Hydraulic Res. 39 (6), (2001): 601-609.

Coceal, O., T. G. Thomas, and S. E. Belcher. "Spatial variability of flow statistics within regular building arrays." Boundary-Layer Meteorology 125.3 (2007): 537-52.

Coffey, C. J., Ph.D. thesis, Imperial College London, (2006).

Cook, N. J., Jenson number- a proposal. Letter to the Editor J. of wind Engg & Ind. Aerod., 22, (1986): 95-96.

Deaves, D. M. "Dense gas dispersion modelling." Journal of Loss Prevention in the Process Industries 5.4 (1992): 219-27.

Debler and J. Imberger, “Flushing criteria in estuarine and laboratory experiments,” J. Hydraul. Eng. 122, 728 (1996).

Debler, W., and S. W. Armfield. "The purging of saline water from rectangular and trapezoidal cavities by an overflow of turbulent sweet water." Journal of Hydraulic Research 35.1 (1997): 43-62.

DePaul, F. T, and CM Sheih. "Measurements of wind velocities in a street canyon”." Atmospheric Environment (1967) 20.3 (1986): 455-9.

Di Sabatino, S., R. Buccolieri, B. Pulvirenti, R. Britter. "Simulations of pollutant dispersion within idealised urban-type geometries with CFD and integral models." Atmospheric Environment 41.37 (2007): 8316-29.

Hacker, J., P. F. Linden, and S. B. Dalziel, “Mixing in lock-release gravity currents,” Dyn. Atmos. Oceans 24, (1996): 183–195.

Hamlyn, D., T. Hilderman, and R. Britter. "A Simple network approach to modelling dispersion among large groups of obstacles." Atmospheric Environment 41.28 (2007): 5848-62.

Hacker, J., Linden, P. F. and Dalziel, S. B., “Mixing in lock-release gravity currents” Dyn. Atmos. Oceans”, 24, (1996): 183-195.

Hanna, Steven S., S. Dharmavaram, J. Zhang, I. Sykes, H. Witlox, S. Khajehnajafi, and K. Koslan, "Comparison of six widely-used dense gas dispersion models for three recent chlorine railcar accidents." Process Safety Progress 27.3 (2008): 248-59.

Huang, H., Y. Akutsu, M. Arai, M. Tamura, "A Two-dimensional air quality model in an urban street canyon: evaluation and sensitivity analysis." Atmospheric Environment 34.5 (2000): 689-98.

Hughes, G. O., and R. W Griffiths, “A simple convective model of the global overturning circulation, including effects of entrainment into sinking regions,” Ocean Modelling 12 (2005): 46–79.

Jensen, M. "The model-law for phenomena in natural wind." Ingenioren 2.4 (1958): 121-8.

Karimpour, A., N. Kaye, and Z. Baratian, “Modeling the neutrally stable atmospheric boundary layer for laboratory scale studies of the built environment” Bldg. & Env. 49, (2012): 203-211.

Kaye, N. B, and G. R Hunt. "Time-Dependent Flows in an Emptying Filling Box." Journal of Fluid Mechanics 520 (2004): 135-56.

Kim, J. J., and J. J. Baik, "Urban street-canyon flows with bottom heating." Atmospheric Environment 35.20 (2001): 3395-404.

Kim, J. J., and J. J. Baik, “Effects of inflow turbulence intensity on flow and pollutant dispersion in an urban street canyon”. Journal of Wind Engineering and Industrial Aerodynamics, 91, (2003): 309–329.

Kim, J. J., and J. J. Baik. "Physical experiments to investigate the effects of street bottom heating and inflow turbulence on urban street-canyon flow." Advances in Atmospheric Sciences 22.2 (2005): 230-7.

Kirkpatrick, M. P, S. W Armfield, and N. Williamson. "Shear driven purging of negatively buoyant fluid from trapezoidal depressions and cavities." Physics of Fluids 24 (2012): 025106.

Kirkpatrick, M. P, and S. W Armfield. "Experimental and large eddy simulation results for the purging of salt water from a cavity by an overflow of fresh water." International Journal of Heat and Mass Transfer 48.2 (2005): 341-59.

Klein, P., B. Leitl, and M. Schatzmann. "Driving physical mechanisms of flow and dispersion in urban canopies." International Journal of Climatology 27.14 (2007): 1887-907.

Kurup, R. G., and D. P. Hamilton. "Flushing of dense, hypoxic water from a cavity of the swan river estuary, western australia." Estuaries and Coasts 25.5 (2002): 908-15.

Li, X.-X., C. H. Liu, , D.Y.C. Leung, “Development of a k-ε model for the determination of air exchange rates for street canyons”. Atmospheric Environment 39 (38) (2005): 7285–7296.

Li, X. X., D.Y.C. Leung, and C. H. Liu. "Physical modeling of flow field inside urban street canyons." Journal of Applied Meteorology and Climatology 47.7 (2008):2058-67

Li, X. X., R. E. Britter, T. Y. Koh, L. K. Norford, C. H. Liu, D. Entekhabi, D. Y. C. Leung. "Large-eddy simulation of flow and pollutant transport in urban street canyons with ground heating." Boundary-Layer Meteorology 137.2 (2010): 187-204.

Linden, P. F., "Mixing in stratified fluids." Geophysical & Astrophysical Fluid Dynamics 13.1 (1979): 3-23.

Linden, P. F., G. F Lane-Serff, and D. A Smeed. "Emptying filling boxes: the fluid mechanics of natural ventilation." Journal of Fluid Mechanics 212.-1 (1990): 309-35.

Liu, H.Z., Liang, B., Zhu, F.R., Zhang, B.Y., Sang, J.G., "A laboratory model for the flow in urban street canyons induced by bottom heating." Advances in Atmospheric Sciences 20.4 (2003): 554-64

Liu, C. H., D. Y. C. Leung, and M. C. Barth. "On the prediction of air and pollutant exchange rates in street canyons of different aspect ratios using large-eddy simulation." Atmospheric Environment 39.9 (2005): 1567-74.

Liu, C. H., W.C. Cheng, T. C. Y. Leung, D. Y. C. Leung. "On the mechanism of air pollutant re-entrainment in two-dimensional idealized street canyons." Atmospheric Environment 45.27 (2011): 4763-9

Macdonald, R. W. "Modelling the Mean Velocity Profile in the Urban Canopy Layer." Boundary-layer meteorology 97.1 (2000): 25-45.

Macdonald, R. W, R. F Griffiths, and S. C Cheah. "Field experiments of dispersion through regular arrays of cubic structures." Atmospheric Environment 31.6 (1997): 783-95.

Macdonald, R. W, R. F Griffiths, and D. J. Hall, “A comparison of results from scaled field and wind tunnel modelling of dispersion in arrays of obstacles,” Atmospheric Environment 32, (1998): 3845–3862.

Mavroidis, I., and R. F Griffiths. "Local characteristics of atmospheric dispersion within building arrays." Atmospheric Environment 35.16 (2001): 2941-54.

Meroney, R. N., M. Pavageau , S. Rafailidis, M. Schatzmann. "Study of line source characteristics for 2-D physical modelling of pollutant dispersion in street canyons." Journal of Wind Engineering and Industrial Aerodynamics 62.1 (1996): 37-56.

Oke, T. R. "Street design and urban canopy layer climate." Energy and Buildings 11.1-3 (1988): 103-13.

Olvera, H. A., A. R. Choudhuri, and W. W. Li. "Effects of plume buoyancy and momentum on the near-wake flow structure and dispersion behind an idealized building." Journal of Wind Engineering and Industrial Aerodynamics 96.2 (2008): 209-28.

Park, S. K., S. D. Kim, and H. Lee. "Dispersion characteristics of vehicle emission in an urban street canyon." Science of the total environment 323.1-3 (2004): 263-71.

Pascheke, F., J. F. Barlow, and A. Robins. "Wind-tunnel modelling of dispersion from a scalar area source in urban-like roughness." Boundary-Layer Meteorology 126.1 (2008): 103-24.

Pasquill, F. "Wind structure in the atmospheric boundary layer." Philosophical Transactions of the Royal Society of London.Series A, Mathematical and Physical Sciences 269.1199 (1971): 439.

Roberts, P. T, REJ Fryer-Taylor, and DJ Hall. "Wind-tunnel studies of roughness effects in gas dispersion." Atmospheric Environment 28.11 (1994): 1861-70.

Rotach, M. W. "On the influence of the urban roughness sublayer on turbulence and dispersion." Atmospheric Environment 33.24-25 (1999): 4001-8.

Roth, M. "Review of atmospheric turbulence over cities." Quarterly Journal of the Royal Meteorological Society 126.564 (2000): 941-90.

Simoėns, S., M. Ayrault, and J. M. Wallace. "The flow across a street canyon of variable width--part 1: kinematic description." Atmospheric Environment 41.39 (2007): 9002-17.

Simoėns, S., and J. M. Wallace. "The flow across a street canyon of variable width--part 2: Scalar dispersion from a street level line source." Atmospheric Environment 42.10 (2008): 2489-503.

Sini, J., Anquetin, S., and Mestayer, P. G., “Pollutant dispersion and thermal effects in urban street canyons,” Atmospheric Environment 30 (1996): 2659–2677.

Smart, G. M. "Turbulent velocity profiles and boundary shear in gravel bed rivers." Journal of Hydraulic Engineering 125 (1999): 106.

Soulhac, L., R. J. Perkins, and P. Salizzoni. "flow in a street canyon for any external wind direction." Boundary-Layer Meteorology 126.3 (2008): 365-88.

Strang, E. J, and H. J. S. Fernando. "Shear-induced mixing and transport from a rectangular cavity." Journal of Fluid Mechanics 520 (2004): 23-49.

Taseiko, O. V., S. V. Mikhailuta, A. Pitt, A. A. Lezhenin, Y. V. Zakharov, "Air pollution dispersion within urban street canyons." Atmospheric Environment 43.2 (2009): 245-52.

Uehara, K., S. Murakami, S. Oikawa, S. Wakamatsu. "Wind tunnel experiments on how thermal stratification affects flow in and above urban street canyons." Atmospheric Environment 34.10 (2000): 1553-62

Wahlin, A., and Cenedese, C., “How entraining density currents influence the stratification in a one-dimensional ocean basin,” Deep-Sea Res. II 53, (2006): 172–193.

Woods, A. W., and Caulfield, C. P., “A laboratory study of explosive volcanic eruptions,” J. Geophys. Res. 97, (1992): 6,699–6,712.

Xie, X., C. H. Liu, and D. Y. C. Leung. M. K.H. Leung, "Characteristics of air exchange in a street canyon with ground heating." Atmospheric Environment 41.39 (2007): 9030-49.

Xie, X., C. H. Liu, and D. Y. C. Leung. "Impact of building facades and ground heating on wind flow and pollutant transport in street canyons." Atmospheric Environment 41.39 (2007): 9030-49.

Zhou, Y., and S. R. Hanna. "Along-wind dispersion of puffs released in a built-up urban area." boundary-layer meteorology 125, (2007): 469–486.